



Università degli Studi di Napoli Federico II

Dottorato di Ricerca in Rischio Sismico

XXI ciclo

**Determination of Site amplification in the Campania-
Lucania Region (Southern Italy) by comparison of
different Site-Response Estimation Techniques**

Dott. Luciana Cantore

Tutor

Dott. Vincenzo Convertito

Coordinatore

Prof. Paolo Gasparini

Introduction.....	4
1.....	9
Local effects on strong ground motion: main characteristics	9
1.1. Introduction.....	9
1.2. Surface topography effects	9
1.3. Basin geometry effects.....	10
1.4. Effects of soft surface layers: main characteristics	11
2.....	14
Development of a map of geologically defined site-condition classes for the Campania-Lucania region (Southern Italy).....	14
2.1. Introduction.....	14
2.2. Geological setting of the Campania-Lucania region - Southern Appenine	15
2.3. Historical and recent seismicity	18
2.4. Site-conditions map for Campania-Lucania region	19
3.....	23
Data selected	23
3.1. Strong-Motion Data Set	23
4.....	27
Simulation of peak ground motion parameters using the stochastic simulation technique.	27
4.1. Introduction.....	27
4.1. The basis of stochastic method: general overview	28
4.3. Obtaining ground motions: simulations of time series	30
4.4. Application.....	32
5.....	56
Estimation of site amplification in the Campania-Lucania region (Southern Italy), by non-linear inversion of microearthquake spectra	56
5.1. Introduction.....	56
5.2. Inverse theory	58
5.3. Simplex method	61
5.4. Spectrum computation	63
5.5. Description of the inversion method.....	64
5.6. Inversion results	66
5.7. Site amplification maps for the Camapania-Lucania region.....	82
6.....	86
H/V spectral ratio of earthquake data	86
6.1. Introduction.....	86
6.2. The technique.....	86
6.3. Comparison of different site response estimation techniques.....	87
Conclusions.....	104
References.....	106

Introduction

It is well known that the surface geology is one of the dominant factors that affect the amplitude, duration, and frequency content of strong ground-motion.

Studies of historic and recent earthquakes have indicated that the local amplification of the strength of the observed seismic waves can be correlated with the surface topography, with sedimentary sites and with strong lateral discontinuities. In fact, these local geological effects, known as "site effects", can amplify or deamplify the seismic ground motion, producing difference in shaking intensity (Bard et al., 1988; Bard and Bouchon, 1985).

During both the 1906 San Francisco earthquake and the 1989 Loma Prieta seismic event, for example, local amplification over soft soils was responsible for intensity variations as large as two degrees. Nearly all recent destructive events like Michoacan, Messico 1985, Spitak, Armenia 1988, Iran 1990, Philippines 1990, Northridge 1994, Kobe 1995 and so on, have had dramatic evidence of site effects. As a consequence, seismologists and engineers have conducted many studies to quantify how the seismic energy is modified and how the engineering structures will behave during strong ground shaking.

The estimate of the contribution of surficial geology, particularly soft sediments, to the amplification of ground shaking has become a necessary requirement in seismic hazard reduction programs and also a fundamental component of regional seismic hazard maps. However, the characterization of ground shaking in terms of local site conditions is not an easy task, because of the different geologic materials and irregularly shaped earth structures formed by weathering, erosion, deposition and other geological processes near the surface of the earth (Aki, 1988).

At the present time, many techniques are available to evaluate the site effects: experimental methods, empirical methods, numerical simulations, and statistical analysis of existing accelerometric data. Each technique presents its own advantages and limitations. Numerical simulations, for example, allow the analysis of different parameters and the calculation of theoretical modeling for a large sample of possible input motions. Such an approach, however, requires an exhaustive understanding both of the geotechnical information of each site and of the sophisticated numerical analyses. The empirical approaches are instead based on the study of weak or strong motion data, recorded on sites with different local geology. These methods, very popular in regions of moderate to high seismicity, use the spectral ratios of earthquake recordings relative to a firm rock site, known as the "reference site" (Borcherdt, 1970). The spactral ratio method assumes that recordings from the reference site contain the same source and propagation effects as records

from the other sites. Therefore, the differences observed between sites are explained as being due to local site effects.

However, as underlined by several authors (Field and Jacob 1995, Boatwright et al., 1991, Harmsen, 1997a), identifying and separating source and site effects, is the greatest impediment to the spectral analysis of low and moderate magnitude earthquakes.

Andrews (1986), proposed a general inversion scheme to decompose the body-wave spectra into source, site and propagation components. Since the site amplification at a reference site is set to unity, this method provides results comparable with those obtained by the traditional spectral ratios. However, the application of such a procedure can present some problems. A reference site is not always available and, as shown by recent studies (Archuleta and Steidl, 1998; Steidl et al., 1996), reference sites may not have a completely flat amplitude response. For these reasons, a number of alternative methods that do not rely on a reference site, have been developed.

The first one employs the generalized-inversion method proposed by Boatwright et al. (1991), where shear-wave spectra are represented with a parameterized source, path-effect model and site-response term for each site. The source parameters for each event, the path-effect terms and the site effect for each site are inverted simultaneously, in the least-squares sense.

The Nakamura technique, instead, is based on the calculation of the spectral ratio between the horizontal and vertical components (H/V) of recorded ambient seismic noise (Nakamura, 1989; Bard, 1997), while the method proposed by Lermo and Chavez-Garcia (1993) involves dividing the horizontal-component shear-wave spectra at each site by the vertical-component spectrum observed simultaneously at that site (Langston, 1979; Field and Jacob, 1995).

Recently, the very large number of observations on the effects of soft soil on seismic response, has allowed researchers to develop empirical relations between surface geology and various measurements of an earthquake ground motion. These relationships, derived when information on both the earthquake observations and the surface geology are available, are very important because they can be applied to other locations, where only the surface geology is known. Additionally, several attempts have been made to obtain precise relationships between surface geology and local amplification factors. A simple method to evaluate the site conditions in ground-motion analyses and in earthquake scenario studies, is to use the shear-wave velocity in geologic units to develop site classifications. This technique allows an unambiguous classification of sites based on only parameter (Borcherdt, 1970; Joyner and Fumal, 1985; Boore et al., 1993). Shear-wave velocity is an effective measure of the quality of the foundation soil because it's dependent on basic physical properties such as density, porosity and degree of compaction of the materials through which the seismic waves propagate. To such purpose, many drilling programs were conducted in several areas

to establish important correlations between seismic response and average shear-wave velocity of various geologic units (Borchardt, 1994).

Joyner et al. (1981) have proposed that the design of structures can be based on the physical properties of the upper 30 m of soil, so that the average shear-wave velocities in the upper 30 m can be used as an indicator of the site response. Several authors (Boore et al., 1994; Boore and Joyner 1997) have based their ground motion regression on this concept.

The classification schemes specified by recent code provisions of the “Design recommendations for earthquake resistance of structures”, such as NEHRP Provisions, 1997 UBC and EC8, make use of site classes, with each site class being assigned according to a simple parameter, such as the average shear-wave velocity of the top 30 m (V_s^{30}), and the site dominant periods.

More recent works on the shaking response based on the surface geology type, provide site-category maps, where the geologic units have been grouped into several classes with similar V_s^{30} values (Tinsley and Fumal, 1985). In that contest, Borchardt (1994) has used the consistent relations between seismic response and various geologic units to find geologically-based, frequency and amplitude-dependent site corrections for future earthquake scenario studies. Those factors can be included into a probabilistic seismic hazard assessment to reach an improved estimate of ground motion that considers the effects of local site conditions.

The fundamental goal of this thesis is to provide an uniform site classification for the Campania-Lucania region (Southern Italy). Estimates of the site response were obtained applying experimental methods and empirical correlations based on the surface geology. The final results were compared to evaluate the accuracy of each method given the current level of information.

In order to introduce the role of geology in seismic hazard estimates at local scale, the available information about age, density and shear-wave velocities have been used to create some generalized sites classes, according to the European norm, Eurocode8 (EC8). These geologic information have been transferred on the 1:250,000 scale regional geologic map, where several geologic units with similar seismic response, were grouped together. The resulting map, built according to a simple classification proposed by Park and Ellrick (1998), subdivides the surface geology in four categories: Quaternary sediments (Q), Quaternary-Tertiary volcanic rocks (V), Tertiary sediments and soft rocks (T), and Mesozoic hard rocks (M).

In this thesis, 106 earthquakes with MI magnitude ranging from 1.5 to 3.5 were analyzed using recordings from 22 seismic stations of the Irpinia Seismic Network (ISNet).

In order to identify possible site effects at each seismic stations of the ISNet network, the stochastic simulation technique proposed by Boore (1983) has been used, to simulate ground motions

expected for a set of earthquakes having a specified magnitude and fault-station distance. Specific values of stress-drop and attenuation terms have been used to account for the tectonic features of the region of interest.

At each station, the observed peak ground-motion values (PGA and PGV) were compared with the simulated ones. In the hypothesis of a correct simulation of both source and propagation effects, using a large dataset, the residuals computed at each station provide a first-order measure of the site effect.

The residual values found by our analysis, were all different from zero. This important result suggests that the material properties near the surface in the Campania-Lucania region, can produce large modifications of the selected parameters.

Therefore, once the presence of site effects was verified, the site responses were computed using non-reference site methods. The shear-wave spectral records, corrected for the propagation path effect, were inverted using a non-linear inverse procedure based on the Simplex algorithm. The inversion starts by choosing a Brune's source model (1970) for each seismic event. Then, each source model divides the corresponding corrected amplitude spectrum of every event. This gives the site effect (Moya et al., 2000). Assuming that the site effects at any given site are the same, regardless of the seismic event, the average and the normalized standard deviation are finally calculated. In our instance, it was observed that site effects for stiff and soft sediments showed deamplification in the high-frequency range, while in rock sites they showed significant amplification for frequencies higher than 4-5 Hz.

The results of the inversion technique were compared with those computed using the horizontal-to-vertical (H/V) ratios for earthquake data. In most of cases, the site responses obtained with the two techniques were found to be similar in shape. Both methods were consistent in estimating the fundamental resonance frequency, even if the levels of amplification were very different. In particular, the lower level of amplification obtained by the H/V ratios at frequencies higher than the fundamental one, was due to the presence of converted waves.

Many authors agree that the H/V spectral ratio method gives only partial information on the site effects, such as the fundamental resonance frequency, while it does not yet an accurate estimate of the amplification factors, because of the unknown source and propagation effects (Lermo et al., 1993; Lermo et al., 1994). As a consequence, at each station, the site-amplification spectra obtained through the inversion method, were averaged within three frequency bands: the first-frequency band (Ib) from 1 to 5 Hz, the second-frequency band (IIb) from 5 to 10 Hz, and the third-frequency band from 10 to 20 Hz (Hartzell, et al., 1996a; Hartzell, et al., 1996b).

In order to correlate these average spectral levels with the surface geology, three site-response maps

have been created, one for each frequency band, displaying the mean amplification values over the QVTM site conditions map. Significant correlations with the three frequency bands have been found, suggesting that spectral amplification at a site is also influenced by the nature of near-surface materials. In particular, a correlation was found between larger site-response factors and lower average shear-wave velocity in the upper 30.

The maps represent the first attempt to produce estimates of site amplification for the Campania-Lucania region based on recorded ground motions. In addition, these simple geologically-based frequency and amplitude dependent site corrections factors, can be used to generate separate maps of the spatial distribution of peak ground motions (acceleration and velocity) as well as a maps of the instrumental seismic intensity. These maps, named as ShakeMap, provide information about the shaking for damaging earthquakes, useful to plan the emergency response, to estimate the losses, as well as to inform the public (Wald et al., 1999).

1.

Local effects on strong ground motion: main characteristics

1.1. Introduction

It has been recognized for a very long time that local site conditions can profoundly modify the main characteristics of strong ground motion (amplitude, frequency contents, and duration). Mallet (1862), for example, noted that the intensity of ground shaking in the 1857 Neapolitan earthquake was related to geologic surface conditions. Gutenberg (1927) was the first one to develop site amplification factors from recordings of microseisms at sites with different soil conditions. But, despite considerable evidences of the existence of site effects, provisions, specifically accounting for local site responses, did not appear in building codes until the 1970s. However, the broad availability of strong-motion instruments, has allowed local site effects to be measured and studied quantitatively in recent years.

The main local geologic factors that can affect the level of shaking experienced during earthquakes, are the surface topography, the basin geometry, and the geometry and the physical properties of the subsurface deposits.

The basic physical phenomena responsible for the site effects are briefly described in the following sections.

1.2. Surface topography effects

Evidences of topographic effects abound in literature. It has been often observed after destructive earthquakes, that the largest damages were found in correspondence of villages built on hill tops. Examples of such observations may be found in Brambati et al., 1980 (Friuli, Italy, 1976 earthquake), Siro, 1982 (Irpinia, Italy 1980 earthquake), and Celebi, 1987 (Chile, 1995 earthquake). There are also very strong instrumental evidences of topographic effects. Perhaps the best known example is that of some peak horizontal accelerations of about 1.25g, recorded during the 1971 San Fernando earthquake (Mw 6.6). These values, considerably larger than those expected for an earthquake of this magnitude, were ascribed to a topographic effect. In fact, since the accelerograph was installed at the top of the rock ridge, a large part of the recorded high peak accelerations was associated to the dynamic response of the ridge (Trifunac and Hudson, 1971).

Although many theoretical and numerical models have been developed, the study of topographic

effects is to this day, a complicated problem. In fact, the interaction of the seismic waves can produce a complex pattern of amplification and deamplification, depending on the topographic features and on the characteristics of the incident wavefield (wave type, frequency contents, incidence and azimuth angle).

Basically, the topographic effects can be connected to three physical phenomena:

1. the sensitivity of the surface motion to the incidence angle, usually large for SV waves around the critical angle. This effect was observed by Kawase and Aki (1990) and analyzed during the 1987 Whittier Narrows, California earthquake (MI 5.9);
2. the focusing or defocusing of seismic waves reflected along the topographic surface. Aki (1988) and Sanchez-Sesma (1990) estimated these topographic effects considering a simple example with a wedge-shaped medium. For a triangular infinite wedge subjected to vertically propagating SH-waves, the apex displacements are amplified by a factor $2\pi/\phi$, where ϕ is the vertex angle of the wedge;
3. the diffraction of body and surface waves which propagate downwards and outwards from the mountain tops, leads to interference phenomena between the direct and diffracted waves (Pedersen et al., 1994).

1.3. Basin geometry effects

The effects of basin geometry on ground motion are of great interest in geotechnical earthquake engineering. In fact, most urban settlements are located on or near alluvial valleys featuring young and soft deposits. The shape of a basin can trap the body waves and can cause some incident body waves to propagate through soft sediments as surface waves. These waves, subjected to multiple reflections along the edges, can produce stronger shaking and longer duration than those produced by S-waves.

Significant differences between the amplification functions at the center and edges of a valley have been observed in different earthquakes (e.g., Caracas 1967, San Fernando 1971, and Leninakan 1988). Additionally, many theoretical studies and analytical approaches (Bard and Gariel, 1986) have indicated that for alluvial valleys of irregular shape, the resulting ground motion can be very complex, even chaotic.

The potential differential ground motion across alluvial valleys, has important implications on the design of structures that are more sensitive to low frequency signals such as bridges or pipelines that often cross valleys. Differential movements can induce large loads and cause heavy damages.

1.4. Effects of soft surface layers: main characteristics

The ground-shaking produced by an earthquake in a given site basically depends on the event magnitude, the source-to-site distance, and the local geologic conditions. When a fault ruptures below the Earth's surface, body waves travel away from the source in all directions. Since the earth's crust is not homogeneous, but it's composed of a complex mixture of rocks and sediments of several types, as the waves reach the boundaries between different geologic materials, they are reflected and refracted. Near the ground surface, where the density and S-waves velocity are generally lower than in the materials beneath them, multiple refractions produce nearly vertical waves propagation. The fundamental phenomenon responsible for the amplification of the motion in soft soils, is the trapping of seismic waves, attributable to the impedance contrast between sediments and the underlying bedrock. The impedance contrast is defined as the ratio between density and S-waves velocity of different geologic materials.

The analysis of one-dimensional ground response are based on the assumption that the soil and bedrock surface is extended infinitely in the horizontal direction and that the soil deposit response is predominantly caused by SH-waves vertically propagating from the underlying bedrock. Most methods commonly used to compute the response of systems with one-degree of freedom, are based on the use of transfer functions. Transfer functions can be used to express several response parameters, such as displacement, velocity, acceleration, from an input motion parameter such as bedrock acceleration.

The bedrock motion (input) can be represented as a Fourier series. Each term in the Fourier series of the input is then multiplied by the transfer function to produce the Fourier series of the ground surface motion (output). Thus, the transfer function determines how each frequency in the bedrock motion is amplified, or deamplified, by the soil deposit. In the hypothesis of a uniform layer of isotropic soil overlying bedrock, the harmonic horizontal motion of the bedrock will produce shear waves traveling up and down in the surface layer (Figure 1.1).



Figure 1.1. Linear elastic soil deposit of thickness H overlying a rigid bedrock.

The resulting horizontal displacement can be expressed as:

$$u(z, t) = Ae^{i(\omega t + kz)} + Be^{i(\omega t - kz)} \quad (1.1)$$

where ω is the angular frequency of the ground shaking, k is the wave number, and A and B are the amplitudes of the waves traveling in the $-z$ (upward) and $+z$ (downward) directions, respectively.

At the free surface ($z = 0$), the shear stress, and consequently the shear strain, must vanish, and thus A must equal B .

The constructive interference of the upward and downward traveling waves produces *standing waves* of amplitude $2A \cos kz$, that have a fixed shape with respect to depth:

$$u(z, t) = 2A \cos kz e^{i\omega t} \quad (1.2)$$

Equation (1.2) can be used to define a transfer function that describes the ratio of the displacement amplitudes at any two points in the soil layer. Choosing these two points to be the top and bottom of the soil layer, the transfer function is given by:

$$F(\omega) = \frac{1}{\cos(\omega H/V_s)} \quad (1.3)$$

The amplification function is the modulus of the transfer function which indicates that the surface displacement is always at least as large as the bedrock displacement and, at certain frequencies, is much larger.

Thus $|F(\omega)|$ is the ratio of the free surface motion amplitude to the bedrock motion amplitude.

As $\omega H/V_s$ approaches $\pi/2 + n\pi$, the denominator of equation (1.3) approaches zero, which implies infinite amplification, or *resonance*. Therefore, the response of soft soil is strongly dependent upon the frequency of the base motion, and the frequencies at which great amplification occurs are related to S-wave velocities and the thickness of the soil layer.

At frequencies that approach the fundamental frequency of a soil deposit, the transfer function begins to take large values.

For one-layer 1D structures, the fundamental frequency is given by

$$f_0 = \frac{\beta}{4h} \quad (\text{fundamental}) \quad (1.4)$$

The n th natural frequency of the soil deposit is given by:

$$f_n = (2n + 1) \cdot f_0 \quad (\text{harmonics}) \quad (1.5)$$

where β is the S-wave velocity in the surface layer, h is the thickness, and n is an integer number characterizing the harmonic order.

The period of vibration corresponding to the fundamental frequency is called the *characteristic site period*,

$$T_s = \frac{4H}{\beta} \quad (1.6)$$

The characteristic site period depends on the thickness (H) and S-wave velocity (β) of the soil. It is a very important parameter because provides a useful indication of the period of vibration at which the most significant amplification can be expected.

It's possible to compute the site amplification using the quarter-wavelength approximation described by Boore and Brown (1998). That method estimates the amplification for a specific frequency, by calculating the impedance contrast between near-surface materials at a depth corresponding to a quarter of the wavelength, and using the material properties of the underlying bedrock. The amplitude is also associated to the characteristics of the wavefield (type of waves, angle of incidence, etc.). In the case of waves with vertical incidence, the maximum amplification reduces to:

$$A(f) = \sqrt{\frac{\rho_r \beta_r}{\rho \beta}} \quad (1.7)$$

In equation (1.7) ρ_r and β_r are the density and shear-wave velocity averaged from the surface to a depth corresponding to a quarter of the wavelength, and ρ and β are the density and velocity at the reference depth.

2.

Development of a map of geologically defined site-condition classes for the Campania-Lucania region (Southern Italy)

2.1. Introduction

In order to include site effects into regional hazard mapping, detailed site classifications must be developed so that the levels of site response within the same site class are similar.

Predicting ground shaking over a region in future earthquake scenario studies, typically involves empirical attenuation relations for a specific site class. Therefore, the existing relations must be adjusted, or new attenuation relations must be developed, in order to take into account potential modifications of ground shaking produced by site-specific conditions.

One of the classification schemes specified in engineering design codes, is based on measured geotechnical parameters, geological observations, and the natural periods of surface soil layers at the sites.

In recent years the shear-wave velocity (V_S) in the shallow subsurface materials, has become an important parameter to define site classifications and to predict spectral-amplification values.

V_S is an effective measure of the quality of foundation soils, because it is dependent on basic physical properties such as density, porosity and degree of cementation of the materials through which the seismic waves propagate. Consequently, several relationships have been derived to provide rough estimates of V_S . Joyner et al. (1981), for example, have suggested that the site conditions can be characterized by calculating the shear-wave velocity at a depth equal to one quarter of the wavelength of the period of interest. Using the mapping units and the observed variations of V_S with age, grain size and depth, Fumal and Tinsley (1985), have assigned an average shear-wave velocity to each geologic unit within a test area. Though the need to have detailed subsurface information, makes the quarter-wavelength method difficult to apply.

Recent works have recommended alternative methods that simplify the use of V_S in ground motion predictions. Borchardt et al. (1991) and Joyner and Fumal (1985), for example, have suggested that site conditions can be classified on the basis of the average shear-wave velocity to a depth of 30 m (V_s^{30}), in agreement with the typical depth that can be reached with drill rigs in a single day. In this way, sites are classified unambiguously by only one parameter.

Furthermore, Borchardt (1994) has used consistent relations between seismic response and the various geologic units, to find site dependent amplification factors based on V_s^{30} . These site

amplification factors based on V_s^{30} , have been included in attenuation equations (Boore et al., 1993) in order to generate predictive maps of strong ground shakings in earthquake hazard mitigation programs and to create automatic maps of the spatial distribution of peak ground motions for any significant earthquake.

Park and Elrick (1998) have used age units shown on geologic maps, and measured V_s^{30} as a starting point to classify geologic materials in Southern California. In particular, they have characterized three general categories with similar V_s^{30} values: Quaternary sediments (Q), Tertiary sediments and soft rocks (T), and Mesozoic hard rocks (M), which were chosen to correspond to the site-conditions terms in ground-motion attenuation equations.

Recent code provisions for buildings and other structures (1994 and 1997 NEHRP Provisions, 1997 UBC, Eurocode 8, or EC8, 2003), have defined site classifications based on a V_s^{30} value or range, and on site dominant periods.

This thesis presents a map of geologically defined site-condition classes for the Campania-Lucania region (Southern Italy). The site-conditions map has been prepared following the main rules proposed by Park and Elrick (1998). The geologic formations from 1:250,000 scale regional geologic map, have been classified into groups with similar age, grain size and correlated with shear-wave velocity categories proposed into Building codes. Because of the wide coverage of the map, and of the lack of V_s profiles in most geologic units, a simpler scheme of classification based on European code provisions (EC8) has been followed. Only four general categories have been grouped: Quaternary sediments (Q), Quaternary-Tertiary volcanic rocks (V), Tertiary sediments and soft rock (T), and Mesozoic hard rocks (M). These categories have been overlapped on a 1:250,000 scale regional geologic map, tracing only the geologic contacts that separate units of different categories.

It is clear that more shear-wave velocity measurements and more detailed geologic mappings are necessary to develop more shear-wave velocity categories. However, the statewide the site classification map provides a first approximation of shallow materials properties that can be used as are or in conjunction with other factors, to calculate probabilistic seismic hazard programs.

2.2. Geological setting of the Campania-Lucania region - Southern Apennine

The Southern Apennine chain is a Neogene east-verging thrust belt formed as the result of the west-dipping subduction of the Apulian-Ionian lithosphere (Doglioni et al., 1996). The belt is associated with the Tyrrhenian back-arc basin to the west and with the Bradano foredeep to the east. During

the middle Miocene-upper Pliocene, several compressive tectonic phases associated with the collision between the African and European margin, have determined thrusting and piling of different units toward stable domains of the Apulo-Adriatic foreland. From late Tortonian to Quaternary, all the system rapidly migrates “eastward” as a consequence of the retreating of the sinking foreland lithosphere (Patacca and Scandone, 1989, Patacca et al., 1990; Pescatore et al., 1999).

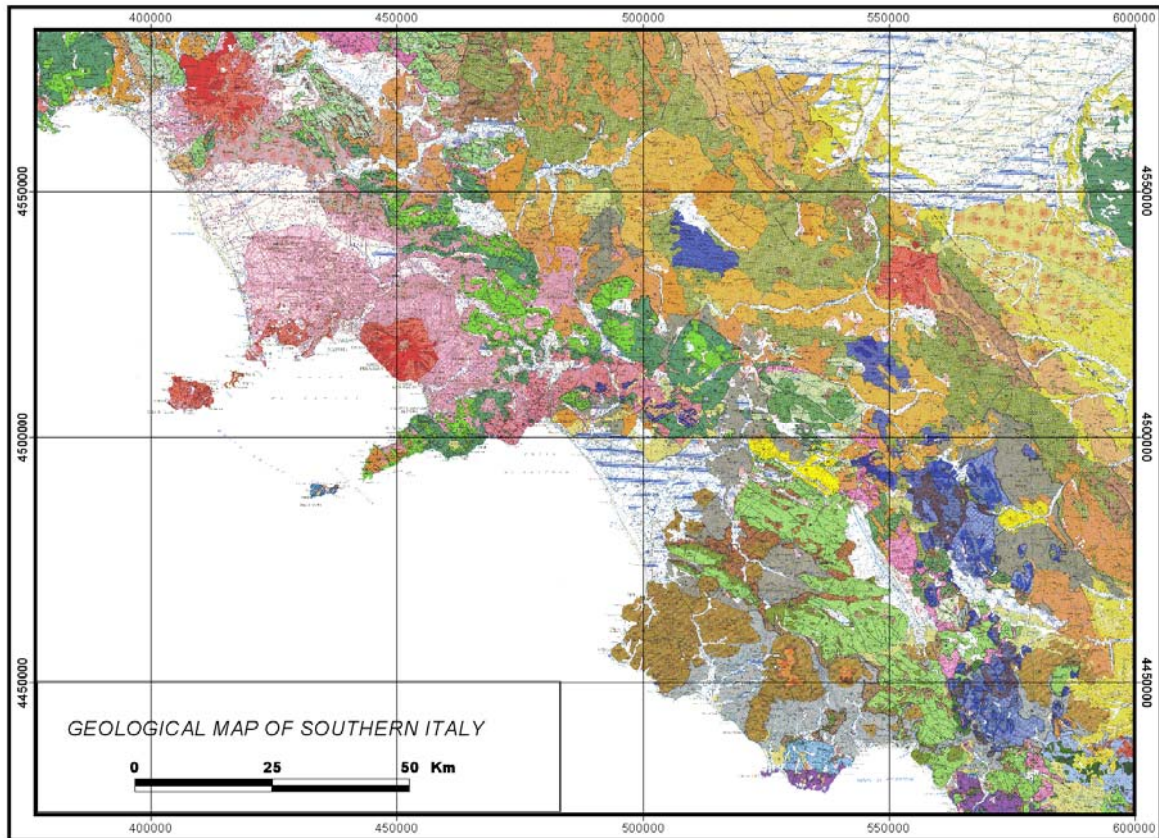
The structural complexity of the Campania-Lucania region, is due to different paleogeographic domains involved in the Southern Apennine thrust belt building. The basinal facies terrains have been involved in ductile deformations, while the carbonate platform sequences in brittle deformations. In addition, the deformation did not proceed cylindrically but it was characterized by out-of-sequence thrust-propagation processes (Roure et al., 1991).

During the upper Pliocene-lower Pleistocene, the tectonic evolution has determined the mountain chain subdivision into the NNW-SSE-trending Molise-Sannio, and the WNW-ESE-trending Campania-Lucania region. Afterwards, in the Middle-Pleistocene, the Southern Apenninic wedge has uplifted and involved in a NE-SW extensional tectonic event. This stress regime has determined the development of large extensional and transtensional structures and it is still active and responsible of the present-day seismicity of the Southern Apennine region (Anderson and Jackson, 1987).

The main units in outcropping in the Southern Apennine can be grouped in four belts. From east to west the following units outcrop area can be identified as (Figure 2.1):

1. successions with basinal to marginal facies, in age from Cretaceous to Miocene, tectonically lying on Plio-Pleistocene foredeep deposits;
2. successions with shallow-water, basinal and shelf-margin facies, ranging in age from middle Triassic to Miocene (‘Lagonegro units’), overthrust on the previous ones;
3. Triassic to Miocene carbonate platform successions (‘Apenninic platform units’), overthrust on the Lagonegro units;
4. Jurassic–Cretaceous to Miocene deep-water successions (ophiolite or ‘internal’ units and associated siliciclastic wedges), outcropping on the Tyrrhenian belt and the Calabria–Lucania boundary, overthrust on the Apenninic platform units.

All these units tectonically lie on the buried Apulian platform. Moreover, volcanic rocks are extensively diffused in the Campania-Lucania region. The main volcanic vents are: the Campi Flegrei, an active volcanic complex located on the eastern border of the region, the Somma-Vesuvio, an active volcano in the central area, and the Vulture a not active volcano located on the western border of the region.



QUATERNARIO - QUATERNARY

Depositi Sedimentari - Sedimentary Deposits

- 1 Spazzie e dune costiere. Olocene
Beaches and coastal dunes. Holocene
- 2 Alluvioni, sedimenti lacustri e lagunari. Olocene
Alluvial, lacustrine and coastal lake sediments. Holocene
- 3 Detriti di falda, alluvioni, aree in frana. Olocene
Talus breccias, alluvium, landslides. Holocene
- 4 Travertini. Olocene - Pleistocene
Travertines. Holocene - Pleistocene
- 5 Depositi marini. Pleistocene superiore
Marine Upper Pleistocene
- 6 Depositi marini terrazzati, dune, spiagge. Pleistocene medio-superiore
Terraced marine deposits, dunes, beaches. Upper-Middle Pleistocene
- 7 Depositi alluvionali terrazzati. Pleistocene medio-superiore
Terraced alluvial deposits. Upper-Middle Pleistocene
- 8 Detriti di falda cementati, arena rossa. Pleistocene superiore
Talus breccias, "terra rossa". Upper Pleistocene
- 9 Conglomerati e sabbie terrazzati. Pleistocene medio-inferiore
Terraced conglomerates and sands. Middle-Lower Pleistocene
- 10 Depositi lacustri terrazzati. Pleistocene medio-inferiore
Terraced lacustrine deposits. Middle-Lower Pleistocene
- 11 Conglomerati alluvionali distali. Pleistocene medio-inferiore
Talus alluvial conglomerates. Middle-Lower Pleistocene

Vulcanico - Volcanic

- 12 Depositi vulcanici - sedimentari
Volcanic - sedimentary deposits
- 13 Depositi prodotti da caduta
Pyroclastic fall deposits
- 14 Proclastiti da fusi (ignimbrite Campana)
Pyroclastic flow deposits (Campanian ignimbrite)
- 15 Aree proclastite da fusi, Surges, Lahars
Other Pyroclastic Flows, Surges, Lahars
- 16 Isolaletti (Isola di Procida)
Islets (Procida Island)
- 17 Lave pahoehoe (Serie stromboliane)
Pahoehoe lavas (Strombolian series)
- 18 Lave ultrapahoehoe (Serie basaltico-nautiche e tufoidee)
Ultrapahoehoe lavas (Basaltic-nautic and tuffaceous series)
- 19 Lava sodico - potassiche del Ma Vulture (Serie basaltiche e basaltiche)
Sodic - potassic lavas of Ma Vulture (Basaltic and basaltic series)

AVAMPASSE APULIO-GARGANICO

APULIA-GARGANO FORELAND

- 20 Catene di bioclastiche e organogene (Catareni di Aprona)
Biostratigraphic calcarenites (Catareni di Aprona). Upper Miocene
- 21 Catene di Nummuliti (Calcine di Peschio). Eocene-Paleocene
Nummulitic calcarenites (Calcine di Peschio). Eocene-Paleocene
- 22 Calcini a Rudisti. Cretacico superiore
Auriculo-Limonites. Upper Cretaceous
- 23 Calcini di piattaforma (alla sommità orizzonte bauleudo decorato). Cretacico inferiore (al Gargano include il Malm)
Carbonate platform deposits (patina bauleudo decorato at the top). Lower Cretaceous (at Gargano includes the Upper Jurassic)
- 24 Magnesiani magnesiane e melastellaniche (Punta delle Pietre Nere, Gargano). Paleocene
Magnesian and melastellan magnesian (Punta delle Pietre Nere, Gargano). Paleocene
- 25 Calcini con sabbie e rudimenti carbonatici. Cretacico
Cherty and rudimental carbonates. Cretaceous
- 26 Rudimenti carbonatici. Cretacico inf.-Malm
Remnants carbonates. Cretaceous-Malm
- 27 Carbonati di Scogliera. Cretacico inf.-Malm
Reef Carbonates. Lower Cretaceous-Malm

AVANFOSSA E BACINI INTRAPPENNINICI PLIO-PLEISTOCENI

PLIO-PLEISTOCENE FOREBEE AND INTRAPPENNINIC BASINS

- 28 Unità Brindane (co Faldone di Monte Marone e Conglomerati di Marina). Pleistocene inf. (B) Argille sottappenniniche. Pleistocene inf. (a) Calcarenite di Gravina. Pleistocene inf. - Pleistocene medio-sup.
Brindane Unit (co Faldone di Monte Marone and Conglomerati di Marina). Lower Pleistocene. (B) Subappennine Clays. Lower-Middle Pleistocene
- 29 Unità di Calvello. Sabbie ad argille. Pleistocene inferiore-Pleistocene medio-inferiore
Calvello Unit. Sands and clays. Lower Pleistocene-Lower Pleistocene

CATENA APPENNINICA - APPENNINIC CHAIN

UNITÀ LITOSTRATIGRAFICHE NEOGENICHE DA PRE-ALTAI TO CROZANZA

NEOGENIC LITHOSTRATIGRAPHIC UNITS, FROM PRE-ALTAI TO CROZANZA

- 30 Unità di Ariano. Pliocene medio-inferiore
Ariano Unit. Middle-Lower Pliocene
- 31 Unità di Aliphan. Pliocene inferiore-Tortoniano superiore, separate da una discontinuità non cartografata.
Aliphan and Tortoniano Units (separated by a non cartographically reported in the past). Lower Pliocene-Upper Tortonian
- 32 Unità di Proconce (segue in corrispondenza a 45). Miocene superiore
Proconce Unit (follows conformity on 45). Upper Miocene
- 33 Formazioni di Pietraroja, Longano, Casiano (spaziano in discontinuità su 46). Tortoniano-Langhiano
Pietraroja, Longano, Casiano formations (read discontinuity on 46). Tortonian-Langhian
- 34 Formazioni di Serravallo - Fiano (Unità ipone esterne, seguono in corrispondenza su 43 e 54). Tortoniano inferiore-Langhiano superiore
Serravallo - Fiano formations (external units, follow conformity on 43 and 54). Lower Tortonian - Upper Langhian
- 35 Formazioni di Grotteferrate - Gorgoglione - Casizzo - San Ruffino
Grotteferrate - Gorgoglione - Casizzo - San Ruffino formations (in discontinuity with unit 36)
- 36 Formazioni di Riva Lagno (segue in corrispondenza su 63 e Monte Sarno). Serravallo-Langhiano superiore
Riva Lagno formations (follows conformity on 63 and Monte Sarno). Serravallo-Langhian Upper
- 37 Formazioni di Monte Sarno. Miocene superiore-medio (7) Monte Sarno Formations. Upper-Middle Miocene (7)
- 38 Onassi (off-shore di Monte Certaurino)
Onassi (off-shore of Monte Certaurino)
- 39 Onassi (entro di Monte Certaurino)
Onassi (within of Monte Certaurino)
- 40 Onassi (entro di Monte Sarno)
Onassi (within of Monte Sarno)
- 41 Formazioni di Aliphan, San Mauro, Pollica, Langhiano-Burdigaliano superiore
Aliphan, San Mauro, Pollica Formations. Langhian-Upper Burdigalian
- 42 Formazioni di Riva Lagno, "Vigilia a discesa", "Burdigaliano inferiore" - "Rivigliano". Burdigalian
Formations of Riva Lagno, "Vigilia a discesa", "Burdigaliano inferiore", "Rivigliano". Burdigalian
- 43 Formazioni di Blando e Certaurina (spaziano in corrispondenza su 67 e 68). Burdigaliano inf. (7)-Aquilatano
"Vigilia Numuliti" (segue in corrispondenza su 54). Langhiano-Oligocene superiore
"Blando-Upper" (segue in corrispondenza su 54). Langhian-Upper Oligocene

UNITÀ TETTONICHE DERIVATE DALLA DEFORMAZIONE DEI

DOMINI APPENNINICI ESTERNI

TECTONIC UNITS RESULTING FROM THE DEFORMATION OF THE

EXTERNAL APPENNINIC DOMAINS

- 44 Unità M. Alpi (Calcini di piattaforma). Cretacico inferiore-Giurassico superiore
M. Alpi Unit (Carbonate platform deposits). Lower Cretaceous-Upper Jurassic
- 45 Unità Molisane (invertebrati depositi di bacino). Miocene superiore
Molise Unit (invertebrate basin deposits). Upper Miocene-Cretaceous (pending to upper Triassic in the subsurface)

Unità Matese-Monte Maggiore - Matese-Monte Maggiore Unit

- 46 (a) Calcini a Rudisti. Cretacico superiore (B) Rudimenti carbonatici da sabbie a grossolane. Paleocene-Cretacico superiore (a) Rudisti (invertebrati). Upper Cretaceous. (B) Carbonate remnants. From fine to coarse. Paleocene-Upper Cretaceous
- 47 Isuati
Isuati
- 48 Calcini di piattaforma (al Matese occidentale includono depositi di mare più profondo). Cretacico inferiore-Lias medio
Platform carbonates (at Western Monte Maggiore include water deposit). Lower Cretaceous-Middle Liassic
- 49 Dolomie e calcari dolomitici. Lias inferiore-Trias superiore
Dolomites. Lower Liassic-Upper Triassic

Unità Lagonegrese. Carbonati e rudimenti carbonatici con

selce, radiolari, marne, argille.

Lagonegrese Units. Cherty carbonates and rudiments, radiolarians,

marls, clays.

Unità Lagonegro I - Lagonegro I Unit

- 50 "Scisti di Roccamare". Paleocene-Cretacico superiore
"Scisti di Roccamare". Paleocene-Upper Cretaceous
- 51 "Flysch Galesano". Cretacico inferiore
"Flysch Galesano". Lower Cretaceous
- 52 "Scisti Silice". Giurassico-Trias superiore
"Scisti Silice". Jurassic-Upper Triassic
- 53 "Calcini con selce". Trias superiore
"Calcini con selce". Upper Triassic

Unità Lagonegro II - Lagonegro II Unit

- 54 "Flysch Rosso". Oligocene-Cretacico superiore (può includere terreni di lago. Sicile alle Molise)
"Flysch Rosso". Oligocene-Upper Cretaceous (may include Sicilian and/or Molise type sequences)
- 55 "Flysch Galesano". Cretacico inferiore
"Flysch Galesano". Lower Cretaceous
- 56 "Scisti Silice". Giurassico
"Scisti Silice". Jurassic
- 57 "Calcini con selce". Giurassico inferiore-Trias superiore
"Calcini con selce". Lower Jurassic-Upper Triassic

Formazioni di Monte Fato. Trias medio ad inferiore

Monte Fato Formations. Middle and Lower Triassic

Terreni Lagonegrese indifferenziati (frange tettoniche del Monte

Picentino)

Uniframmentati agono-sequenziali (Monte Picentino and/or

Monte Marzano - Monti della Maddalena Unit

- 60 (a) Calcini a Rudisti. Cretacico superiore. (B) Rudimenti carbonatici. Eocene-Cretacico inf.
Rudimenti carbonatici. Upper Cretaceous. (B) Carbonate remnants. Eocene-Cretaceous
- 61 Depositi carbonatici di piattaforma e di margine. Cretacico inferiore-Lias
Carbonate platform and margin deposits. Lower Cretaceous-Liassic
- 62 Dolomie e calcari dolomitici. Lias inferiore-Trias superiore
Dolomites. Lower Liassic-Upper Triassic

Unità Monti Picentini-Taburno (inclusi gli Aurunci occidentali)

Monti Picentini-Taburno Unit (including western Aurunci Mountains)

- 63 Calcini a Rudisti. Cretacico superiore (agli Aurunci orientali, Taburno e Trias include anche il Paleocene). al Taburno e al Trias sono diffusi i rudimenti carbonatici.
Rudimenti carbonatici. Upper Cretaceous (in the Eastern Aurunci Mountains, at Taburno and Trias Mountains carbonate rudiments are common)
- 64 Depositi carbonatici di piattaforma (rudimenti carbonatici diffusi al Taburno e al Trias). Cretacico inferiore-Lias
Carbonate platform deposits (carbonate rudiments common at Taburno and Trias). Lower Cretaceous-Liassic
- 65 Dolomie, marne e calcareniti, sabbie bituminose. Lias inferiore-Trias superiore
Dolomites, marls and calcarenites, bituminous sands. Lower Liassic-Upper Triassic

Unità Monte Foroporta - Monte Foroporta Unit

- 66 Dolomie e rudimenti carbonatici, talco con selce. Giurassico-Trias superiore
Dolomites and rudimental carbonates, talc with selce. Jurassic-Upper Triassic

Unità Alburno - Cervati - Pollino

Alburno - Cervati - Pollino Unit

- 67 Calcini e marne (Formazione di Terranova). Eocene inferiore-Paleocene
Invertebrati and marls (Terranova Formation). Lower Eocene-Paleocene
- 68 Calcini di piattaforma, localmente rudimenti carbonatici. Cretacico superiore-Lias medio
Platform carbonates, locally rudimental carbonates. Upper Cretaceous-Middle Liassic
- 69 Dolomie e calcari dolomitici. Lias inferiore-Trias superiore
Dolomites. Lower Liassic-Upper Triassic

Unità San Donato - San Donato Unit

Metalcalci e metadolomie, flysch. Cretacico-Trias medio

Capri - Monte Marina and Bulgheria - Verbicario Units

Metalcalci e metadolomie, flysch. Cretacico-Trias medio

Capri - Monte Marina and Bulgheria - Verbicario Units

- 70 Calcini con sabbie e rudimenti carbonatici, marne ("scaglioli"). Oligocene-Cretacico superiore. (a) Capri - Monte Marina. (B) Bulgheria-Verbicario
Cherty sandstones and carbonate rudiments, marls ("scaglioli"). Oligocene-Upper Cretaceous. (a) Capri - Monte Marina. (B) Bulgheria-Verbicario
- 71 Vulcaniti basaltiche (Monte Carvino)
Basaltic volcanics (Monte Carvino)
- 72 "Calcini ad Elipagione", rudimenti carbonatici e calcini con selce. Cretacico inferiore-Lias medio (al Capri-Monte Marina. (B) Bulgheria-Verbicario)
"Calcini ad Elipagione", carbonate rudiments and cherty sandstones. Lower Cretaceous-Middle Liassic (at Capri-Monte Marina. (B) Bulgheria-Verbicario)
- 73 Dolomie e calcari dolomitici. Lias inferiore-Trias superiore
Dolomites. Lower Liassic-Upper Triassic

Unità Capri - Monte Marina and Bulgheria - Verbicario Units

Metalcalci e metadolomie, flysch. Cretacico-Trias medio

Capri - Monte Marina and Bulgheria - Verbicario Units

Metalcalci e metadolomie, flysch. Cretacico-Trias medio

Capri - Monte Marina and Bulgheria - Verbicario Units

Metalcalci e metadolomie, flysch. Cretacico-Trias medio

Capri - Monte Marina and Bulgheria - Verbicario Units

Metalcalci e metadolomie, flysch. Cretacico-Trias medio

Capri - Monte Marina and Bulgheria - Verbicario Units

Metalcalci e metadolomie, flysch. Cretacico-Trias medio

Capri - Monte Marina and Bulgheria - Verbicario Units

Metalcalci e metadolomie, flysch. Cretacico-Trias medio

Capri - Monte Marina and Bulgheria - Verbicario Units

Metalcalci e metadolomie, flysch. Cretacico-Trias medio

Capri - Monte Marina and Bulgheria - Verbicario Units

Metalcalci e metadolomie, flysch. Cretacico-Trias medio

Capri - Monte Marina and Bulgheria - Verbicario Units

Metalcalci e metadolomie, flysch. Cretacico-Trias medio

Capri - Monte Marina and Bulgheria - Verbicario Units

Metalcalci e metadolomie, flysch. Cretacico-Trias medio

Capri - Monte Marina and Bulgheria - Verbicario Units

Metalcalci e metadolomie, flysch. Cretacico-Trias medio

Capri - Monte Marina and Bulgheria - Verbicario Units

Metalcalci e metadolomie, flysch. Cretacico-Trias medio

Capri - Monte Marina and Bulgheria - Verbicario Units

Metalcalci e metadolomie, flysch. Cretacico-Trias medio

Capri - Monte Marina and Bulgheria - Verbicario Units

Metalcalci e metadolomie, flysch. Cretacico-Trias medio

Capri - Monte Marina and Bulgheria - Verbicario Units

Metalcalci e metadolomie, flysch. Cretacico-Trias medio

Capri - Monte Marina and Bulgheria - Verbicario Units

Metalcalci e metadolomie, flysch. Cretacico-Trias medio

Capri - Monte Marina and Bulgheria - Verbicario Units

Unità Nord-Calabrese - Norm-Casabian Unit

Formazioni del Saraceno, delle Crete Nere, di Tempa della Mungia,

successioni ad affinità siciliote. Oligocene-Malm

Saraceno-Crete Nere, Tempa della Mungia Formations. Sicilote type

successions. Oligocene-Malm

Unità Sicilidi - Sicilide Unit

Calcareniti, calcareniti, arenaglie variegato, arenarie. Miocene inferiore-

Cretacico

Calcarenites, calcarenites, variegated clay, sandstones. Lower Mio-

cene - Cretaceous

Unità Sicilidi - Sicilide Unit

Calcareniti, calcareniti, arenaglie variegato, arenarie. Miocene inferiore-

Cretacico

Calcarenites, calcarenites, variegated clay, sandstones. Lower Mio-

cene - Cretaceous

Unità Sicilidi - Sicilide Unit

Calcareniti, calcareniti, arenaglie variegato, arenarie. Miocene inferiore-

Cretacico

Calcarenites, calcarenites, variegated clay, sandstones. Lower Mio-

cene - Cretaceous

Unità Sicilidi - Sicilide Unit

Calcareniti, calcareniti, arenaglie variegato, arenarie. Miocene inferiore-

Cretacico

Calcarenites, calcarenites, variegated clay, sandstones. Lower Mio-

cene - Cretaceous

Unità Sicilidi - Sicilide Unit

Calcareniti, calcareniti, arenaglie variegato, arenarie. Miocene inferiore-

Cretacico

Calcarenites, calcarenites, variegated clay, sandstones. Lower Mio-

cene - Cretaceous

Unità Sicilidi - Sicilide Unit

Calcareniti, calcareniti, arenaglie variegato, arenarie. Miocene inferiore-

Cretacico

Calcarenites, calcarenites, variegated clay, sandstones. Lower Mio-

cene - Cretaceous

Unità Sicilidi - Sicilide Unit

Calcareniti, calcareniti, arenaglie variegato, arenarie. Miocene inferiore-

Cretacico

Calcarenites, calcarenites, variegated clay, sandstones. Lower Mio-

cene - Cretaceous

Unità Sicilidi - Sicilide Unit

Calcareniti, calcareniti, arenaglie variegato, arenarie. Miocene inferiore-

Cretacico

Calcarenites, calcarenites, variegated clay, sandstones. Lower Mio-

cene - Cretaceous

Unità Sicilidi - Sicilide Unit

Calcareniti, calcareniti, arenaglie variegato, arenarie. Miocene inferiore-

Cretacico

Calcarenites, calcarenites, variegated clay, sandstones. Lower Mio-

Figure 2.1. Geological map of Southern Italy (Bonardi G., B. D'Argenio, and V. Perrone - 74° Congress of the Geological Society of Italy).

2.3. Historical and recent seismicity

The Southern Apennine is an active tectonic region of Italy that accommodates the differential motions between the Adria and Tyrrhenian microplates, to which almost all of the seismicity occurring in this region can be ascribed.

Most of the earthquakes of the Campania-Lucania region are located into the narrow upper-crustal seismic zone (30-50 km). In particular, two different clusters of crustal earthquakes are identified: the westernmost with shallow earthquakes (depths < 20 km) centred on the axis chain (Irpinia area) and the easternmost with deeper earthquakes (about 20-40 km) located on the outer margin of the chain (Potentino area) and the foredeep. These earthquakes have different focal solutions indicating a pure extensional regime, to the west (Irpinia area), and strike-slip regime, to the east (Potentino area). Moreover, it is possible recognize a third zone, located within the Appenninic chain from the Vallo di Diana to the Agri Valley, characterized by low seismicity (Figure 2.2a).

Historically, the Southern Apennine has experienced numerous large disastrous events, among which there are those that are occurred in 1694, 1851, 1857 and 1930, with the most recent event represented by the Irpinia earthquake (23 November, 1980, M 6.9), that resulted in about 3.000 deaths and huge damage (Westaway and Jackson, 1987; Bernard and Zollo, 1989).

The locations and magnitude of the historic earthquakes retrieved from the Catalogo dei Forti Terromoti in Italia (CFTI) (Boschi et al. 1997) are shown in Figure 2.2b.

More recent studies indicate that the 1980' faulted area is currently interested by an intense seismic activity with the occurrence of low to moderate events. In the recent past, moderate magnitude events are also occurred within or near at border of the multiple fault systems, the 1990 and 1991 Potenza earthquake (M 5.4 and 5.1 respectively), and the 1996 event (M 4.9). This recent seismicity indicates that the Campania-Lucania region has a high probability of occurrence for $M \geq 5.5$ earthquakes, and therefore represents a region with a high seismic risk level also for the future (Cinti *et al.*, 2004).

Recordings of small to moderate size events located in the fault zone, can be used to produce study aimed at understanding and modeling the physics of the site effects at local and regional distances, that can be used for computing reliable deterministic and/or probabilistic strong ground motion scenarios for moderate to large magnitude events occurring in Irpinia area (Zollo et al., 2004).

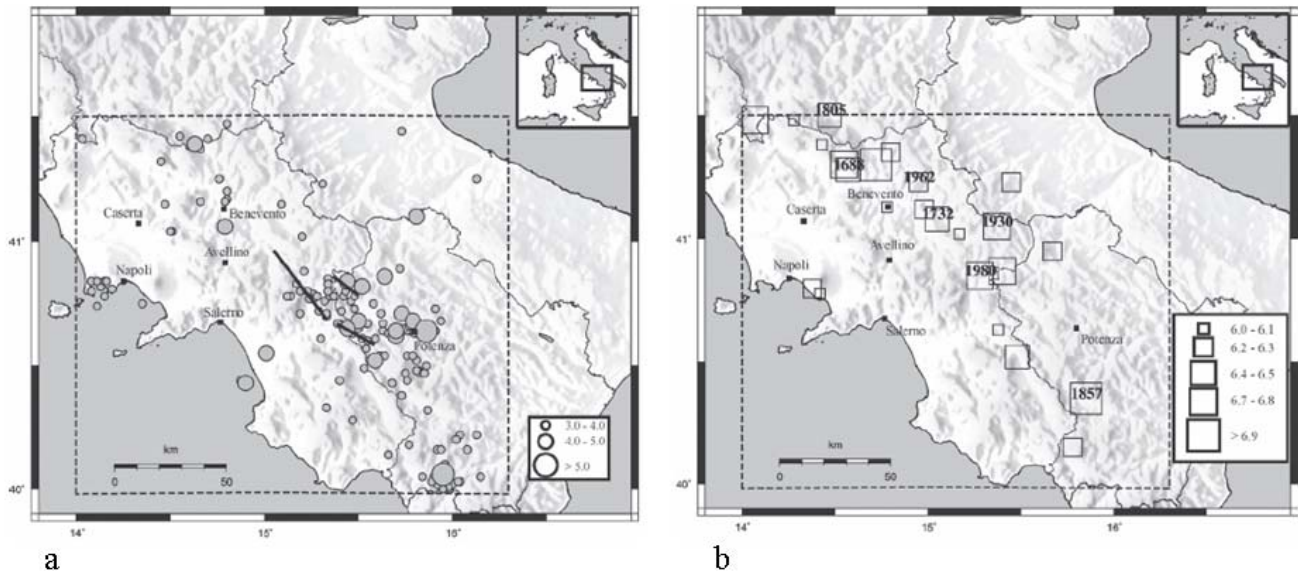


Figure 2.2a). Map of recent instrumental seismicity with $M > 2.5$ recorded by the INGV in the period 1981–2002 in the region defined by the dashed rectangle. Dimensions of the circles are proportional to magnitude. The black lines represent the surface projection of the three fault segments that broke in the 23 November 1980 earthquake (M 6.9) (Weber et al., 2007).

2.2b). Locations of the main historical earthquakes retrieved from the CFTI database within the region defined by the dashed rectangle. The box dimensions are proportional to magnitude. The best-constrained historical earthquakes are reported along with their date of occurrence (Weber et al., 2007).

2.4. Site-conditions map for Campania-Lucania region

One motivation of this thesis is to provide a site-conditions map for the Campania-Lucania region, based on surface geology and on shear-wave velocities. In order to generate a site-conditions map for use as a V_S category map, it is important to select an appropriate geologic map.

The most detailed available geologic maps are, usually, at 1:25,000 scale. Commonly, geologic maps show units that are distinguished by their ages, lithologies, grain size, and other factors that may be correlated with V_S . Although the most detailed geologic mapping may provide a better site-conditions map, it was chosen to use a larger albeit less detailed map in order to completely cover the region of interest with a single map. Thus, the site-conditions map for the Campania-Lucania region, has been digitized and generalized from a 1:250,000 scale regional map.

In general, a digital site-conditions map is generated grouping geological formations of similar age and physical properties (grain size, density, and shear-wave velocity), as proposed by Park and Elrick (1998).

The geologic units shown on the 1:250,000 scale geologic map of the Campania-Lucania region

(Bonardi et al.), were sorted into four different categories on the basis of lithological and age criteria. The resulting four classes, that are expected to have similar V_S , are: Quaternary sediments

(**Q**), Quaternary-Tertiary volcanic rocks (**V**), Tertiary sediments and soft rock (**T**), and Mesozoic hard rocks (**M**).

In order to compile a digital site-conditions map, the four categories (QVTM) have been overlapped on the 1:250,000 scale regional map, tracing only the geologic contacts that separate units of different categories. The resulting QVTM map (Figure 2.3) is an extension of the geological classification proposed by Park and Ellrick (1998), because of the presence of volcanic rocks widely spread in the studied region.

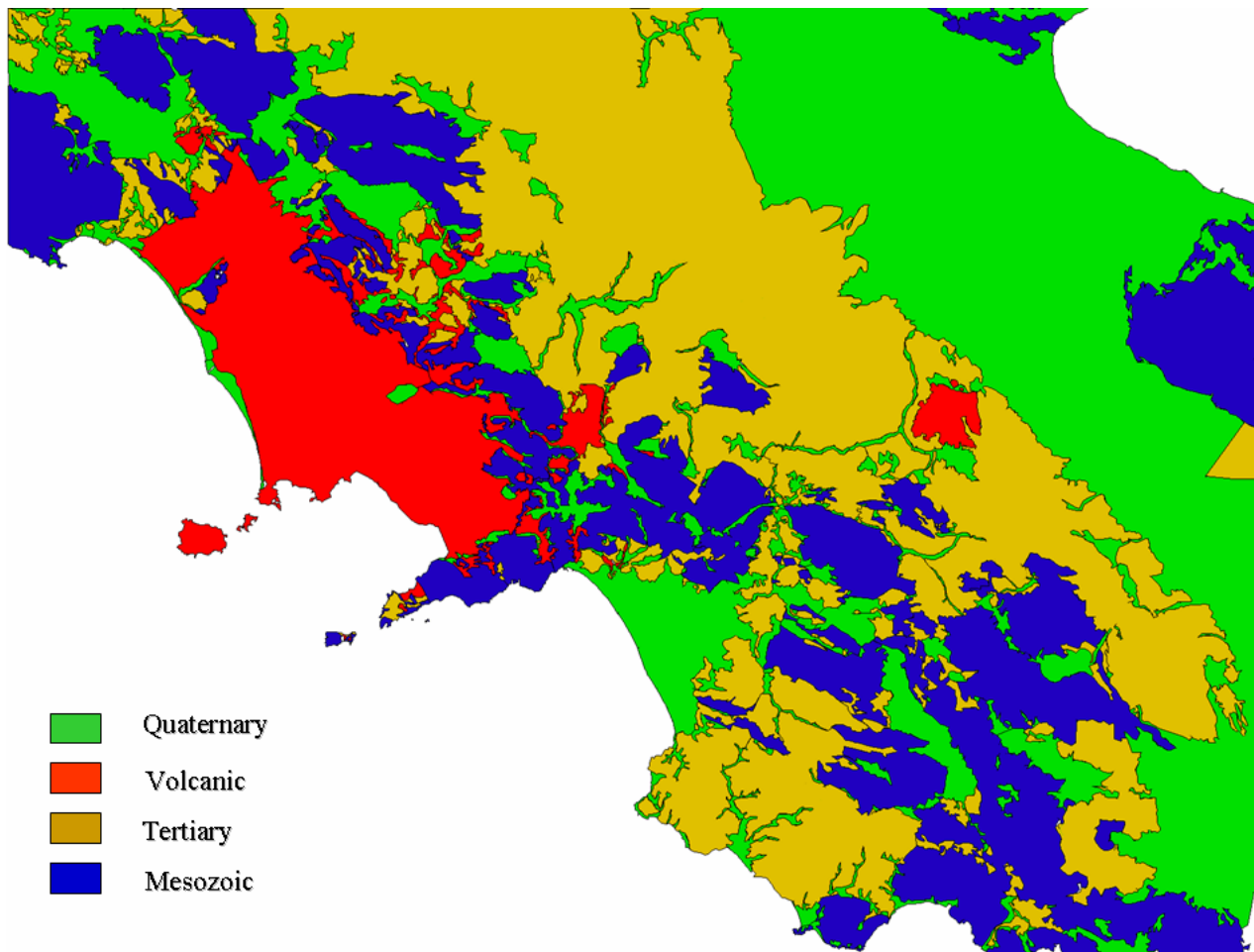


Figure 2.3. The QVTM site-conditions map.

In order to develop a V_S site classification, it is necessary to assemble a database of V_S profiles, and use V_S^{30} to characterize each site class.

The fundamental complication with this approach is that shear-wave velocities are only measured at

discrete points, and some method of extrapolation is necessary for any point other than the sampled ones. Sometimes, there are too few measurements in a given geologic unit in order to adequately characterize its response. Or two geologically distinct units may have similar velocity distributions and thus exhibit similar responses.

Many efforts were devoted to collect enough geotechnical information to assemble a database of V_S profiles for the Campania-Lucania region. Data concerning V_S profiles as a function of depth and density values for each layer, were obtained from geological, geotechnical and geognostic data, when available.

For a profile of soil or rock, the representative average V_S^{30} is, generally, computed from the time taken by the shear-wave to travel from a depth of 30 m to the ground surface:

$$V_{S,30} = \frac{30}{\sum_{i=1,N} \frac{h_i}{V_i}} \quad (2.1)$$

where h_i and V_i denote the thickness (m) and shear-wave velocity (m/s) of the i th formation or layer, in a total of N , existing in the top 30 meters.

Since ideally all shear-wave velocity profiles must reach the depth of 30 m, it has been possible to calculate an average shear-wave velocity, using equation (2.1) only for sites with a depth of at least 30 m. Moreover, because V_S profiles have been measured in relatively few geologic units, at some sites the V_S^{30} have been inferred from velocity measurements in near boreholes in similar materials at comparable depths. In other cases, V_S^{30} values were instead extrapolated from measures at sites with similar age and materials.

Regarding the volcanic area, density and shear-wave velocity data was extrapolated and collected from several published reports (Nunziata et al., 2004; Nunziata et al., 2006), since they were not available at the time of writing. Following these general rules, V_S^{30} value or range, has been assigned to each site class.

Table 2.1 shows the assigned QVTM site classes to geologic units in outcrop in the studied region, according to the site classification proposed by EC8. The four categories were also defined by the V_S^{30} and by the dominant site period.

The dominant period has been estimated as four times the S-wave travel time in the soil layer, assuming that the site can be represented by a single soil layer, 30 m in width, with a constant shear-wave velocity, to a first order approximation. The natural period value or range, is an important site descriptor because it provides a set of parameters of engineering interest, such as for example the spectral ordinates $S_a(T)$, used to differentiate ground conditions in the seismic shaking hazard.

Ground Type	Age	Site Natural Period (sec)	V_{s30} (m/s)	Subsoil class in EC8
Carbonate platform successions	Mesozoic	$T < 0.15$	> 800	A
Sediments, soft rocks and flysh deposit	Tertiary	$0.15 = T < 0.3$	360-800	B
Volcanic rocks	Quaternary- Tertiary	$0.12 = T < 0.3$	360-1000	B
Alluvium and gravel deposits	Quaternary	$0.3 = T < 0.6$	180-360	C
Very soft soils	Quaternary	$T = 0.6$	< 180	D

Table 2.1. Site Class Definitions for the Campania-Lucania region and the corresponding EC8 Site Classes (2003)

The site-conditions map for the Campania-Lucania region presented in this thesis, shows the general geologic categories alluvium, soft rock, and hard rock, which are correlated with the terms used in strong-ground motion attenuation equations.

Unfortunately, because of lack of sufficient V_s profiles for volcanic rocks and for Quaternary units, it has not been possible to break down these geologic units into more V_s^{30} categories. Generally, volcanic rocks show extremely variable lithologies. Units such as basalt, (hard rocks but extensively fractured), and pyroclastic rocks (loose agglomerations of volcanic ash and cinders) are widely spread in the Campania-Lucania region.

The Quaternary units, usually have highly variable velocity characteristics. They are subdivided on geologic maps into many formations according to grain size, density, porosity, and cementation. Therefore, special care should be taken when dealing with these ground type soils with typically very low values of V_s , low internal damping and a non-linear behaviour, that can produce anomalous site amplification effects.

Clearly, the site-conditions map for the Campania-Lucania region is expected to evolve as more shear-wave velocity measurements and more geologic data on Quaternary and Volcanic area become available in order to highlight significant variations in site response for mapped young sediments. However, resulting site-conditions map can be used to estimate the shaking over the Campania-Lucania region, by spatially interpolation ground motion recorded using frequency and amplitude dependent site correction factors based on surface geology.

3.

Data selected

3.1. Strong-Motion Data Set

The seismic data used in the present work consist of earthquakes recorded in the Campania-Lucania region (Southern Italy) where, an advanced and dense seismic network, the Irpinia Seismic Network (ISNet) equipped with high dynamic instruments, has been recently installed (Weber et al., 2006). ISNet covers an area of approximately $100 \text{ km} \times 70 \text{ km}$ along the Southern Apennine chain and is deployed around and over the active faults system that generated the November, 23 1980, Irpinia earthquake (M 6.9) (Figure 3.1).

Recordings from 22 of the available seismic stations for 92 earthquakes ($1.5 < M_I < 3.2$) occurred between February 2006 and December 2007, were analyzed. Stations not considered in the analysis were discarded either because they had insufficient data or were not operating during the considered period. The waveforms have been recorded by the accelerometer sensors, Guralp CMG-5T, with a sampling rate of 125 Hz.

In order to assign a geologically-based site classification to each station site, the seismic stations were displayed on the QVTM geologic map (Figure 3.2).

On the basis of the QVTM site conditions map, it can be noted that the recording instruments are located on rock and stiff soil (Mesozoic and Tertiary age), and only one station, MVL3, is located on a volcanic area (Tertiary-Quaternary age).

Since the MVL3 station wasn't operating during the analyzed period, in order to characterize the site response in the volcanic area, 14 seismic events ($1.5 < M_I < 3.2$) have been used. These events occurred between February 2005 and January 2008, were recorded by the VULT seismic station (Trillium 40 seconds seismic sensor) from the Istituto Nazionale di Geofisica e Vulcanologia, (INGV network).

Figure 3.4 displays the distribution of the events and stations used.

Most of the seismic events have source depths between 2.4 and 30 km. The hypocentral distances ranging from 4.5 to 65 km, with 80% of the events within distances of 10 to 65 km.

In order to be valid the far-field approximation (Aki and Richards, 2002), a minimum hypocentral distance about 4 km has been imposed.

Figure 3.5 shows an example of recording on the three components, at one of the analyzed ISNet stations, for the 5 February 2006 earthquake ($M_I 3.2$) occurred at 17:02:49.437 UTC.

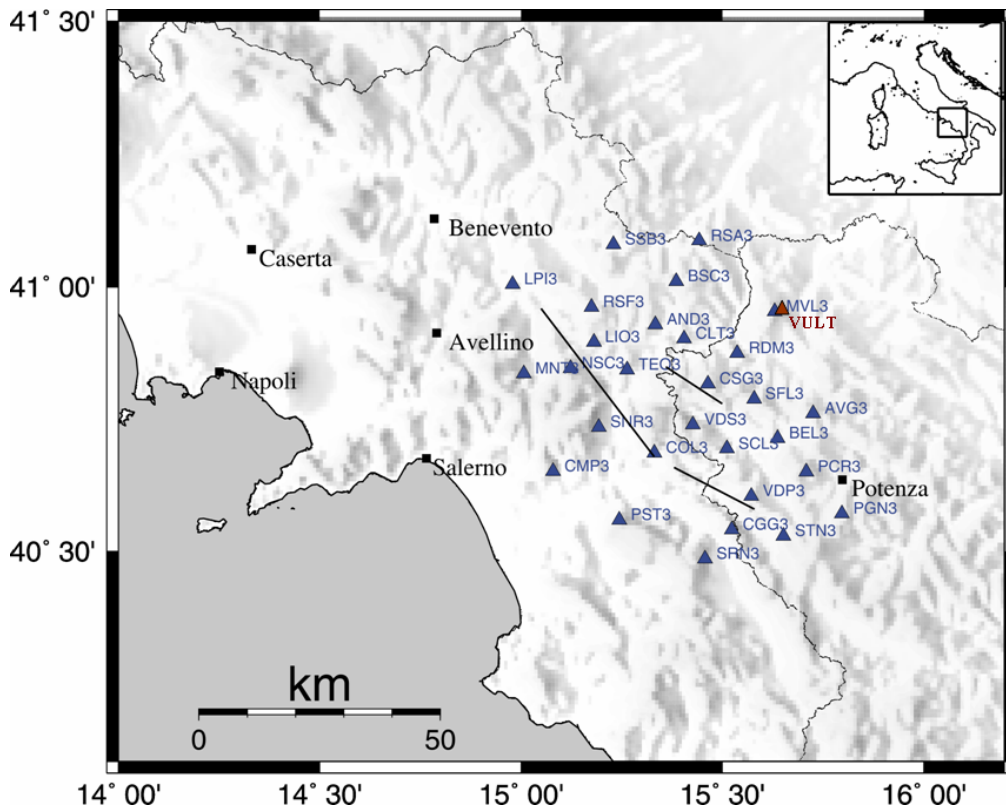


Figure 3.1. The ISNet stations (blue triangles) installed around the Irpinia fault system (black lines). The VULT station belongs to the INGV network (red triangle).

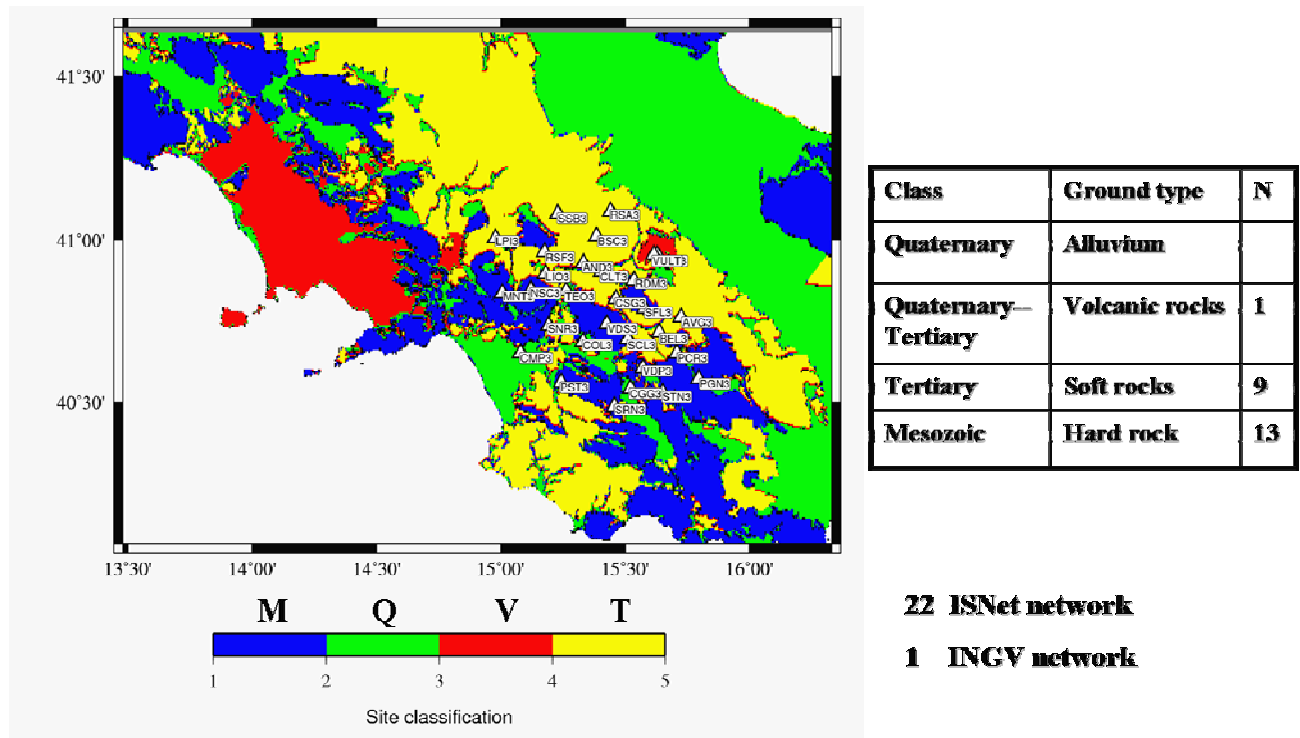


Figure 3.2. The QVTM site-conditions map.

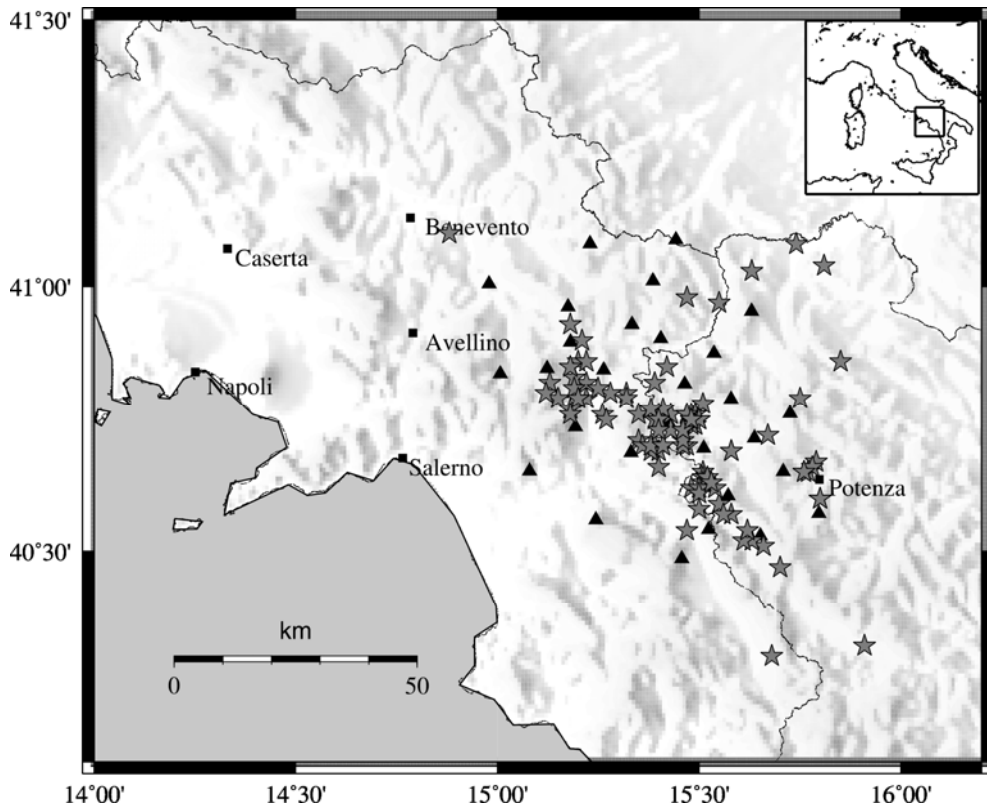


Figure 3.4. Epicenters of the seismic events (stars), and the seismic stations (triangles).

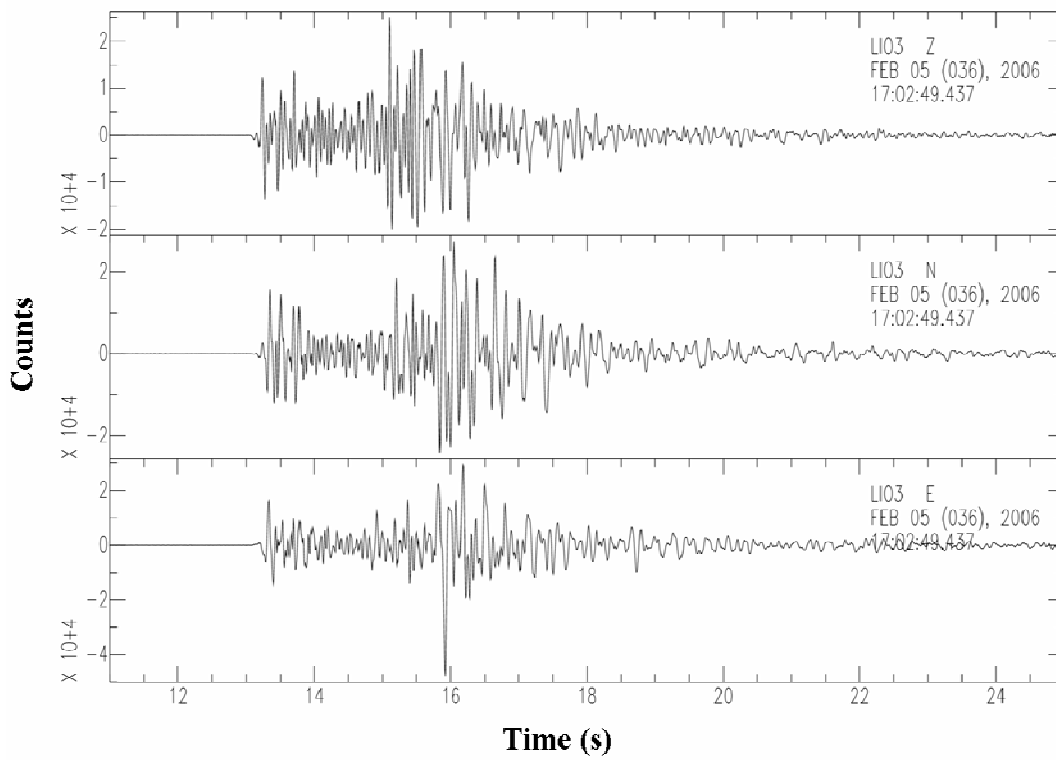


Figure 3.5. Example of recording at the LIO3 station for the 5 February 2006 earthquake (MI 3.2) at 17:02:49.437 UTC.

Figure 3.6 shows the number of events per magnitude range, and the magnitude distribution as a function of hypocentral distance, epicentral distance, and source depths.

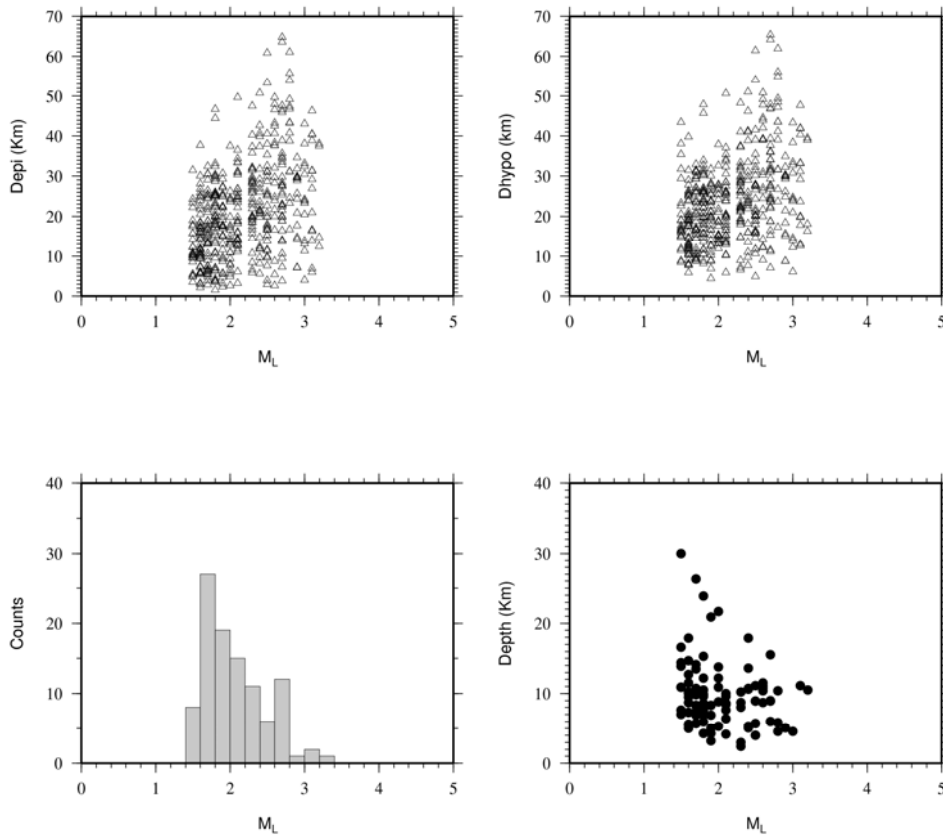


Figure 3.6. Number of events per magnitude range, and the magnitude distribution vs the hypocentral distance, epicentral distance and source depths.

4.

Simulation of peak ground motion parameters using the stochastic simulation technique.

4.1. Introduction

A method for simulating ground motions has been carried out to verify the presence of the amplifications that the site effects induce on the incoming seismic wavefield. The selected method is the stochastic simulation technique proposed by Boore (1983). This method is widely used to simulate the higher-frequency ground motions (generally, $f > 0.1$ Hz), and to predict ground motions for region of the world in which recordings of motion from potentially damaging earthquakes are not available (Boore, 2003).

The stochastic simulation technique proposed by Boore (1983), has its basis in the work of Hanks and McGuire (1981), who combined seismological models of the spectral amplitude of ground motion with the concept that high-frequency motions are essentially random (Hanks and Kanamori, 1979; McGuire and Hanks, 1980; Hanks and McGuire, 1981). The method is referred as stochastic because uses a partially stochastic description of the source and propagation path. Generally, the simulated motions are those corresponding to the S waves, because, due to their effect on the structures, are the most important motions for seismic hazard.

The method has been widely applied, and its effectiveness has been demonstrated and reported in a great number of references (Akinici et al., 2001; Anderson and Lei, 1994; Singh et al., 1999, 2002 and so on).

The fundamental ingredient is the amplitude spectrum of the ground motion at a specific distance and site condition. Assuming that this motion is distributed with random phase over a duration equal to the inverse of the lower corner frequency, the time series can be obtained by a time-domain simulation or by using random vibration theory.

In the present thesis, the stochastic method has been used to simulate ground motions expected for a set of earthquakes having a specified magnitude and fault-station distance using specific values of stress-drop and attenuation terms to account for the of region of interest. The selected ground-motion parameters are peak ground acceleration (PGA) and peak ground velocity (PGV).

In order to identify possible site effects at each of the seismic stations of the ISNet network, for each recorded earthquake, the corresponding PGA and PGV were simulated. At each station those values are compared with those recorded. In the hypothesis of a correct simulation of both source

and propagation effect, using a large dataset, the residuals measured at each station provide a first-order measure of the site effect.

4.1. The basis of stochastic method: general overview

The observed spectrum of the ground motion at a specific site, can be represented in the form of a simple equation (Iwata and Irikura, 1988):

$$O(f) = S(f)P(f)G(f)I(f) \quad (4.1)$$

where $S(f)$ is the seismic source, $P(f)$ is the term of propagation path, $G(f)$ is the site effects, and $I(f)$ is the instrument or the type of motion. When the stochastic method has to be applied, all the spectrum terms in equation (4.1) must be specified.

The most commonly used model of the earthquake source spectrum is the ω -square model, where both the shape and the amplitude of the source spectrum are specified as a function of earthquake size. For a constant stress-drop ($\Delta\sigma$), the dependence of the corner frequency (f_0) on the moment magnitude (M_0) is a constant ($M_0 f_0^3 = \text{constant}$) and determines the scaling of the spectral shapes. Following the model proposed by Brune (1970), the corner frequency is given by:

$$f_0 = 4.9 \times 10^6 \beta_s \left(\frac{\Delta\sigma}{M_0} \right)^{\frac{1}{3}} \quad (4.2)$$

where f_0 is in Hz, β_s is the shear-wave velocity in km/s, $\Delta\sigma$ is bars, and M_0 in dyne-cm. From the equation (4.2) the dependence of the corner frequency on earthquake size, can be observed.

Although the ω -square model is widely used, other models can be used within the stochastic method.

The next component that must be specified is the path effect. In most of the applications, the effects of the path are usually represented by a function that accounts for geometrical spreading, attenuation (combining intrinsic and scattering attenuation), and the general increase of duration with distance due to wave propagation and scattering effect.

The simplified path effect for body waves, is given by the multiplication of the geometrical spreading and Q quality factor. The propagation-path effect, $P(f)$, for the radiation of S-waves from a point source, has the following form:

$$P(f) = Z(R) e^{-\pi R f / Q(f) V_s} \quad (4.3)$$

where $Z(R)$ is the geometrical spreading function, $Q(f)$ is a frequency-dependent quality factor of the form $Q(f) = Q_0 (f/f_0)^n$, V_S is the mean shear-wave velocity, and R is the source-to-site distance. Generally, R is taken as the closest distance to the rupture surface, rather than the hypocentral distance. According to Boore et al. (1997), R is given by:

$$R = \sqrt{D^2 + h^2} \quad (4.4)$$

where D is the closest distance to the vertical projection of the rupture surface onto the ground surface, and h is taken from the empirical results.

Although the Fourier amplitude spectrum of the ground motion does not depend on the duration, in the simulation of ground motion is included the distance-dependent duration. The ground motion duration is expressed as the sum of the source duration, which is related to the inverse of a corner frequency, and a path-dependent duration.

Much effort are devoted into accounting for the modifications of the ground motion due to local site geology. In many cases, such as in the present thesis, the simulations from stochastic method are used for the prediction of motion at a generic site. In this instance, a simplified function can be used to describe the frequency-dependent modifications of seismic spectrum (Boore, 2003).

The simplified function has the following form:

$$G(f) = A(f)D(f) \quad (4.5)$$

where $A(f)$ is the amplification and $D(f)$ is the attenuation.

The Boore stochastic method deals with the site effects (G) as a function of the amplitude of shaking, but it does not account for nonlinear effects.

The amplification can be given by the square root of the impedance ratio (*ratio between density and S-waves velocity of different geologic materials*) between the source and the surface. The form of the amplitude is given by:

$$A(f(z)) = \sqrt{Z_s / \bar{Z}(f)} \quad (4.6)$$

where the impedance near the source (Z_s) is given by:

$$Z_s = \rho_s \beta_s \quad (4.7)$$

and ρ_s e β_s are the density and shear-wave velocity near the source. $\bar{Z}(f)$ is a function of frequency because it is a time-weighted average from the surface to a depth equivalent to a quarter wavelength.

The attenuation, $D(f)$ in equation (4.5), accounts for the path-independent loss of high-frequency in the ground motions. This loss may be due to a source effect, as suggested by Papageorgiou and Aki (1983b), or to site effect, as suggested by several authors (Hanks, 1982), or by a combination of both.

In order to account for the diminution of the high-frequency motions a simple multiplicative filter can be used.

Generally, the filters used are two: the f_{\max} filter (Hanks, 1982; Boore, 1983)

$$D(f) = \left[1 + \left(\frac{f}{f_{\max}} \right)^8 \right]^{-1/2} \quad (4.8)$$

and the k_0 filter (Anderson and Hough, 1984)

$$D(f) = \exp(-\pi k_0 f) \quad (4.9)$$

Finally, the term $I(f)$ of the equation (4.1), accounts for the particular type of the ground motion that has to be simulated. These $I(f)$ filter is given by:

$$I(f) = (2\pi f i)^n \quad (4.10)$$

where $i = \sqrt{-1}$ and $n=0, 1, \text{ or } 2$ for ground displacement, velocity or acceleration, respectively.

4.3. Obtaining ground motions: simulations of time series

For a given spectrum of the motion at a site, ground motions in the time or in the frequency domain, can be estimated by applying a time-domain simulation or using random vibration theory.

In this thesis ground motions are computed by applying the time-domain simulation.

The basis of the time-domain procedure are shown in Figure 4.1 (Boore, 2003). White noise, generally Gaussian, is generated for a duration given by the duration of motion (Fig. 4.1a); the noise is windowed (Fig. 4.1b); this windowed noise is, then, transformed into the frequency domain

(Fig. 4.1c); the spectrum is normalized by the square-root of the mean square amplitude spectrum (Fig. 4.1d); the normalized spectrum is multiplied by the ground motion spectrum $O(f)$ (Fig. 4.1e); the resulting spectrum is transformed back to the time domain (Fig. 4.1f).

In applications, it is most common to simulate the time series of ground acceleration. Various other measures of ground motion, such as peak velocity, peak displacement, Arias intensity, and response spectral amplitudes, can be derived from the simulated ground acceleration.

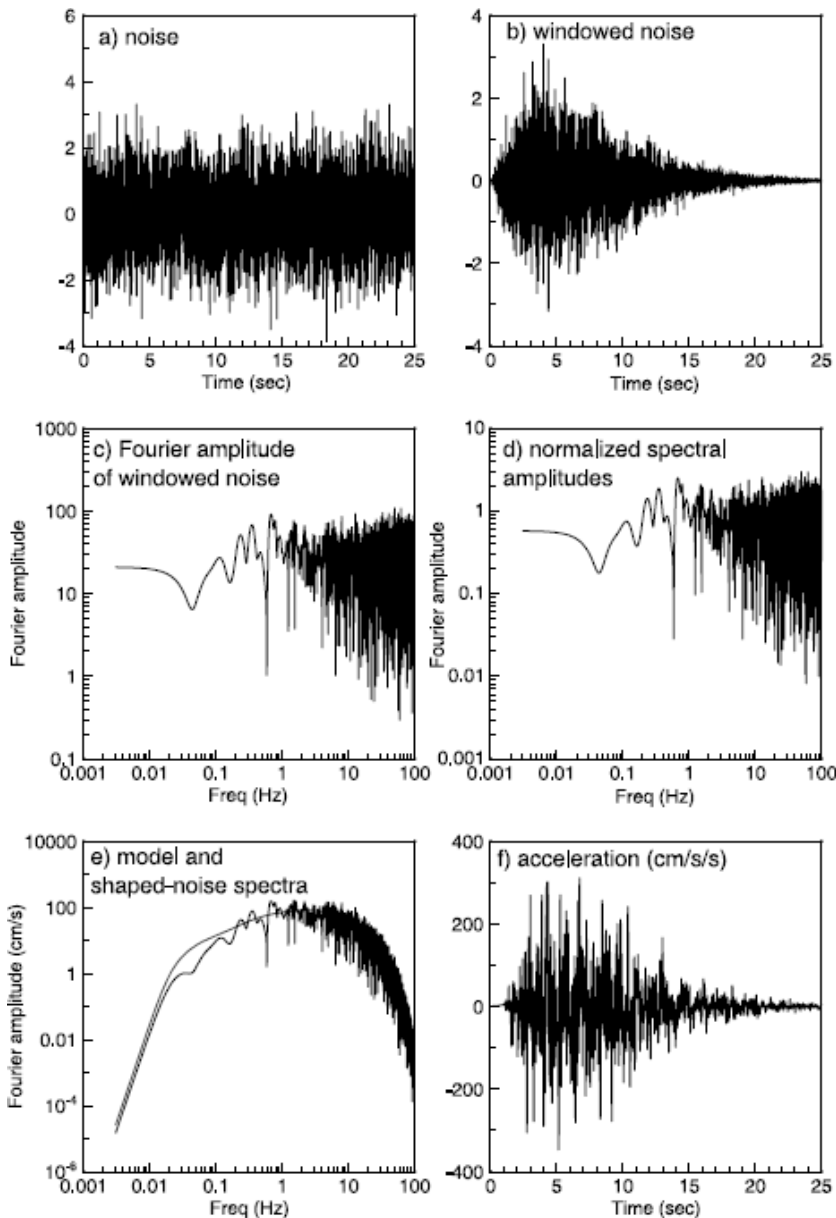


Figure 4.1. Outline of the time-domain approach for simulating ground motions using the stochastic method (Boore, 2003).

4.4. Application

In the present thesis, time-domain simulations were used to identify possible site effects at the seismic stations of the ISNet network, by comparing the observed and simulated peak ground motion parameters at a generic rock or a generic soil site.

The dataset of PGA and PGV used for the study, were collected using the waveforms of 92 local earthquakes ($1.5 < M_l < 3.2$), recorded from February 2006 to December 2007 by 22 seismic stations. Most of the earthquakes have source depths from 2.4 to 30 km, the hypocentral distances ranging from 4.5 to 65 km, with 80% of the events within distances of 10 to 65 km (Figure 3.4).

Thirteen of the 22 stations are located on hard rock (Mesozoic category) and nine on stiff soils (Tertiary category) (Figure 3.2).

At each station the PGA and PGV parameters were obtained from the simulated and recorded acceleration ground motions.

The input parameters for the simulation technique, have been a geometrical spreading of the form R^{-1} , an anelastic attenuation factor parameterized by a frequency dependent quality factor of the form $Q(f) = Q_0 (f/f_0)^n$, and an average static stress-drop of 30 bars. In particular, the quality factor $Q(f)$ is given by:

$$Q(f) = 130 \left(\frac{f}{f_0} \right)^{0.10} \quad (4.11)$$

where $f_0 = 1.0$ Hz (Malagnini et al., 2000).

At each station, the observed peak ground-motion PGA and PGV were compared with the simulated ones.

If the difference between observed and estimated PGA, and PGV values differs from zero, the discrepancy can be attributed to site effects and not to path effects or source effects such as radiation pattern or directivity effects.

Considering the j th receiver, the peak motion residual terms, PGA and PGV, are computed as:

$$\text{Res}(P_j) = \log \text{PGX}_j^{\text{obs}} - \log \text{PGX}_j^{\text{est}} \quad (4.12)$$

where Pgx^{obs} is the recorded value and Pgx^{est} is the estimated value.

In our instance, the residual values between observed PGA and PGV and estimated PGA and PGV, are all different from zero.

In addition, predicted PGA and PGV values were obtained by using pre-existing empirical

attenuation relationships (Wald et al., 1999) that, for given magnitude and distance values, allow to estimate ground motion parameters both in time and in frequency domain. The coefficients of the attenuation model were retrieved from the earthquake recordings by using time-domain simulations. The general formulation of the attenuation relationships is approximated as:

$$\log P_{gx} \approx f(M, R) + g(\phi) \quad (4.13)$$

where P_{gx} corresponds to both PGA in m/s^2 and PGV in m/s , $f(M, R)$ is the standard distance-magnitude dependent function and $g(\phi)$ is a term which accounts for azimuthal dependence of peak ground motion. The attenuation relationship was used to obtain estimate PGA and PGV values at the network recording sites. At each seismic station the residuals were computed by comparing the observed and the predicted ground motion values.

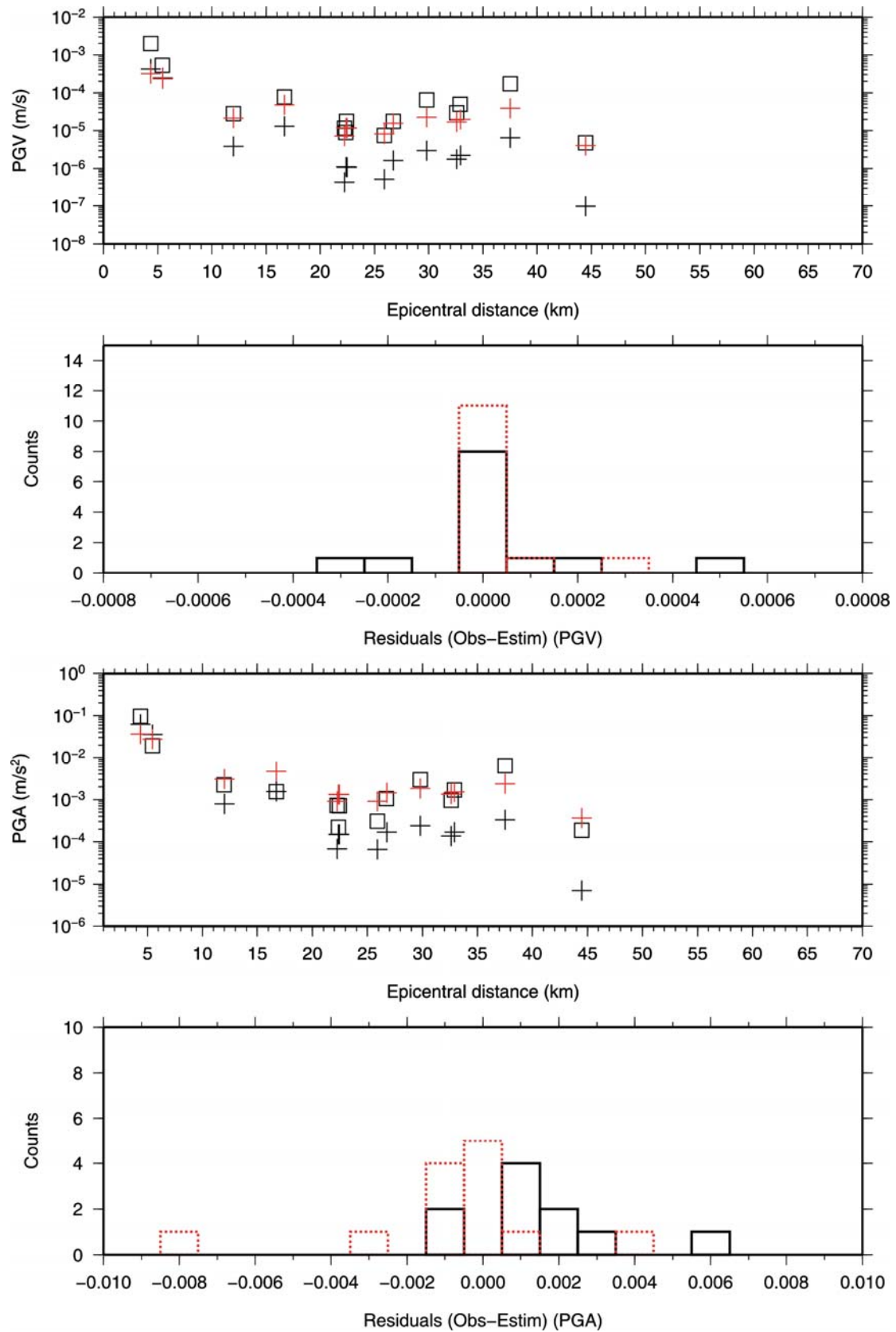
In our instance, the residual values between observed PGA and PGV and estimated PGA and PGV, obtained by using the attenuation relationship, are all different from zero.

This important result suggests that the material properties near the surface in the Campania-Lucania region, can produce large modifications of the selected parameters. In particular, it can be noted that also the surface-rock sites have a site response of their own. This could lead to an underestimation of the seismic hazard when these sites are used as reference sites in the spectral techniques. In fact, the near-surface weathering and cracking of the hard rock sites affects the recorded ground motions at frequencies of engineering interest, even at sites that appear to be located on competent rock (Steidl et al., 1996).

The Figures that follow, one for every station, show the results of the test in terms of residuals between observed and estimated data, these last ones with or without the attenuation relationship. In particular, in the figures there are two bar charts that represent the distribution of the residuals between observed and estimated PGA and PGV values, and two graphs to represent the PGA and PGV distributions as a function of epicentral distance.

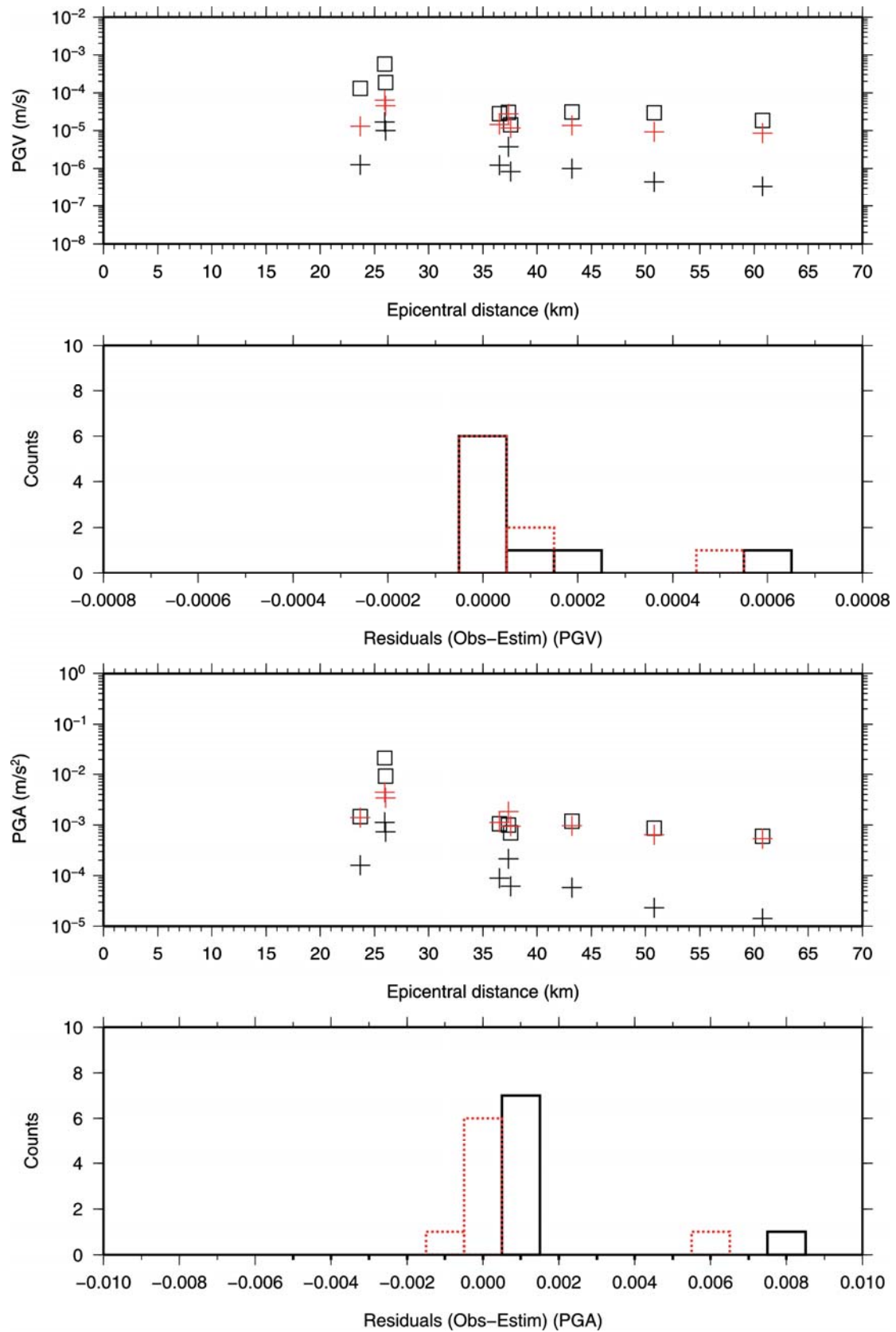
The squares on the graphs represent the observed PGA and PGV values, the black crosses represent the estimated PGA and PGV values obtained without the attenuation relationship, while the red crosses represent the estimated PGA and PGV values obtained when the attenuation relationship is used.

The first thirteen Figures show the residual values for the stations belonging to the Mesozoic site class, the following nine Figures show the residual values for 9 stations belonging to the Tertiary site class.



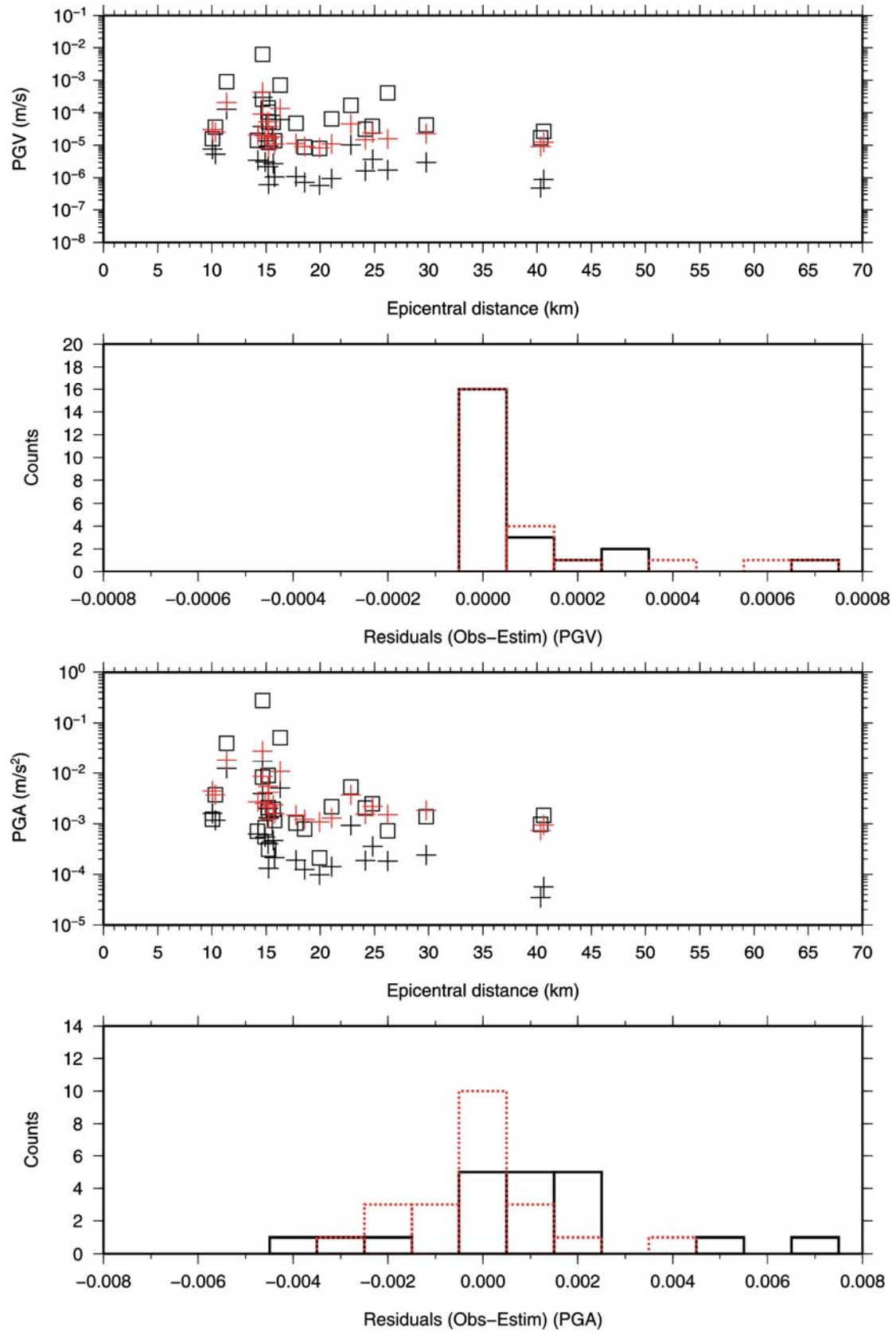
CGG3 seismic station – Mesozoic site class.

Figure 4.1 a). Distribution of the residuals between observed and estimated PGA and PGV values, and PGA and PGV distributions vs the epicentral distance. The squares represent the observed PGA and PGV values, the black crosses represent the estimated PGA and PGV values obtained without the attenuation relationship, while the red crosses represent the estimated PGA and PGV values obtained when the attenuation relationship is used.



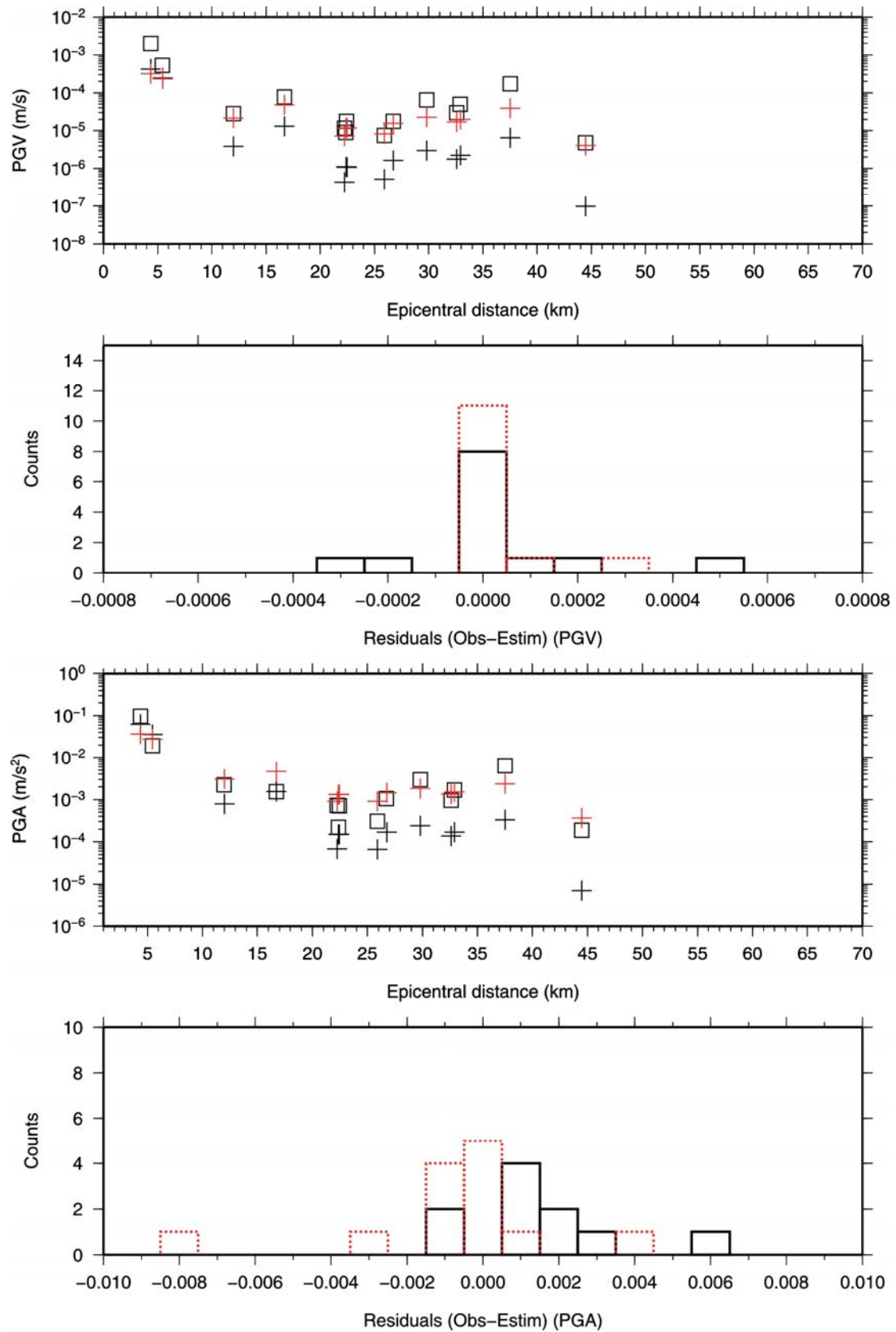
CMP3 seismic station – Mesozoic site class.

Figure 4.1 b). Same as figure 4.1a), but for station CMP3.



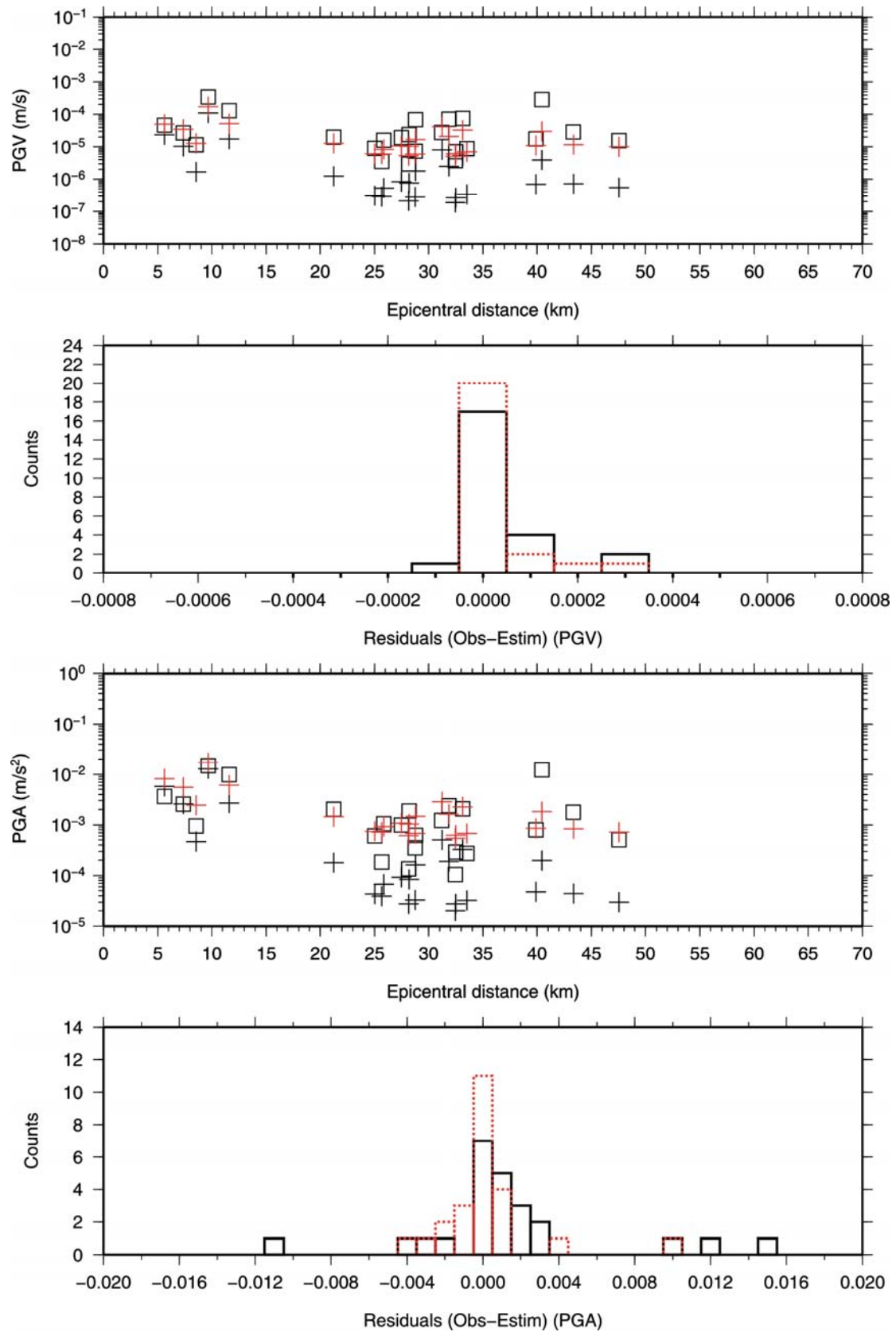
COL3 seismic station – Mesozoic site class.

Figure 4.1 c). Same as figure 4.1a), but for station COL3.



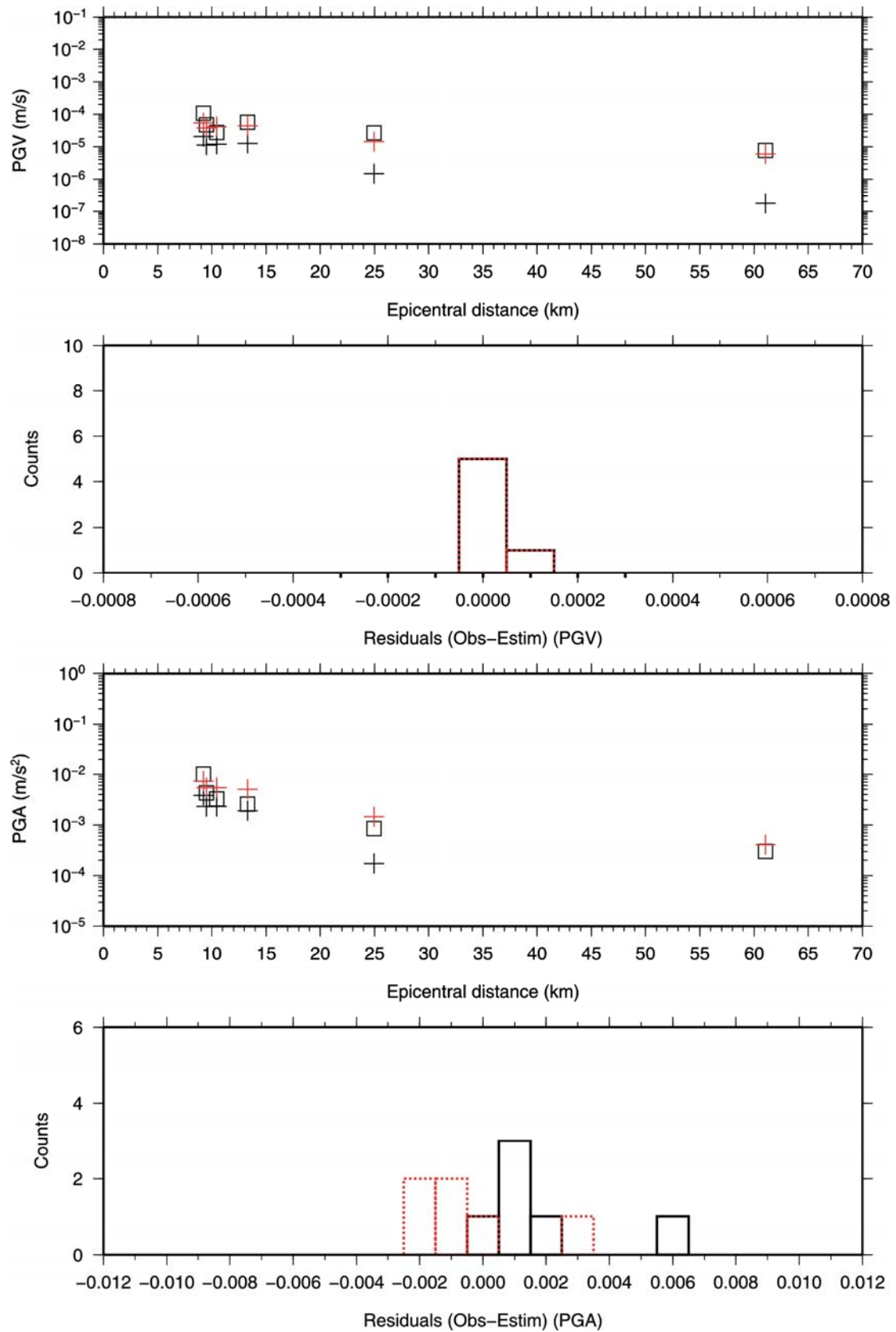
CSG3 seismic station – Mesozoic site class.

Figure 4.1 d). Same as figure 4.1a), but for station CSG3.



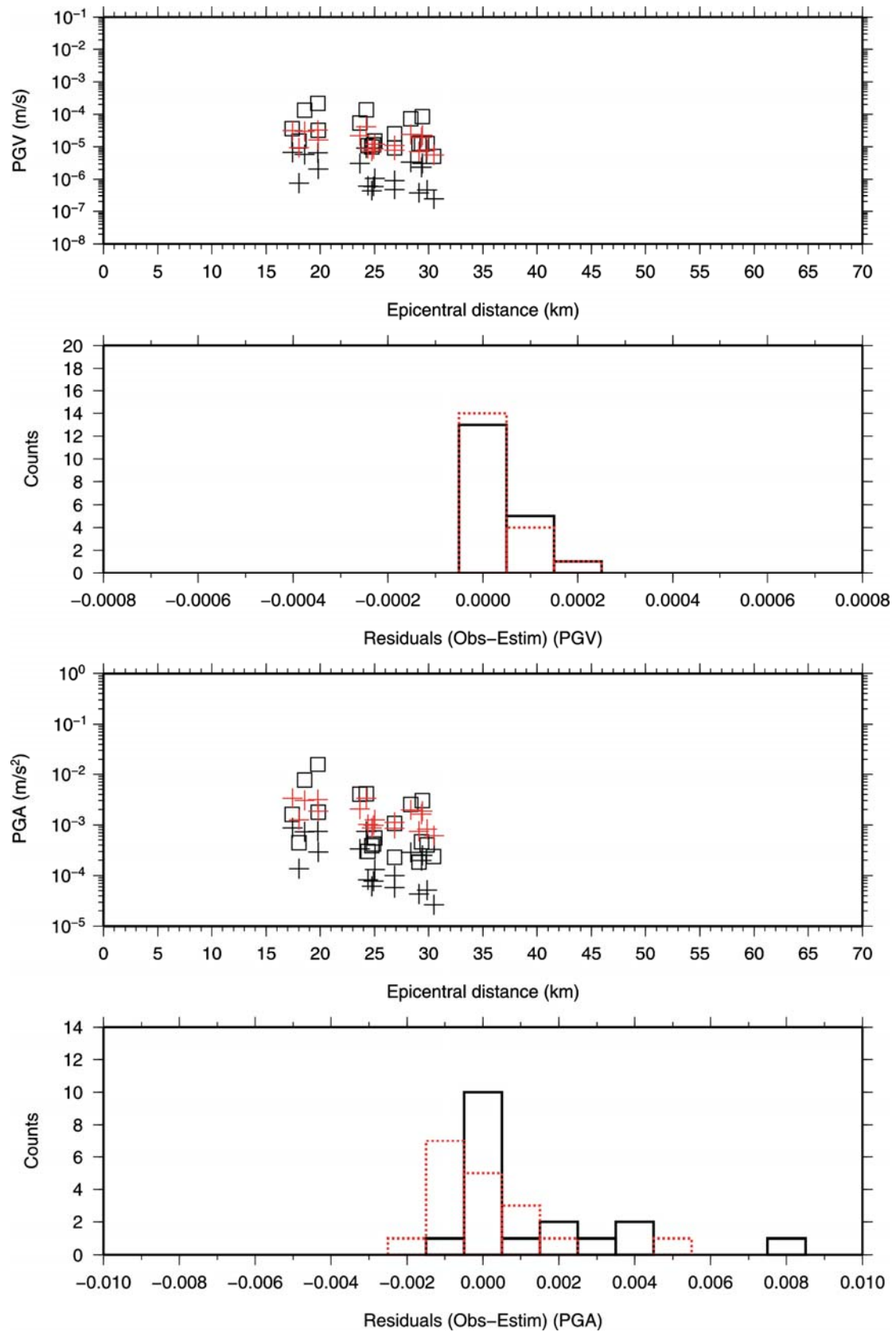
NSC3 seismic station – Mesozoic site class.

Figure 4.1 e). Same as figure 4.1a), but for station NSC3.



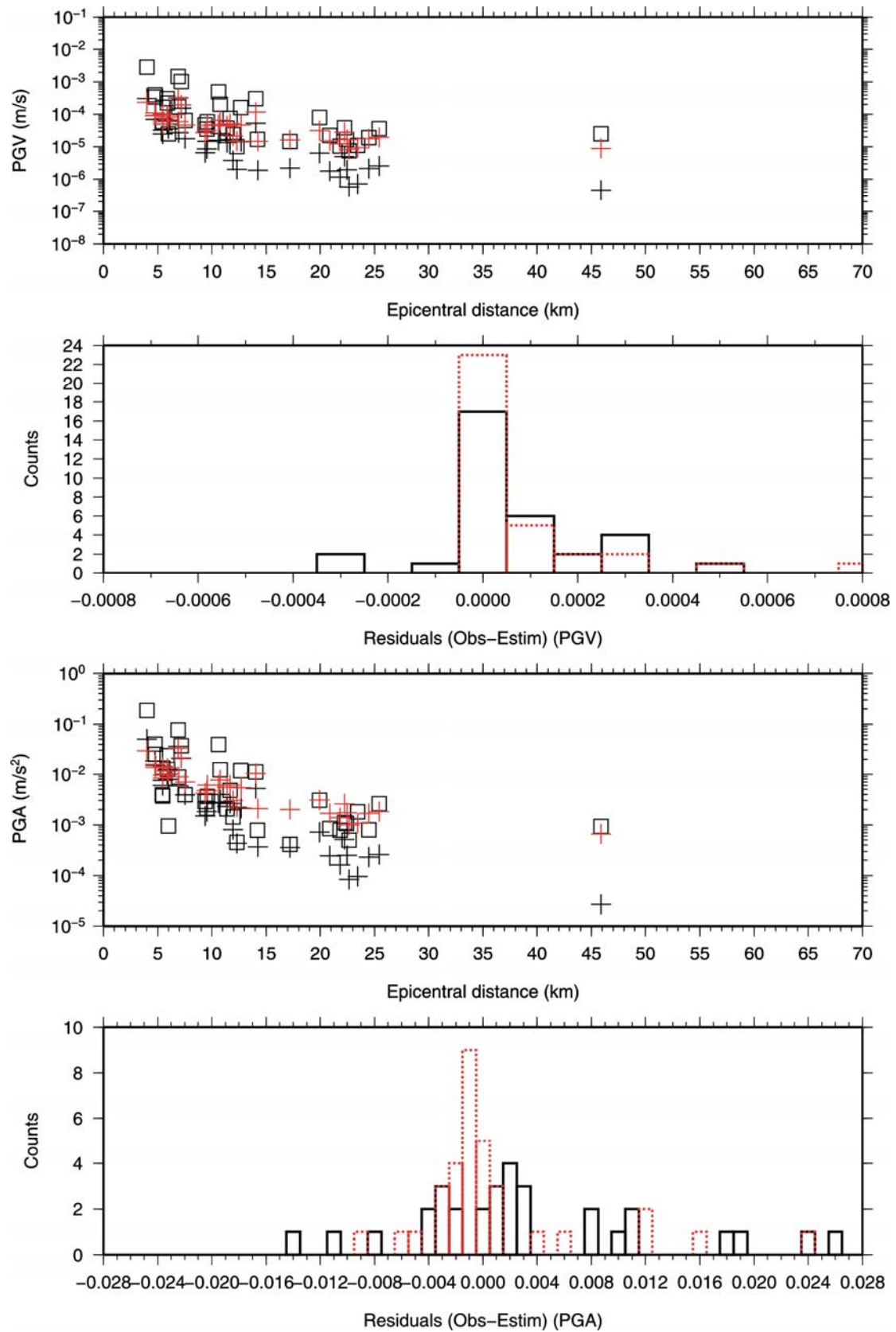
PGN3 seismic station – Mesozoic site class.

Figure 4.1 f). Same as figure 4.1a), but for station PGN3.



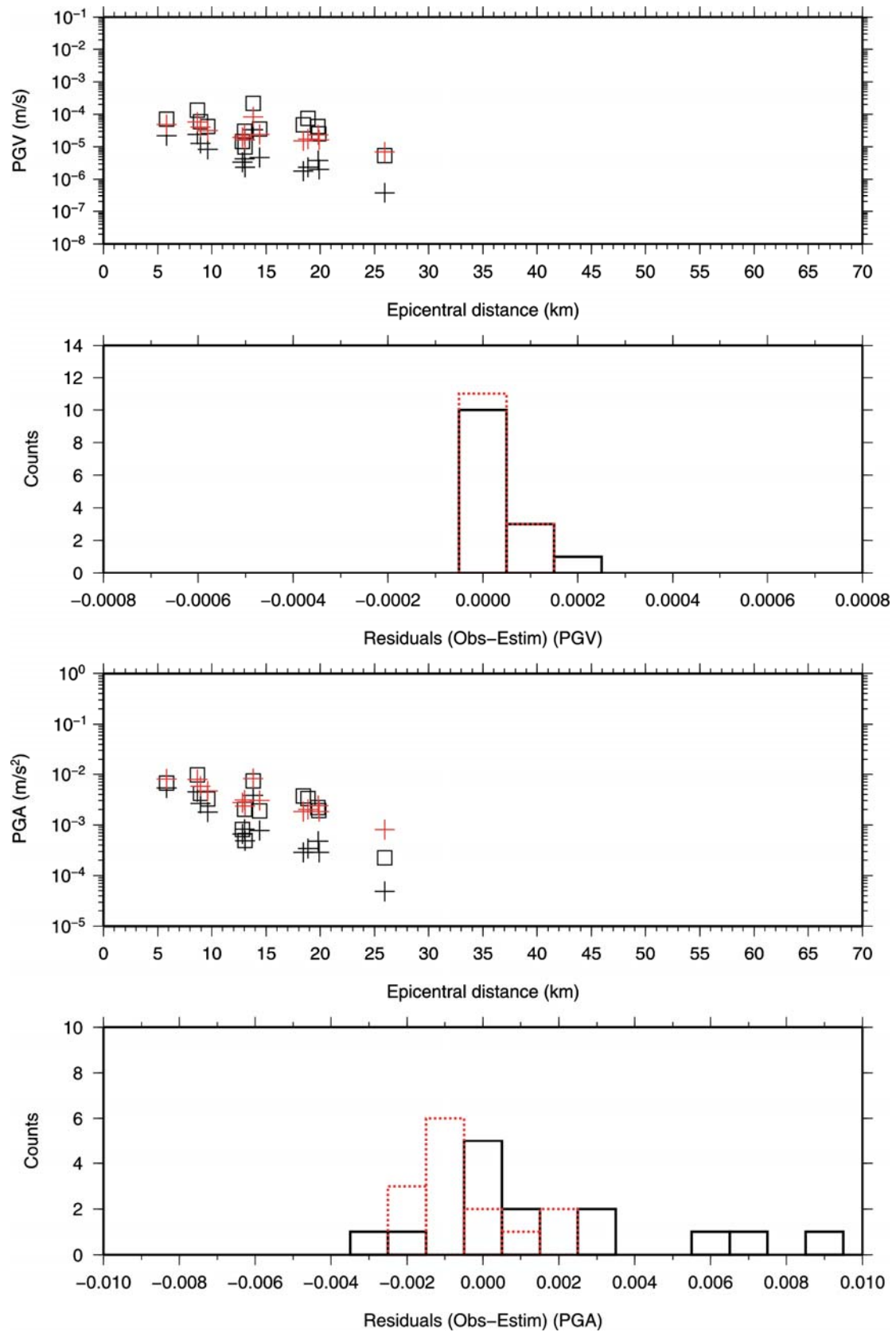
PST3 seismic station – Mesozoic site class.

Figure 4.1 g). Same as figure 4.1a), but for station PST3.



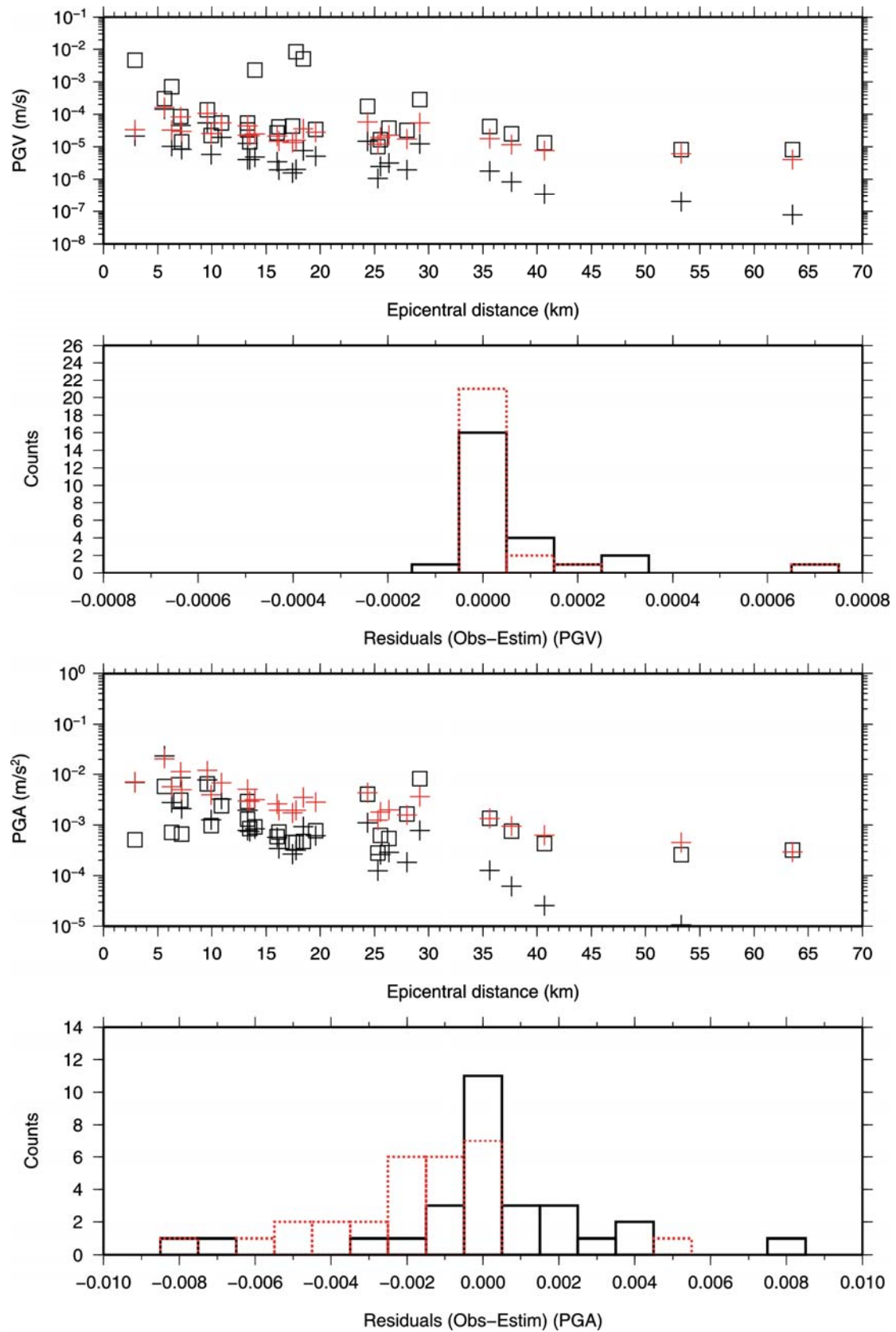
SCL3 seismic station – Mesozoic site class.

Figure 4.1 h). Same as figure 4.1a), but for station SCL3.



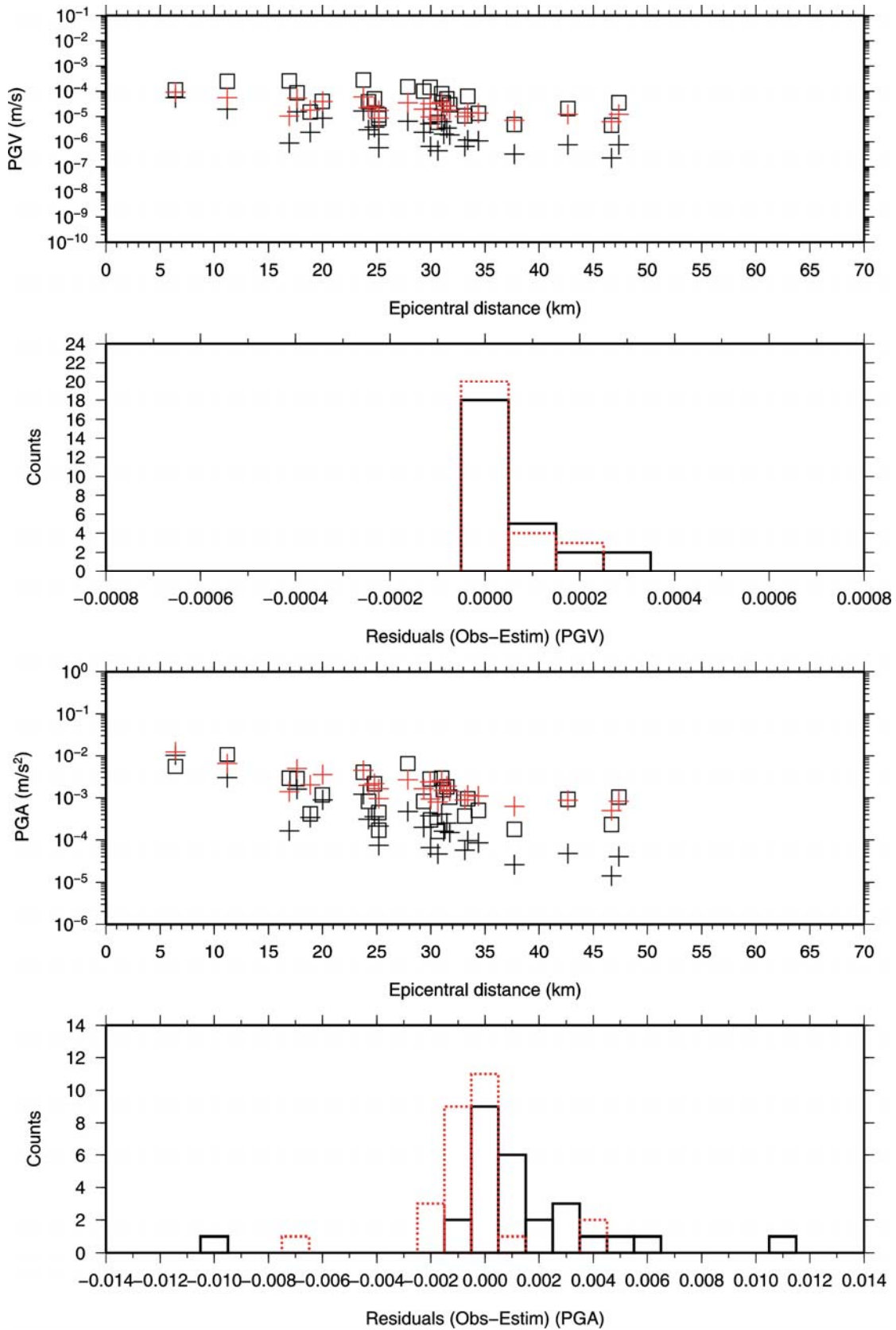
SFL3 seismic station – Mesozoic site class.

Figure 4.1 i). Same as figure 4.1a), but for station SFL3.



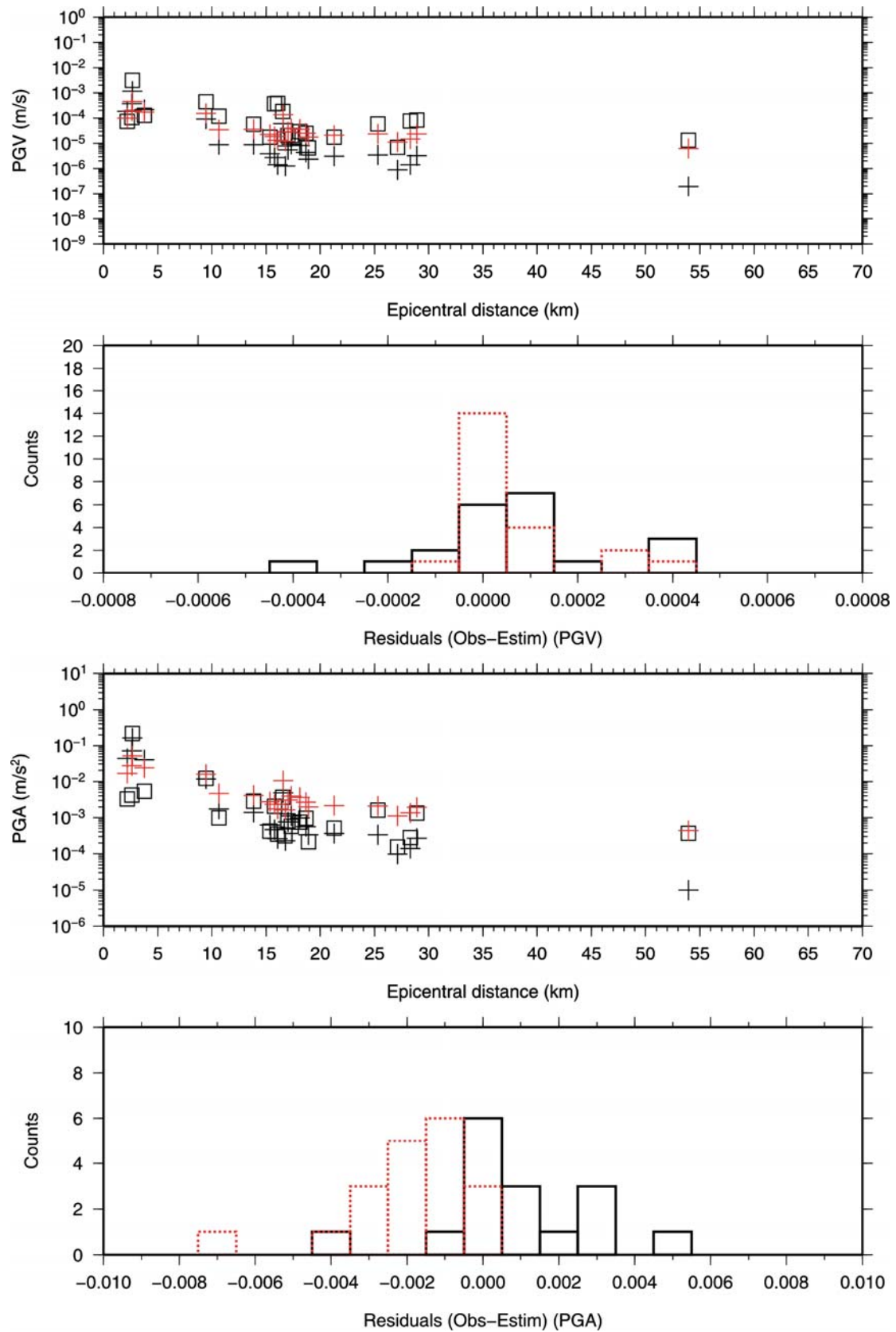
SNR3 seismic station – Mesozoic site class.

Figure 4.1 j). Same as figure 4.1a), but for station SNR3.



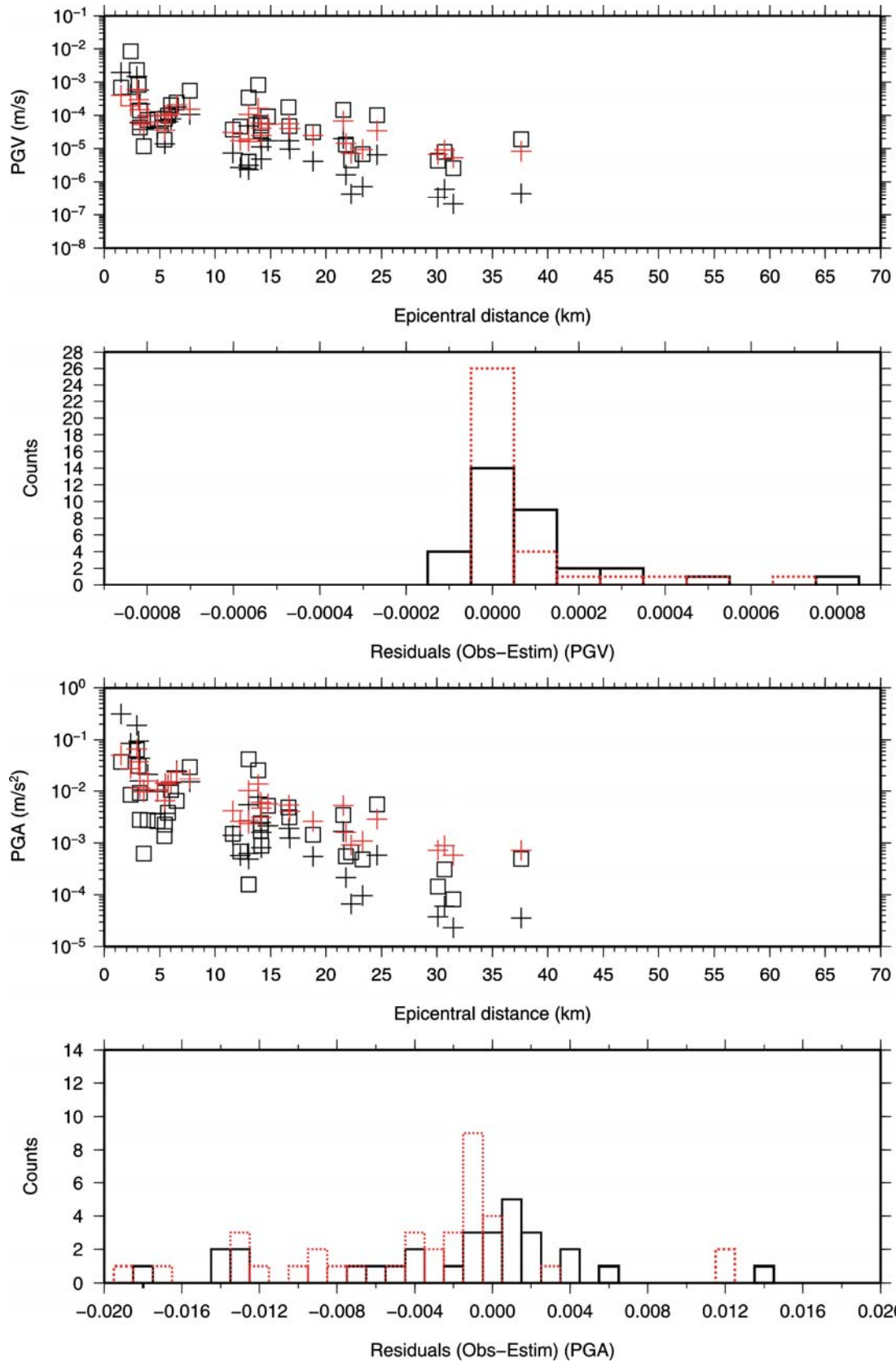
SRN3 seismic station – Mesozoic site class.

Figure 4.1 k). Same as figure 4.1a), but for station SRN3.



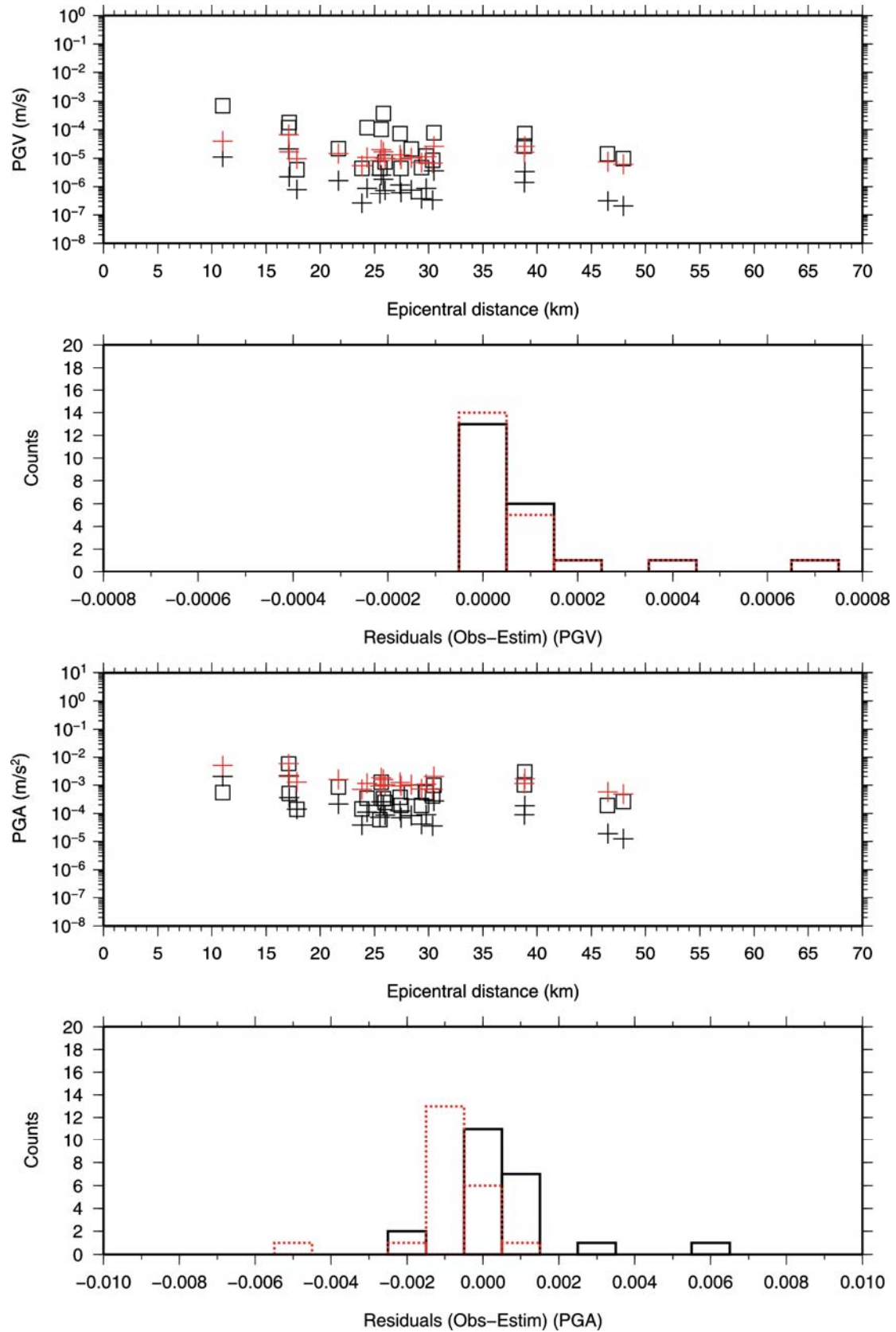
STN3 seismic station – Mesozoic site class.

Figure 4.1 l). Same as figure 4.1a), but for station STN3.



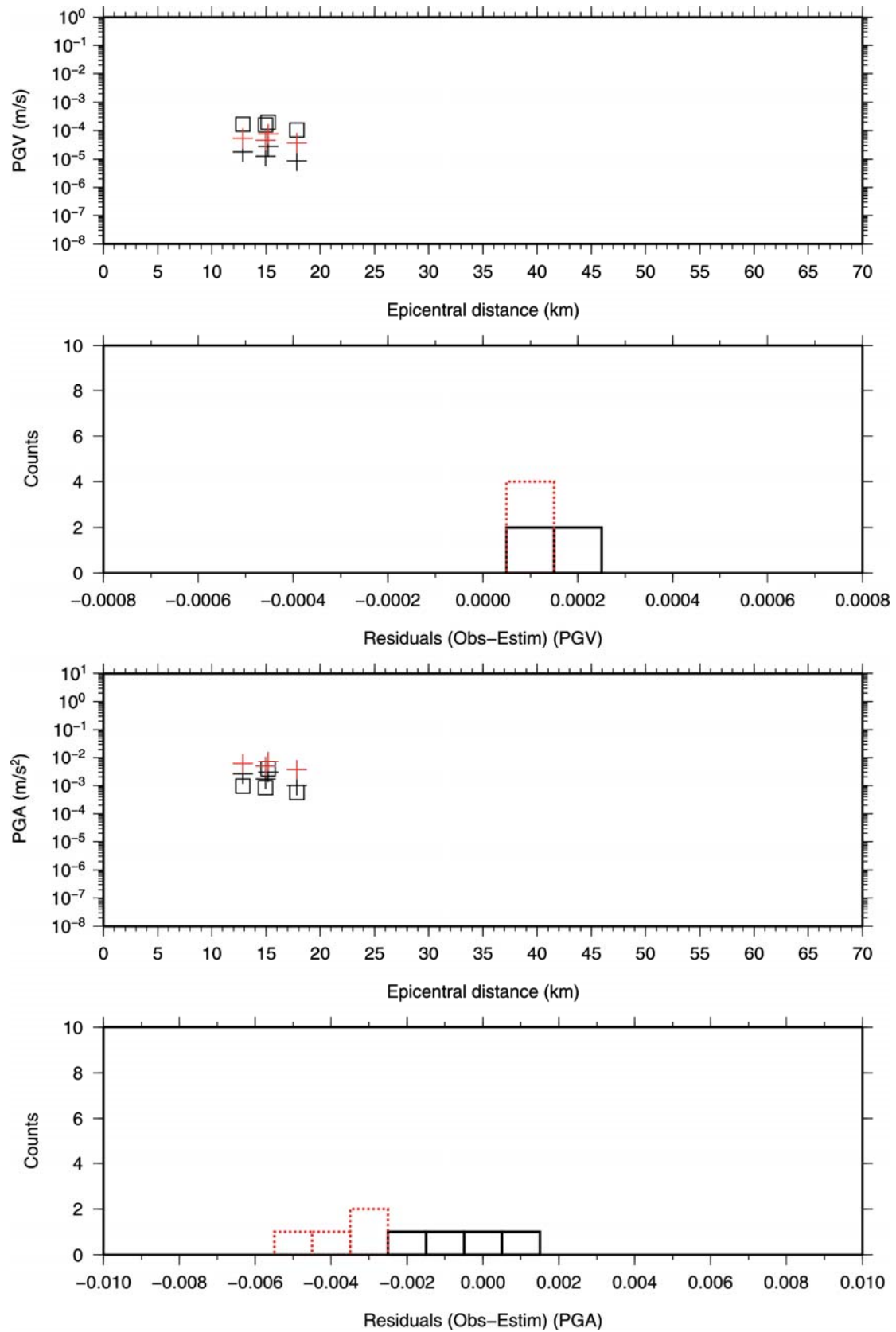
VDS3 seismic station – Mesozoic site class.

Figure 4.1 m). Same as figure 4.1a), but for station VDS3.



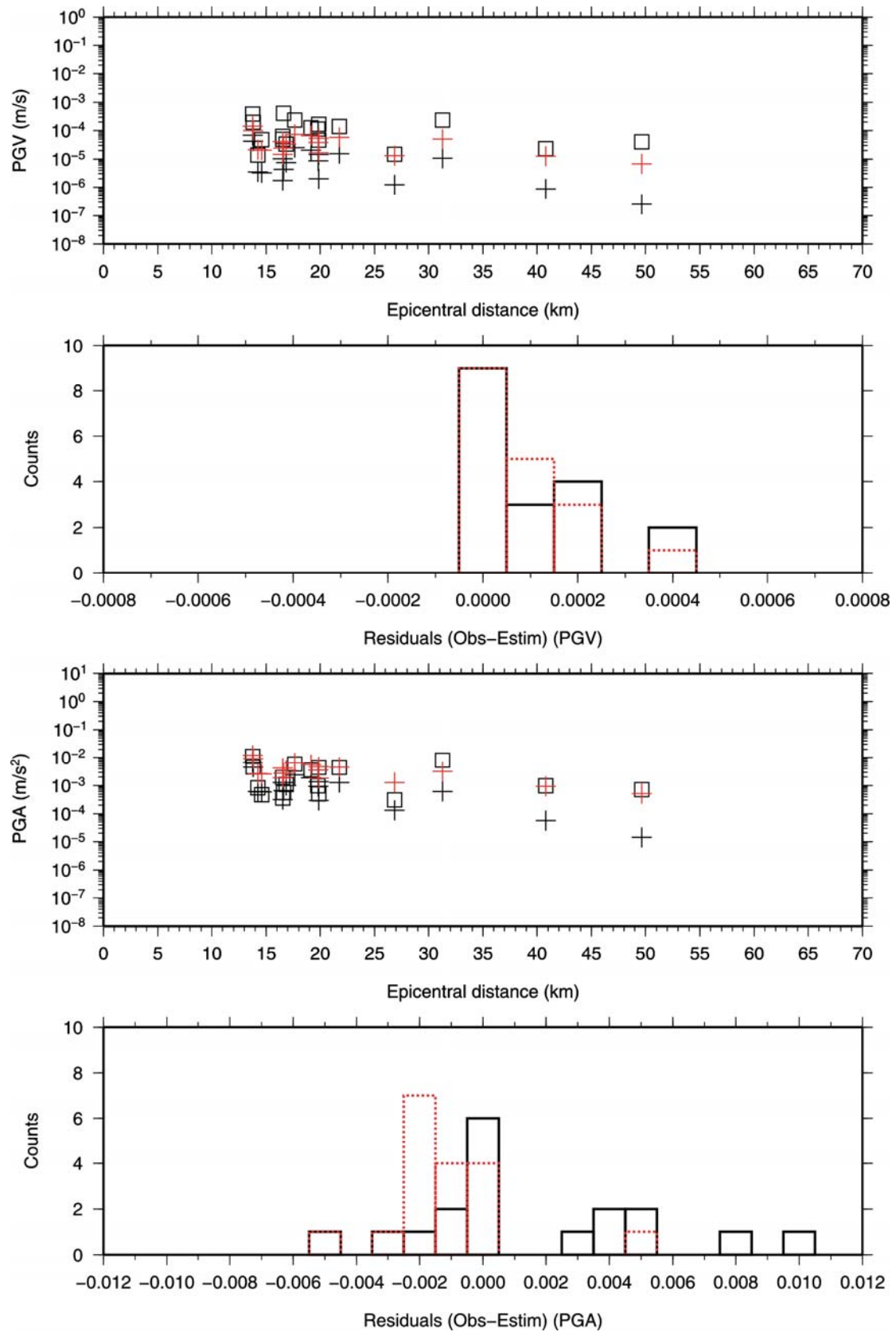
AND3 seismic station – Tertiary site class.

Figure 4.1 n). Same as figure 4.1a), but for station AND3.



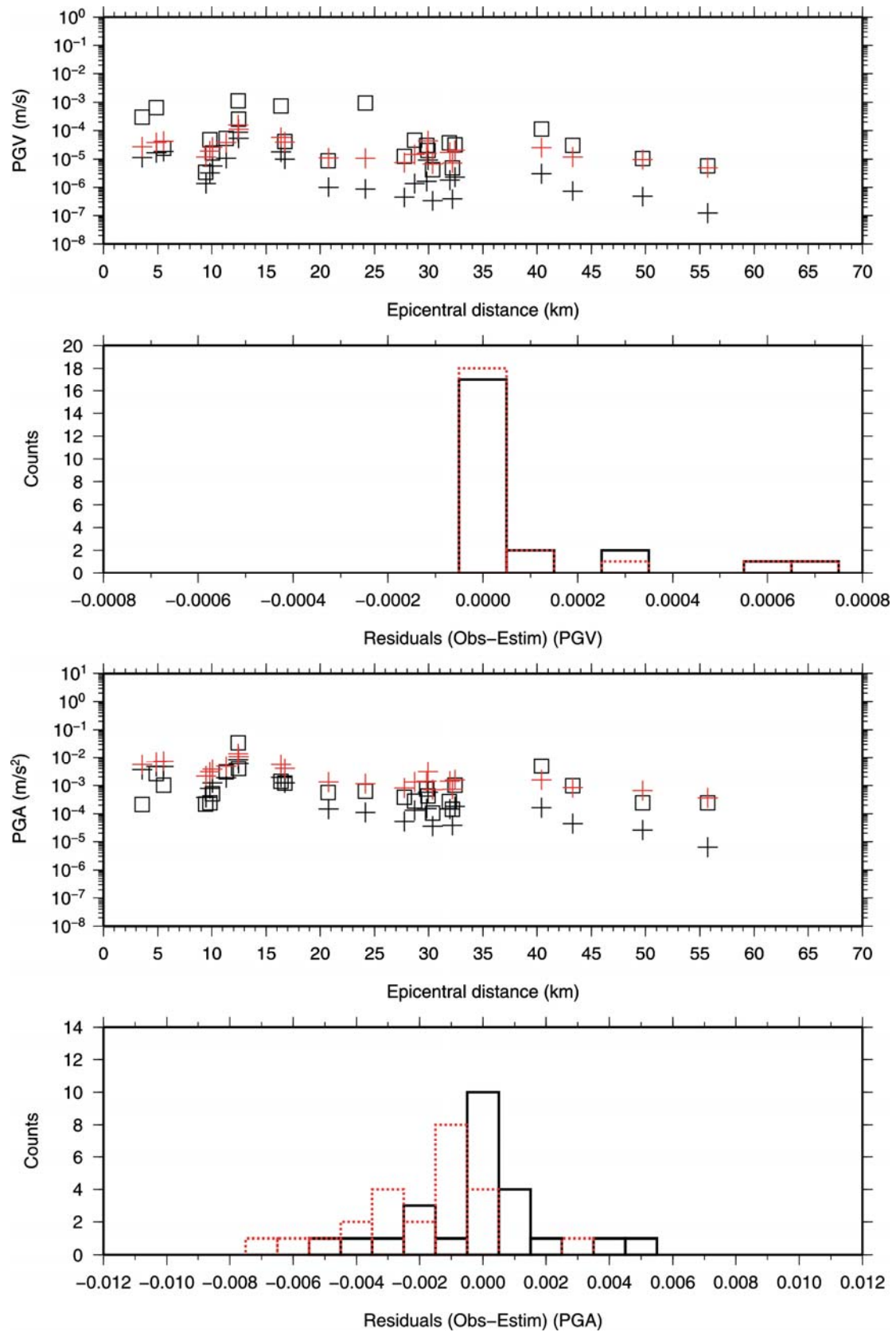
BEL3 seismic station – Tertiary site class.

Figure 4.1 o). Same as figure 4.1a), but for station BEL3.



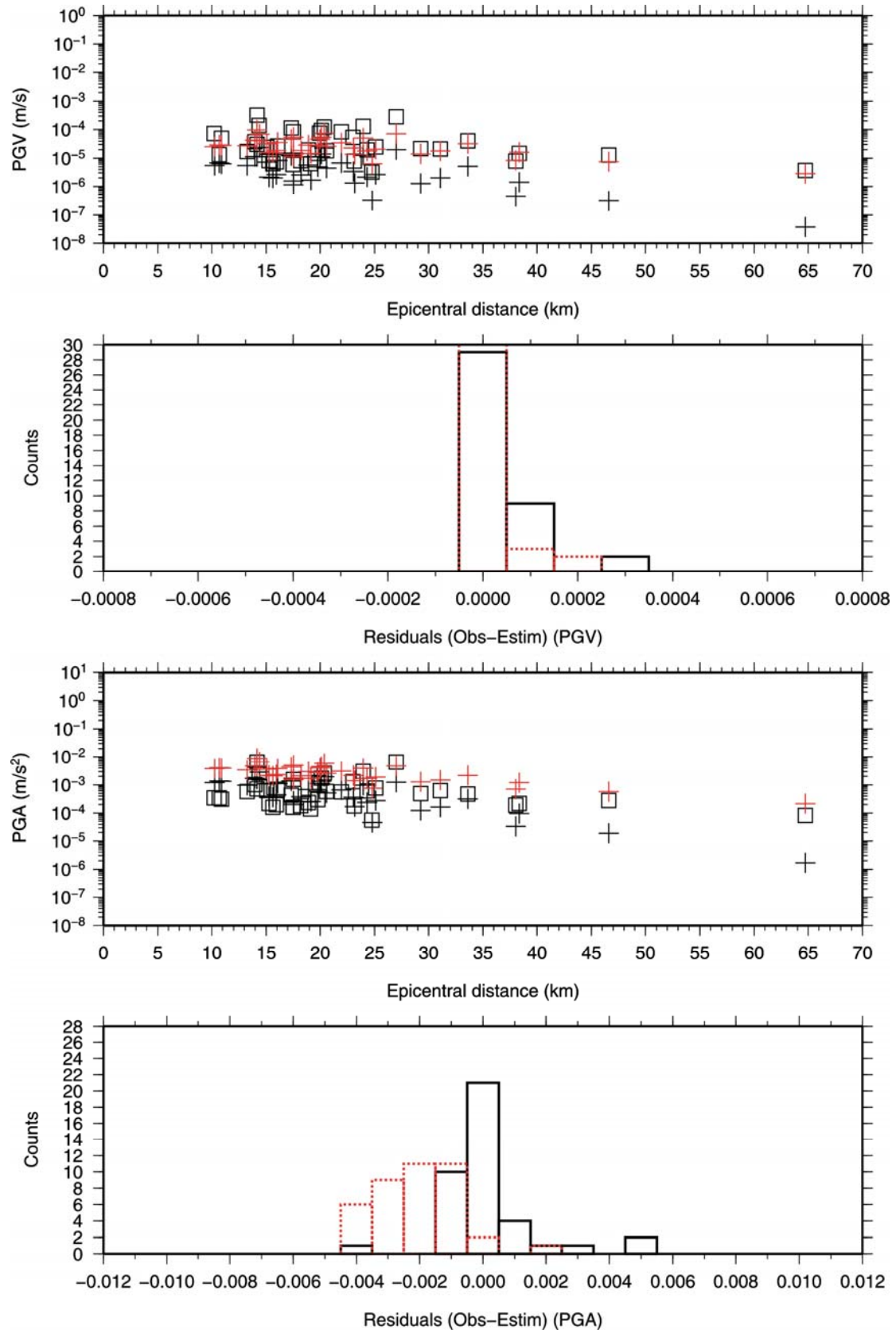
CLT3 seismic station – Tertiary site class.

Figure 4.1 p). Same as figure 4.1a), but for station CLT3.



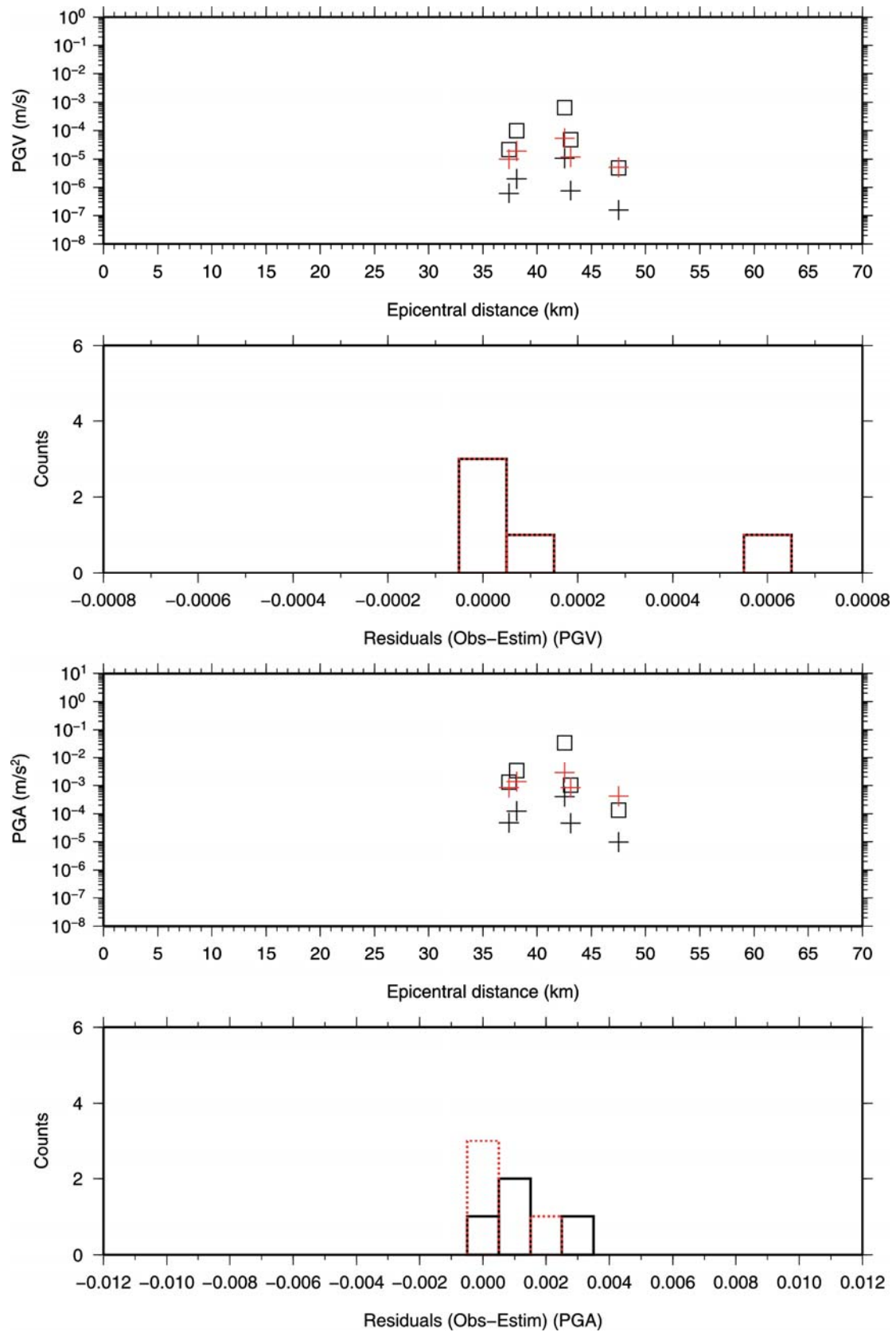
LIO3 seismic station – Tertiary site class.

Figure 4.1 q). Same as figure 4.1a), but for station LIO3.



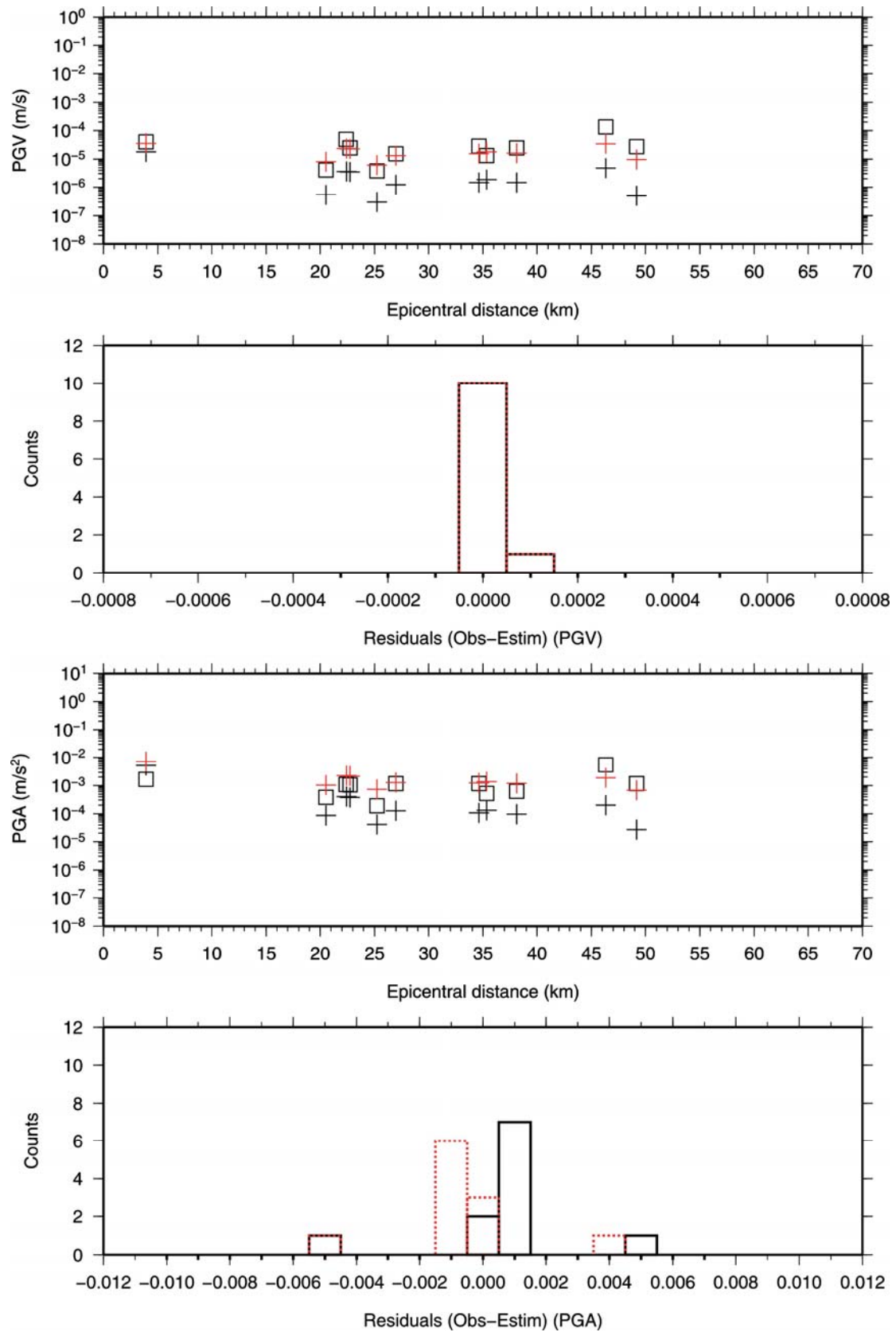
RDM3 seismic station – Tertiary site class.

Figure 4.1 r). Same as figure 4.1a), but for station RDM3.



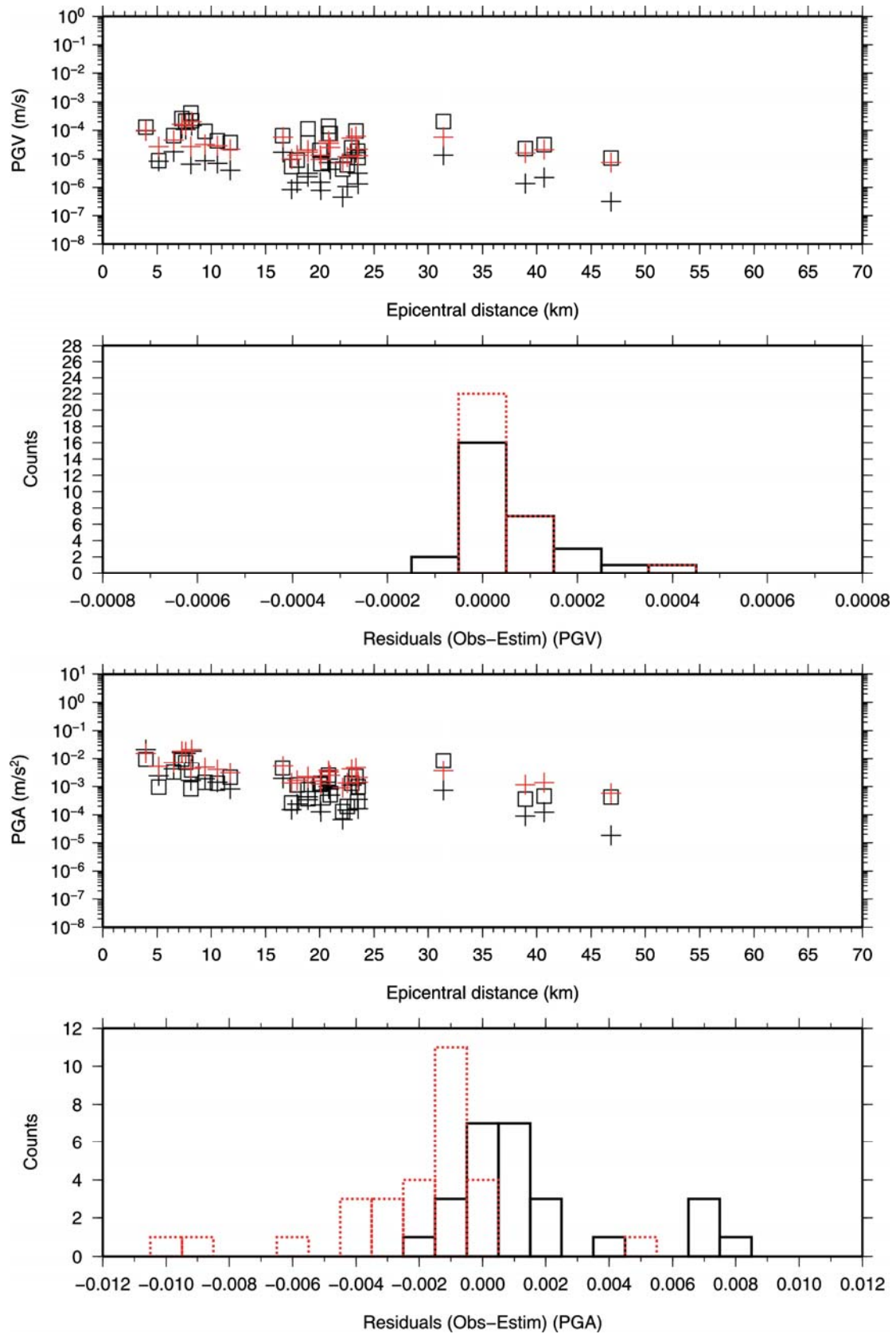
RSA3 seismic station – Tertiary site class.

Figure 4.1 s). Same as figure 4.1a), but for station RSA3.



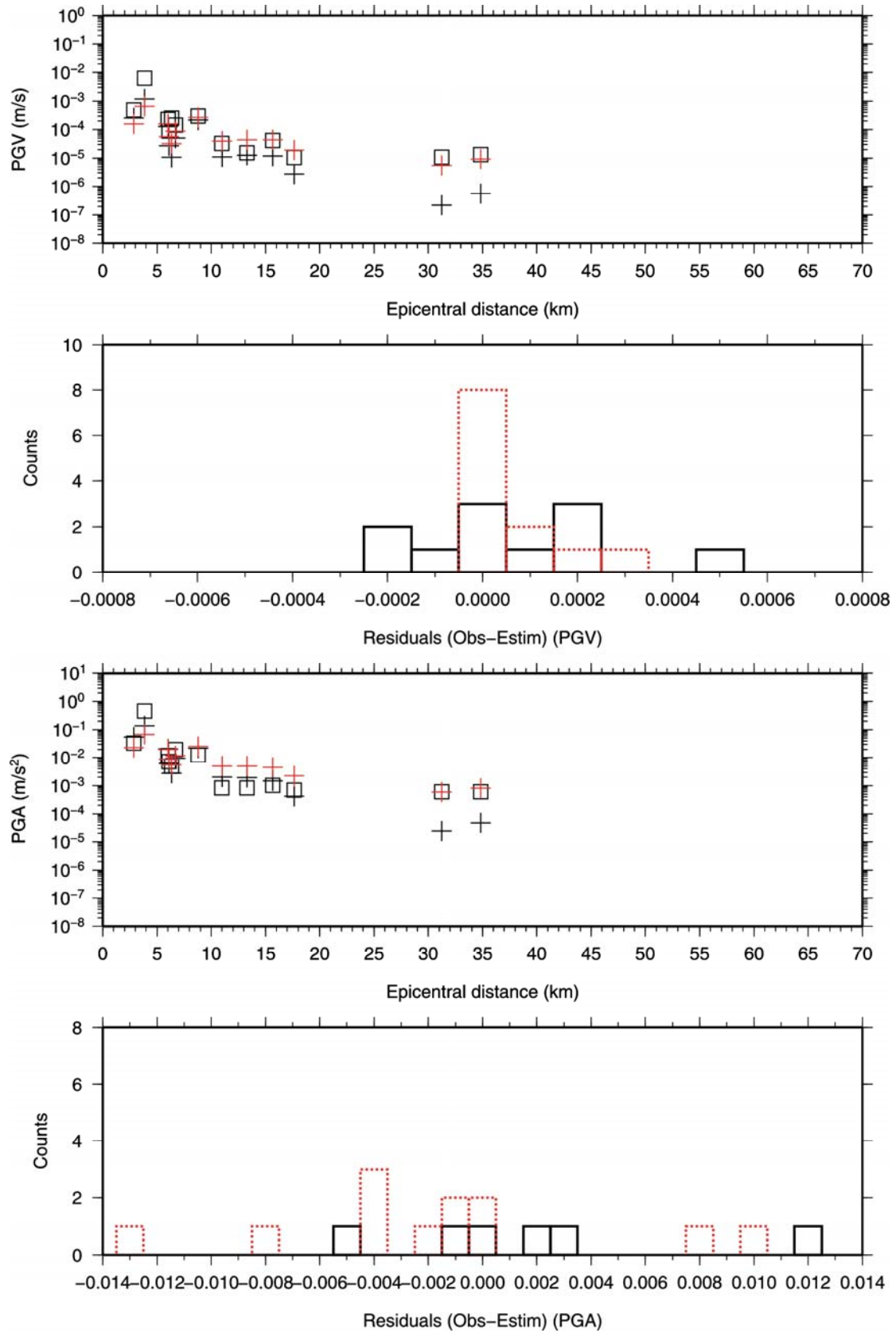
RSF3 seismic station – Tertiary site class.

Figure 4.1 t). Same as figure 4.1a), but for station RSF3.



TEO3 seismic station – Tertiary site class.

Figure 4.1 u). Same as figure 4.1a), but for station TEO3.



VDP3 seismic station – Tertiary site class.

Figure 4.1 v). Same as figure 4.1a), but for station VDP3.

5.

Estimation of site amplification in the Campania-Lucania region (Southern Italy), by non-linear inversion of microearthquake spectra

5.1. Introduction

In regions giving rise to small and moderate-sized earthquakes, as is the case of the Campania-Lucania region (Southern Italy), attenuation relationships for a specific site class, are crucial parameters in seismic hazard analyses. One way to improve the predicting of ground shaking over a region from future earthquakes, is to reduce the uncertainty in the attenuation relationships by regionalizing them to a specific area. Site conditions can have profound effects on the ground surface motion at soil sites, and inappropriate modeling of these, can produce large uncertainties into attenuation models. In order to include the site response into regional hazard mapping, several methods that use the local recordings of strong-motion data, have been developed.

The methods proposed can be divided into two main categories, depending on whether or not they need a reference site.

One of the most used techniques to estimate site effects in regions of moderate to high seismicity, is the spectral ratio method that uses earthquake recordings relative to a reference station (Borcherdt, 1970). The procedure consists in comparing records at nearby sites, using one of them as the reference site, generally consisting a station installed on firm hard rock. The spectral ratios represent a reliable estimate of the site response, if the reference site is located sufficiently near to the examined site to ensure that the differences between sites can be ascribed to site conditions, and not to a source or propagation effects. However, as underlined by several authors (Field and Jacob 1995, Boatwright et al., 1991, Harmsen, 1997a), identifying and separating source and site effects, is the greatest impediment to the spectral analysis of low and moderate magnitude earthquakes.

Andrews (1986) recast the method of spectral ratios into a generalized-inverse problem by inverting the body wave spectra of recorded events, for all source, site, and propagation effects simultaneously. In a nutshell, the amplitude spectrum of the i th earthquake recorded at the j th receiver, $O(f)_{ij}$, can be represented in the frequency domain as the product of three physical parameters (Iwata and Irikura, 1988):

$$O(f)_{ij} = S(f)_i P(f)_{ij} G(f)_j \quad (5.1)$$

where $S(f)_i$ is the seismic source effect of the i th earthquake, $P(f)_{ij}$ is the term accounting for the propagation path from the j th receiver, and $G(f)_j$ is the site effect at the j th receiver.

The model can be linearized by taking natural logarithms:

$$\ln O(f)_{ij} = \ln S(f)_i + \ln P(f)_{ij} + \ln G(f) \quad (5.2)$$

This linear equation often forms the basis of attempts to separate the source, path, and site effects. For each frequency of interest, the terms $S(f)_i$ and $G(f)_j$ are estimated from all the events recorded by each station, through the sum of squared differences between observed and theoretical spectra. To constrain the inversion, generally $G(f)_j$ is specified for the records at one site, called *reference site*. The reference site is taken equal to 1 at each frequency. Since the site amplification at a reference site is set to unity, this method provides results comparable with those obtained by the traditional spectral ratios.

This technique depend on the availability of an adequate reference site.

Since such a site may not always be available, it is desirable to develop alternative methods that do not rely on a reference site.

An alternative method employs the generalized-inversion technique suggested by Boatwright et al. (1991), where shear-wave spectra are represented with a parameterized source, path-effect model and site-response term for each site. The source parameters for each event, the path-effect terms and the site response for each site are inverted simultaneously, in the least-squares sense. This inversion scheme allows to recover the shape of the site response spectra from seismic data by assuming the general shape of the source spectra, the ω^{-2} source model, and inverting for the seismic moment and corner frequency of each earthquake.

The site responses in the Campania-Lucania region have been determined using a non-linear inverse procedure based on the Simplex algorithm. The method has been applied to 22 seismic stations providing accelerograms from 92 local earthquakes and to one station providing seismograms from 14 local earthquakes.

S -wave displacement spectra have been computed by using a Fourier transform of 5 second time windows enclosing the manually picked S -phase on acceleration waveforms. The inversion starts assuming a ω^{-2} source model (Brune, 1970), a geometric attenuation of the form R^{-1} , and a frequency-dependent quality factor of the form $Q(f) = Q_0 (f/f_0)^n$. The site effects have been estimated following the method introduced by Tsurugi et al. (1997). The method selects values for the flat levels and the corner frequencies obtained at the end of the inversion, and produces different

source models for each earthquake. Then, the specified source model divides the corresponding corrected amplitude spectrum of every event. This gives the site effect (Moya et al., 2000). Assuming that the site effects are the same regardless of the seismic event, the average and the normalized standard deviation are finally calculated. The main advantage of this technique is that it does not need a reference site.

At each station, the resulting site-amplification spectra are averaged over three frequency bands: the first-frequency band (Ib) ranging from 1 to 5 Hz, the second (IIb) ranging from 5 to 10 Hz, and the third ranging from 10 to 15 Hz (IIIb). These bands are chosen to retrieve the amplification factors for different input ground-motion parameters (PGM), such as PGA, PGV or Sa(T), that are "moderate-to-high" frequency parameters.

In order to correlate the average site amplifications with the superficial geology, three maps were constructed displaying site amplification factors on the QVTM site conditions map. The maps are aimed at identifying the main geological units in outcrop at which a constant amplification coefficient or a site-response function, can be associated. These correlations are fundamental to include an average site effects in real or near-real time shake maps. This work has been carried out in the frame of European Safer Project also (Seismic Early warning for Europe – FP6-Global-4).

Significant correlations with the surface geology have been found, suggesting that the site spectral amplification is also influenced by the nature of near-surface materials. Average site-amplification factors are, also, compared with those obtained from many California earthquakes by Harmsen (1997) and Borchardt (1994), and are found to be in good agreement in amplitude values.

5.2. Inverse theory

Inverse theory is an organized set of mathematical techniques used to infer the values of model parameters from given observed data. It is a task that often arises in many branches of the physical sciences, and is, also, widely used by people working with geophysical problems, since they always have a set of measurements that depend on a set of model parameters (for instance the knowledge of Earth's interior from data collected at the Earth's surface only).

Let \mathbf{S} be a generic physical system (for example the mass of the Earth, or gravity, or a quantum particle, etc.) described by a set of model parameters. If the parameters describing the model are not directly measurable, it is possible to extract their values from observable parameters that characterize the physical system. While the forward problem can predict the results of measurements on the basis of some general principle or model, the inverse problem, starting with measured data and a general principle or model, determines estimates of the model parameters.

Therefore, while the forward problem has a unique solution, the inverse problem has multiple solutions (Tarantola, 2005). Because of that, in the inverse problem all the a priori information on the model parameters must be explicated (Menke, 1989).

As an example, consider the phenomenon of temperature variation as a function of depth beneath the Earth's surface. Assuming that the temperature increases linearly with depth z , with a law such as $T(z) = az + b$, where a and b are constants. By knowing these constants it is possible to find the temperature variation (forward problem) by simply computing the formula for a given depth. The inverse problem, instead, determines a and b on the basis of temperature measurements made at different depths.

The forward and inverse problem can be formulated as follows:

Forward problem:

model parameters \rightarrow model \rightarrow prediction of data

Inverse problem:

measured data \rightarrow model \rightarrow estimates of model parameters.

In most inverse problems the observed data over-determines some model parameters, leaving others underdetermined. This under-determination, due to intrinsic experimental uncertainties or lack of data, can be easily handled applying present-day methods based on the concept of “least-absolute-values” and on the “minimax” criterion, introduced by Laplace in 1799 to obtain the “best” solution, or based on the “least-squares” criterion, formulated by Legendre in 1801 and Gauss in 1809.

Moreover, data redundancy typically makes inverse problems “ill-posed” as opposed to the “well-posed problems” defined by Hadamard. Of the three conditions for a “well-posed problem” (existence, uniqueness, stability of the solution or solutions), the stability condition is the most often violated one. For instance, to a small perturbation of the data typically corresponds a large perturbation of the solution. In this case, the inverse problem is typically “ill-conditioned” and can be regularized using a probabilistic formulation, where the information on the model parameters is given by a probability distribution in the ‘model space.’ Then, the measurements of the observable data, the *a priori* information on model parameters, and the information on the physical correlations between observable parameters and model parameters can all be described using probability

densities.

The techniques used today for solving inverse problems are as diverse as the problems themselves, but they can all be described by the same few principles.

Formulating the inverse problem starts with a description of the measured data, usually, represented by a vector. If N is the number of measurements, they are arranged in a vector \mathbf{d} of dimension N .

The model parameters can be represented as the elements of a vector \mathbf{m} of dimension M .

data:

$$\mathbf{d} = [d_1, d_2, d_3, \dots, d_N]^T$$

model parameters:

$$\mathbf{m} = [m_1, m_2, m_3, \dots, m_M]^T \quad (5.3)$$

In the inverse theory, the model parameters and the data are correlated, and their relationship is called *model*. In realistic situations the relationship between data and model parameters is expressed by complex equations, though in general they can be expressed by one or more equations of the form:

$$\begin{aligned} \mathbf{f}_1 &= (\mathbf{d}, \mathbf{m}) = 0 \\ \mathbf{f}_2 &= (\mathbf{d}, \mathbf{m}) = 0 \\ &\cdot \\ &\cdot \\ &\cdot \\ \mathbf{f}_L &= (\mathbf{d}, \mathbf{m}) = 0 \end{aligned} \quad (5.4)$$

where L index is the number of equations. These equations are solved, or “inverted” for the model parameters and, generally, $\mathbf{f}(\mathbf{d}, \mathbf{m}) = 0$ can consist of nonlinear functions of the data of model parameters.

The function \mathbf{f} has an implicit linear form in the data and model parameters that can be written as the matrix equation:

$$\mathbf{f}(\mathbf{d}, \mathbf{m}) = 0 = \mathbf{F} \begin{bmatrix} \mathbf{d} \\ \mathbf{m} \end{bmatrix} \quad (5.5)$$

where \mathbf{F} is an $L \times (M + N)$ matrix.

In many instances it is possible to separate data and model parameters, thus forming exactly N equations that are linear in data, but can be nonlinear in the model parameters:

$$\mathbf{f}(\mathbf{d}, \mathbf{m}) = 0 = \mathbf{d} - \mathbf{g}(\mathbf{m}) \quad (5.6)$$

When the function \mathbf{g} is linear, it is possible to obtain an $N \times M$ matrix equation:

$$\mathbf{f}(\mathbf{d}, \mathbf{m}) = 0 = \mathbf{d} - \mathbf{Gm} \quad (5.7)$$

In that case, the inverse problem can be solved by inverting the matrix \mathbf{G} :

(5.8)

$$\mathbf{m} = \mathbf{G}^{-1}\mathbf{d}$$

5.3. Simplex method

The general approach for solving nonlinear inverse problems is the same used when dealing with problems in which one seeks to minimize or maximize a function, by systematically choosing the values of real or integer variables out of a given dataset. This is an optimization problem that can be described in the following way:

Given: a function $f: A \rightarrow \mathbb{R}$ from a set A to real numbers

Sought: an element x_0 in A such that $f(x_0) \leq f(x)$ for every x in A ("minimization")

or such that

$f(x_0) \geq f(x)$ for every x in A ("maximization").

The function f is called *objective function*, or *cost function*. A possible solution that minimizes (or maximizes) the objective function is called an *optimal solution*. Generally, when the objective function does not present convexity, there may be several local minima and maxima. A large number of algorithms proposed for solving non-convex problems are not capable of making a distinction between local optimal solutions and global optimal solutions. Actually, deterministic algorithms have been developed, assuring the convergence to the actual optimal solution of a non-convex problem in finite time. These deterministic algorithms are called *global optimization*.

In the present thesis, a method for local optimization has been used, named **Downhill Simplex Method**, due to Nelder & Mead (1965). This method is a numerical method for optimizing many unconstrained problems, and belongs to the more general class of search algorithms. A simplex is a geometrical Figure consisting of $N+1$ vertices (or points), in N dimensions, and all their interconnecting line segments, polygonal faces, etc. In two dimensions, a simplex is a triangle, in three-dimensional it is a tetrahedron and so forth. In general, interest only simplexes that are nondegenerate, which enclose a finite inner N -dimensional volume.

The simplex method must be started with $N+1$ points, defining an initial simplex. At the beginning, the step consist of a locating starting vertex on the simplex, \mathbf{P}_0 . The other n point are given as:

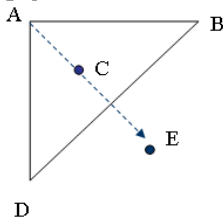
$$\mathbf{P}_i = \mathbf{P}_0 + \lambda \mathbf{e}_i \quad (5.9)$$

Where the \mathbf{e}_i 's are N unit vectors, and λ is a constant that represents the problem's characteristic length scale.

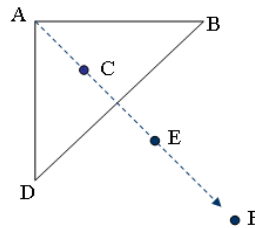
The method can be roughly divided in a series of steps. Most steps moving the point of the simplex where the cost function is largest ("highest point") through the opposite face of the simplex to a lower point. These steps are called reflections, and they are constructed to conserve the volume of the simplex. The method expands the simplex in one or another direction to take the larger steps. When it reaches a "valley floor", the method contracts itself in the transverse direction and tries to ooze down the valley. The method, then, contracts itself in all directions, and pulling itself in around its lowest (best) point. The basic moves are summarized in Figure 5.1.

The simplex at the beginning of the step, here is a triangle.

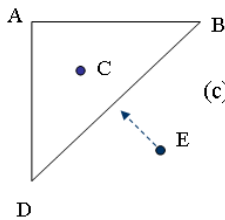
High point



(a) A reflection away from the high point



(b) A reflection and expansion away from the high point



(c) A contraction along one dimension from the high point toward the low point

A suitable sequence of the step will always converge to a minimum of the cost function

Figure 5.1. Outline of a step in the downhill simplex method.

Termination criteria can be delicate in any multidimensional minimization routine. It is possible to identify one "cycle" or "step" of a multidimensional algorithm, and the step terminates when the vector distance moved in that step, is fractionally smaller in magnitude than some tolerance. Alternatively, it can be required that the decrease in the function value in terminating step, be fractionally smaller than some tolerance. An appropriate sequence of the step will always converge to a minimum of the function (Numerical Recipes, 1987).

5.4. Spectrum computation

In order to estimate the Fourier spectra of the earthquakes, all records were first corrected to zero baseline removing mean and linear trend. A cosine taper function (5%) was then applied to a selected time window beginning from the S-wave arrival time for the north-south (NS) and the east-west (EW) components. Both components have been then filtered (band-pass filter between 0.075 and 30 Hz) and integrated two times in order to obtain the displacement spectra.

The resultant horizontal displacement spectrum has been estimated as:

$$O(f) = \sqrt{(NS(f))^2 + (EW(f))^2} \quad (5.10)$$

where $O(f)$ is the resultant of the Fourier displacement amplitude spectra of the NS and EW components.

Spectra of earthquakes are considered valid only when the signal-to-noise (S/N) ratio is greater than 2 in the frequency band 1-25 Hz, with respect to the pre-event noise window.

The spectral amplitudes were smoothed using an arithmetic smoothing algorithm to each data point.

The size of the window is defined by specifying its halfwidth of 5 points.

A critical point in the analysis is the selection of the time window enclosing the S-phase, in order to compute the S-wave spectrum. Generally, for site effects study the window length is chosen so as to contain at least the 90-95% of the total S-wave energy. For this work, time windows beginning 0.7 seconds before the S-wave arrival time have been selected, with a total duration of 5 seconds. The choice to use time windows of 5 seconds seemed to be a good compromise between the need to select S waves only and the need to get 90-95% of the S-waves energy.

Figure 5.2 shows an example of the 5 seconds time window used to compute the spectra.

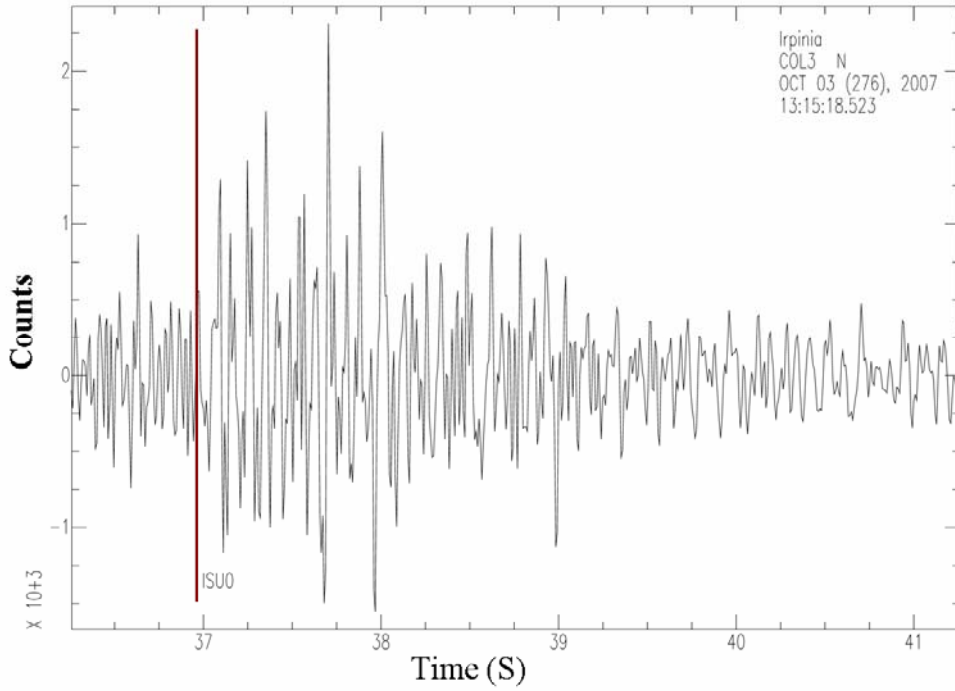


Figure 5.2. Time window to extract the S waves: 0.7 s before, 4.3 s after the S arrival time.

5.5. Description of the inversion method

The displacement spectrum of i th seismic event recorded at the j th receiver, $O(f)_{ij}$, can be modeled as the product of three physical parameters:

$$O(f)_{ij} = S(f)_i P(f)_{ij} G(f)_j \quad (5.11)$$

where $S(f)_i$ is the source effect of the i th earthquake, $P(f)_{ij}$ is the propagation path from the i th source to the j th receiver, and $G(f)_j$ is the site effect of the j th receiver. A non-linear inversion technique based on the Simplex algorithm has been used to solve the non-linear problem and retrieve these different terms.

In order to estimate the source spectra, the observations must be corrected for the propagation path and site effects. Considering a geometrical spreading of the form R^{-1} , and an anelastic attenuation factor parameterized by a frequency dependent quality factor of the form $Q(f) = Q_0 (f/f_0)^n$, the propagation-path effect, $P(f)_{ij}$, for the radiation of S-waves from a point source has the following form:

$$P(f)_{ij}^* = R_{ij}^{-1} e^{-\pi R_{ij} f / Q(f) V_s} \quad (5.12)$$

where R_{ij} is the hypocentral distance from the i th source to j th station. In the present thesis, we assumed a quality factor $Q(f) = Q_0 (f/f_0)^n$ ranging from 60 to 160, with n ranging from 0.1 to 0.5 (Malagnini et al., 2000). V_s is the mean shear-wave velocity ($V_s = 3.2$ km/s).

The effect of the geometrical spreading has been approximated as $1/R$ since only S-waves are included in the selected time windows.

An average S-wave radiation pattern coefficient of 0.70 has also been employed, corresponding to a 30° dip, dip-slip faults, as calculated by Boore and Boatwright (1984).

Substituting (5.12) into the (5.11) equation, and solving for the source term it's obtained:

$$S(f)_{ij} = \frac{O(f)_{ij}^*}{G(f)_j} \quad (5.13)$$

where

$$O(f)_{ij}^* = R_{ij}^{-1} e^{-\pi R_{ij} f / Q(f) V_s} O(f)_{ij} \quad (5.14)$$

is the observed spectrum for the i th seismic event at the j th receiver, corrected by the propagation-path effect. In a nutshell, correcting all records from a given station by the propagation effect, it is possible to isolate the source and the site effect.

The site effect at the j th station, $G(f)_{ij}$, is then calculated from the spectral ratio between the corrected amplitude displacement, $O(f)_{ij}^*$, and the corresponding proposed source model $S(f)^*$ (Tsurugi et al. 1997):

$$G(f)_{ij} = \frac{O(f)_{ij}^*}{S(f)^*} \quad (5.14)$$

where $S(f)^*$ is the far-field displacement spectrum given by Brune's model (Brune, 1970):

$$S(f)^* = \frac{\Omega_0}{\left[1 + \left(\frac{f}{f_0} \right)^2 \right]} \quad (5.15)$$

where Ω_0 is the low-frequency flat level, f_0 is the corner frequency, and f is the frequency.

Since each station can have as many site effects as observed spectra, the average and the normalized

standard deviation have been calculated.

Assuming that the site response at a given station is independent of the input earthquakes, the inversion method searches values for the corner frequency f_0 and the low-frequency flat level, Ω_0 , from the corrected displacement spectrum at the surface, and proposes different source models for each earthquake. The flat levels and corner frequencies obtained at the end of every inversion are the ones that correspond to the most stable site effect estimation.

Figure 5.3 illustrates the inversion method.

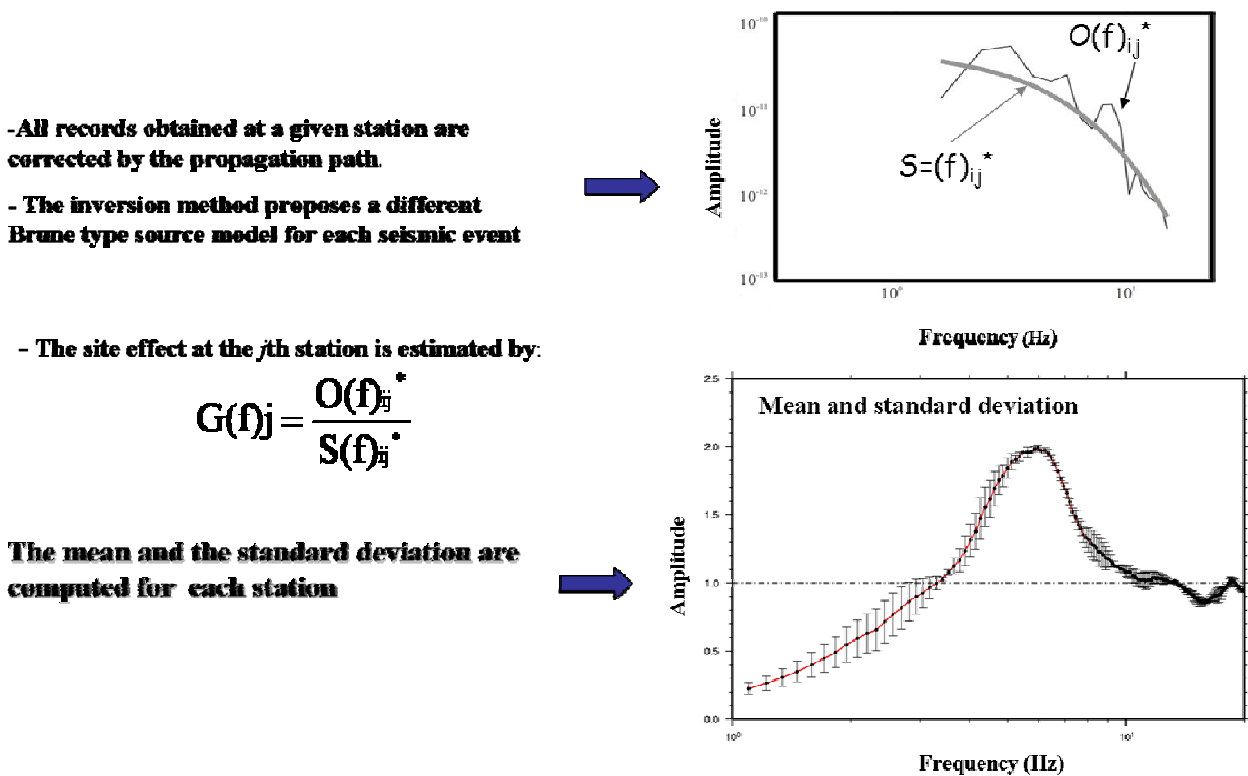
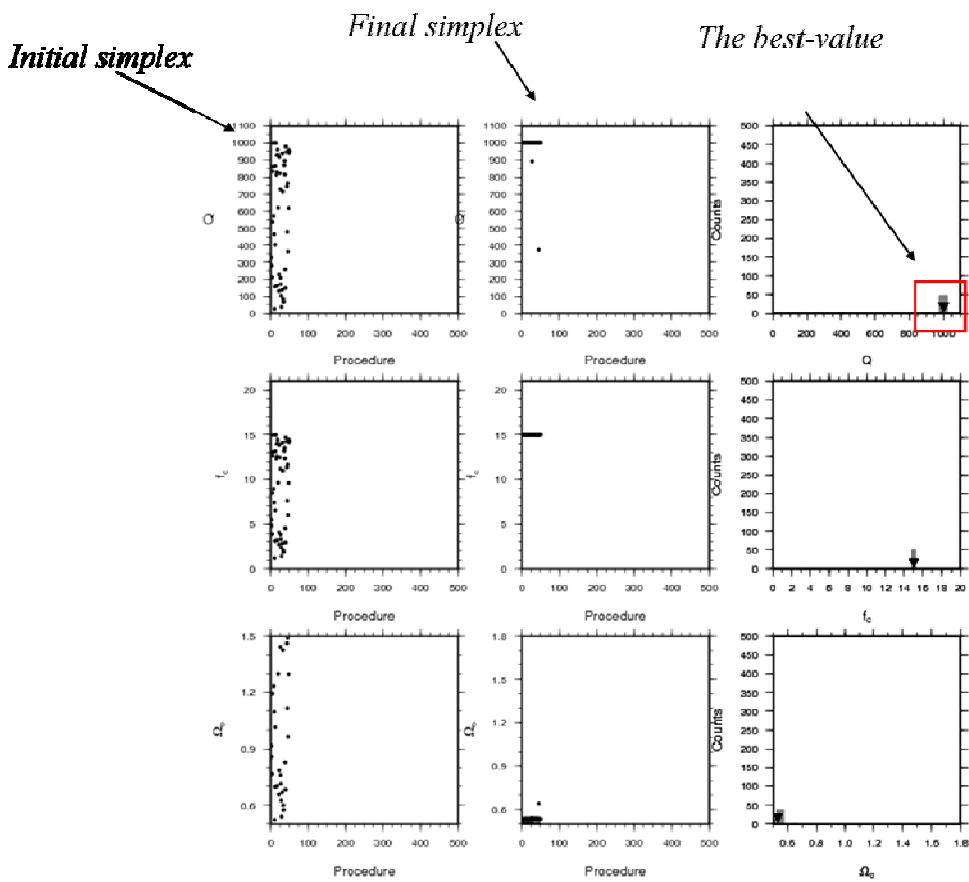


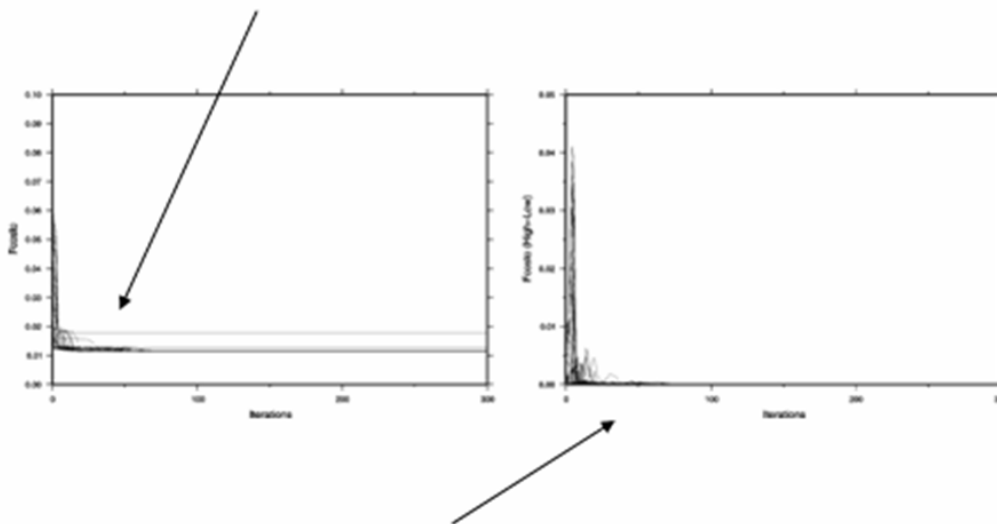
Figure 5.3. Outline of the inversion scheme to estimate the source spectrum and site effect.

5.6. Inversion results

The inversion has been performed for a total of 200 procedures and 1000 iterations. In general, the convergence of the simplex algorithm has been fast: the results didn't change much after the 50th procedure (Figure 5.4).



Trend of the cost-function



Difference between the lower and higher value of the cost-function

Figure 5.4. The simplex convergence and evolution and differences between the lower and higher value of the cost-function.

Figure 5.5 shows the corrected horizontal component of displacement spectra for two selected events. Note how the two events presented in the Figure 5.5 seem to have a corner frequency at around 4- Hz. The tendency, presented by most of the displacement spectra of having low values of the source-originated corner frequencies, could be caused by strong attenuation at high frequency due to the surface deposits. This effect becomes an important problem when trying to estimate the source parameters of small seismic events. Indeed, the site effect tends to modify the true value of corner frequencies.

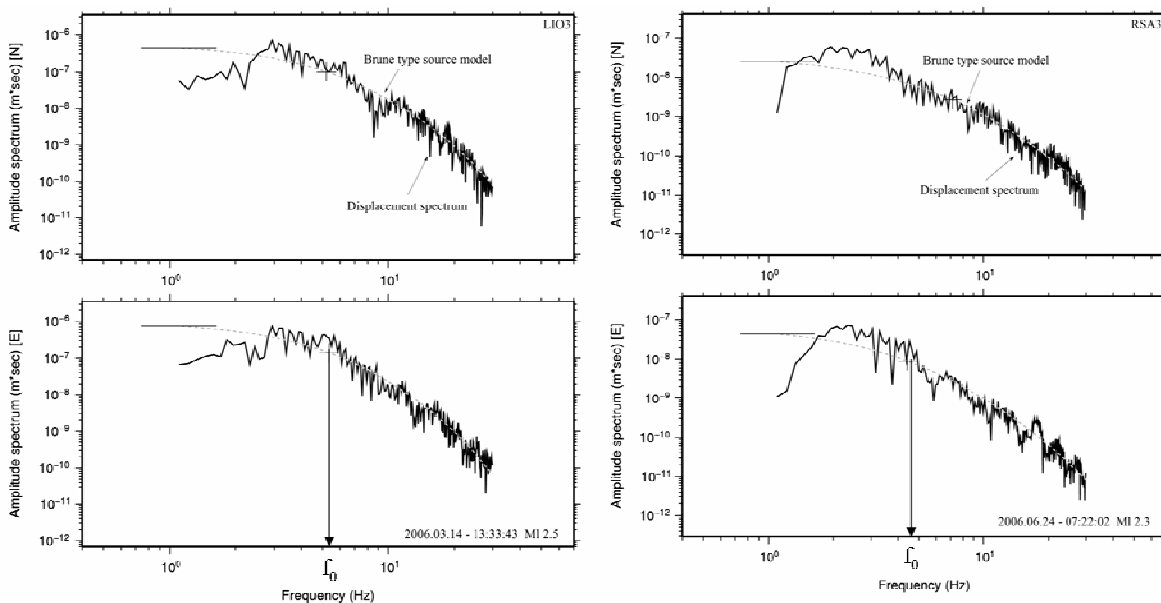


Figure 5.5. The corrected displacement spectra for two selected events (only the horizontal components). Both events seem to have a corner frequency at around 4-5 Hz. This is caused by the site effect.

The resulting site transfer functions obtained by the inversion of 106 recorded events, are shown in Figure 5.6. All Figures, one for every station, are formed by six plots: a bar chart representing the magnitude distribution of earthquakes recorded at the selected station, four plots to represent the spectral ratios as a function of the azimuth with respect to the events, and a central plot showing the average site effect (red line) and the corresponding standard deviation (black lines). All the seismic stations show spectral ratios that are quite similar in shape, and not directionally dependent.

The first thirteen Figures present the site effects for 13 stations belonging to the Mesozoic site class, the following nine Figures show the site effects for 9 stations belonging to the Tertiary site class, and the last one shows the site effect estimated for the only station belonging to the Volcanic site class.

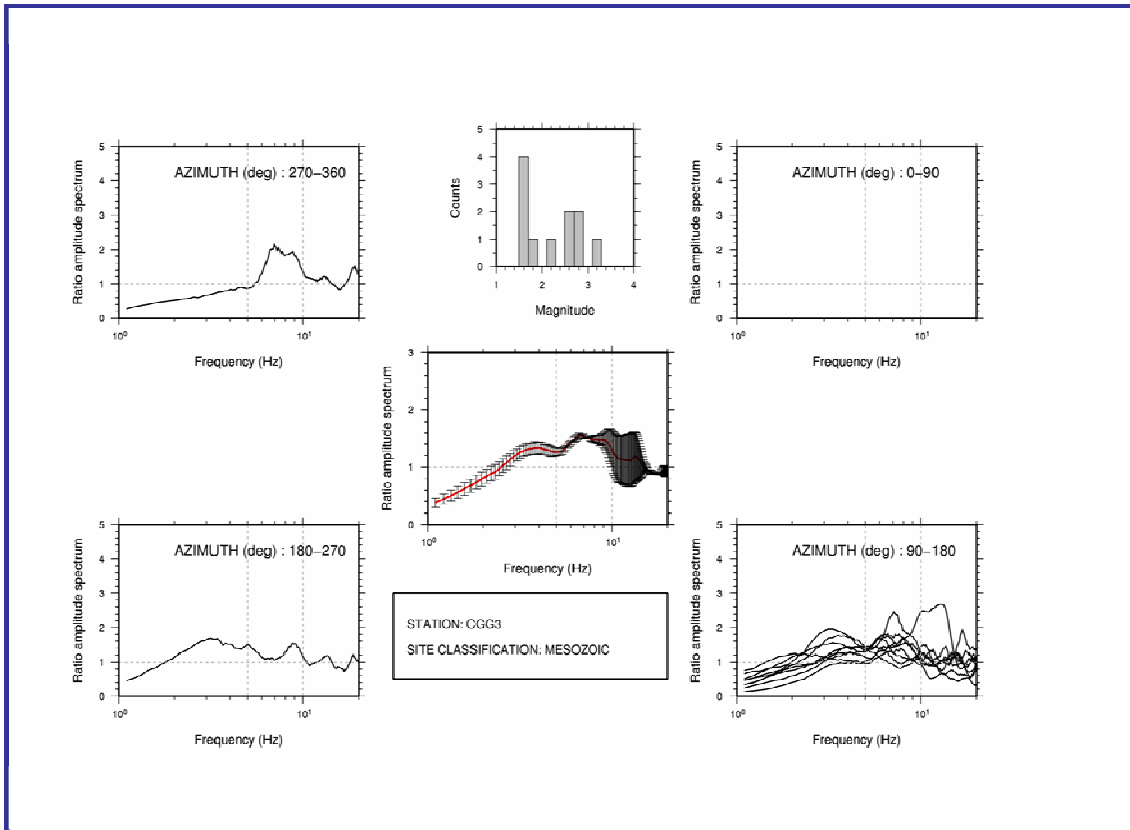
Note that the stations of the Mesozoic site class (*CGG3 CMP3, COL3, CSG3, NSC3, PGN3, PST3, SCL3, SFL3, SNR3, SRN3, STN3, VDS3*), are not completely devoid of amplification at the surface.

In particular, all spectral ratios present a significant deamplification for frequencies below 2-3 Hz, and peaks of amplification above 5 Hz. However, although at some stations the amplification is peaked at certain distinct frequencies, at other stations (*COL3*, *NSC3*, *SRN3*, *STN3*, *SNR3*, and *SCL3*) the amplification occurs over a broader frequency range. These results agree with the hypothesis of rock sites with a velocity V_S^{30} about 800 m/s. Moreover, even if these stations are located on rock, according to geological maps, the resulting spectral ratios show that stations classified as rock sites can have significant site effects. In fact, as shown by Steidl et al., (1996), near-surface weathering and cracking affect the recorded ground motion.

Most of the stations located on soft rock and stiff soils of the Tertiary site class (*AND3*, *BEL3*, *CLT3*, *LIO3*, *RDM3*, *RSA3*, *RSF3*, *TEO3*, *VDP3*), show a level of amplification distributed over a broad frequency range, generally below 4-5 Hz, and only three stations, *BEL3*, *CLT3*, and *VDP3*, have the amplification peaked at certain distinct frequencies, between 3 and 5 Hz. These results are in good agreement with sites characterized by V_S^{30} ranging from 360 to 800 m/s.

The last Figure shows the site effect estimated for the VULT station located on a volcanic rock site. As expected, the amplification level is roughly constant, about 1.4, for frequencies below 5 Hz, and it decays rapidly at higher frequencies. The shape of the spectral ratio in the low-frequency range is theoretically appropriate for a volcanic rock site, characterized by volcanic units as pyroclastic flow deposits, surges and extensively fractured sodic potassic lavas.

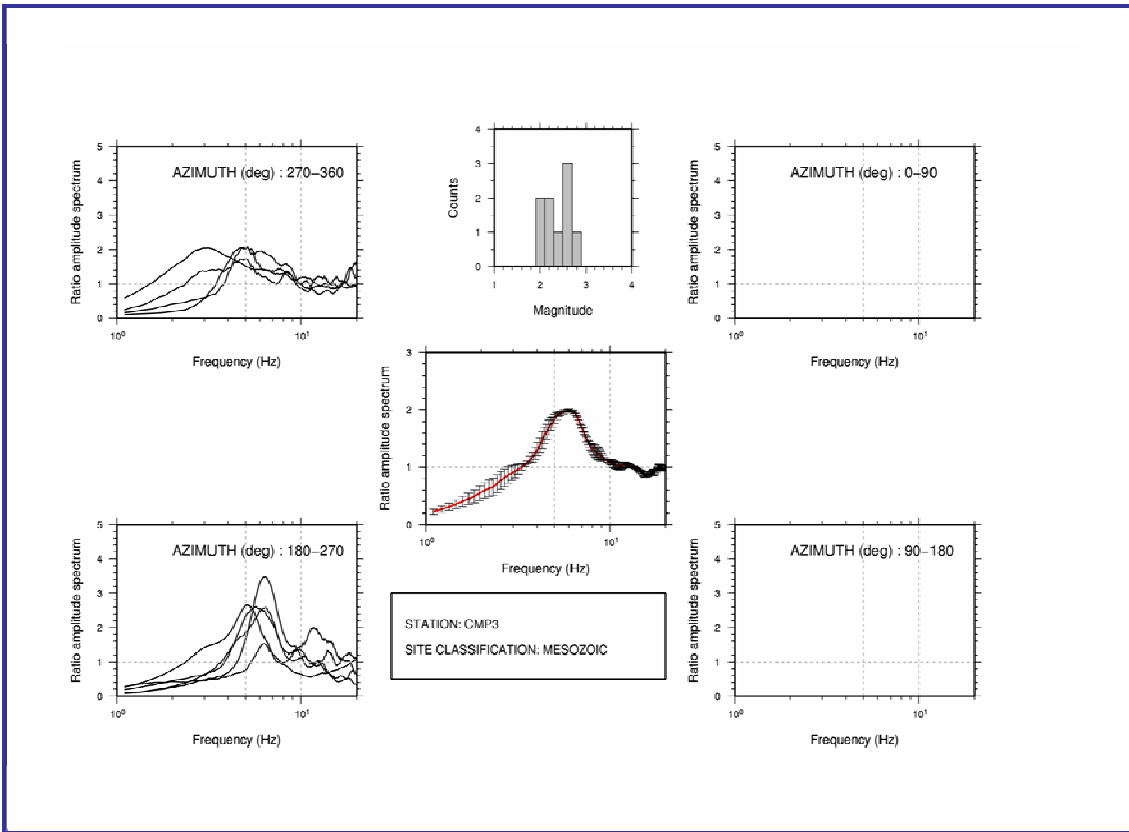
In light of these results, it is possible to state that the transfer functions obtained by the inversion technique for the Campania-Lucania region, do contain important information on the site effects. The stations located on stiff and soft soils (Tertiary) show a deamplification in the high frequency range, while rock sites (Mesozoic) present significant amplification at high frequencies. In particular, the surface-rock sites not present a flat response close to 1. In fact, also sites located on what appears to be a competent rock show amplification at frequencies above 5 Hz, this is because the rock site response is due to the weathered and fractured nature of the near surface. Therefore, these results suggest that the choice of one these sites as the reference site could lead to an underestimation of the seismic hazard analysis, and that techniques not requiring a reference site could, instead, give more reliable estimates of the site effects.



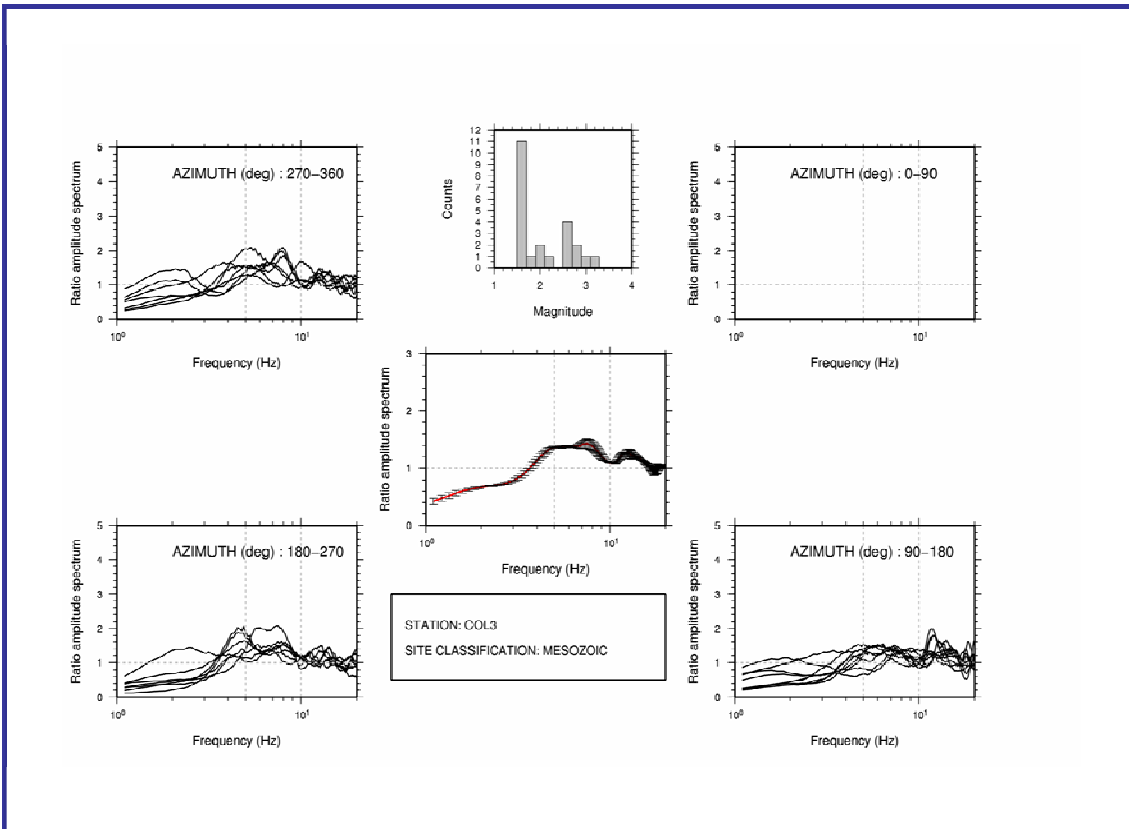
CGG3 seismic station - Mesozoic site class

Figure 5.6 a). Spectral ratios obtained by the inversion method of 106 seismic events.

All Figures, one for every station, are formed by six graphics: a bar chart to represent the number of events per magnitude range, four to represent the spectral ratios as a function of the azimuth with respect to the events, and a central graphic that shows the average site effect (red line) and the corresponding standard deviation. The first thirteen Figures show the site effects for 13 stations belonging to Mesozoic site class, the following nine Figures show the site effects for 9 stations belonging to Tertiary site class, and the last one shows the site effect estimated for the only station belonging to Volcanic site class.

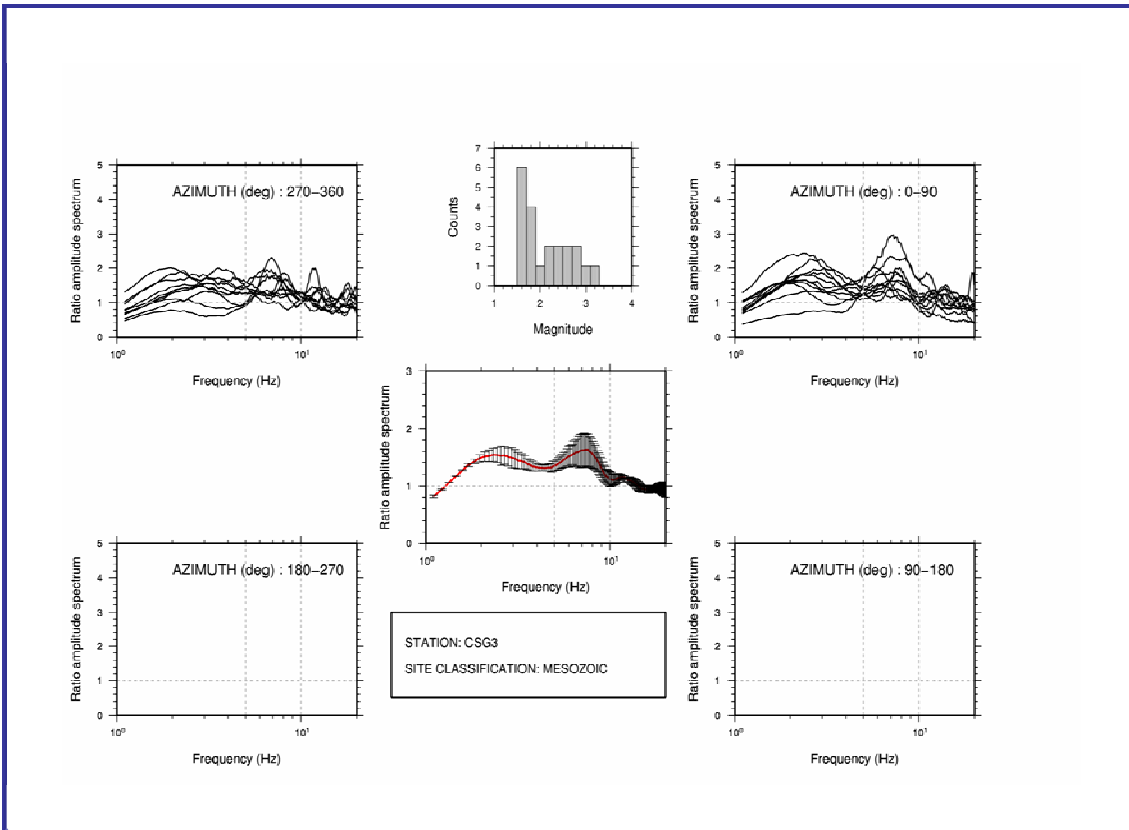


CMP3 seismic station - Mesozoic site class.

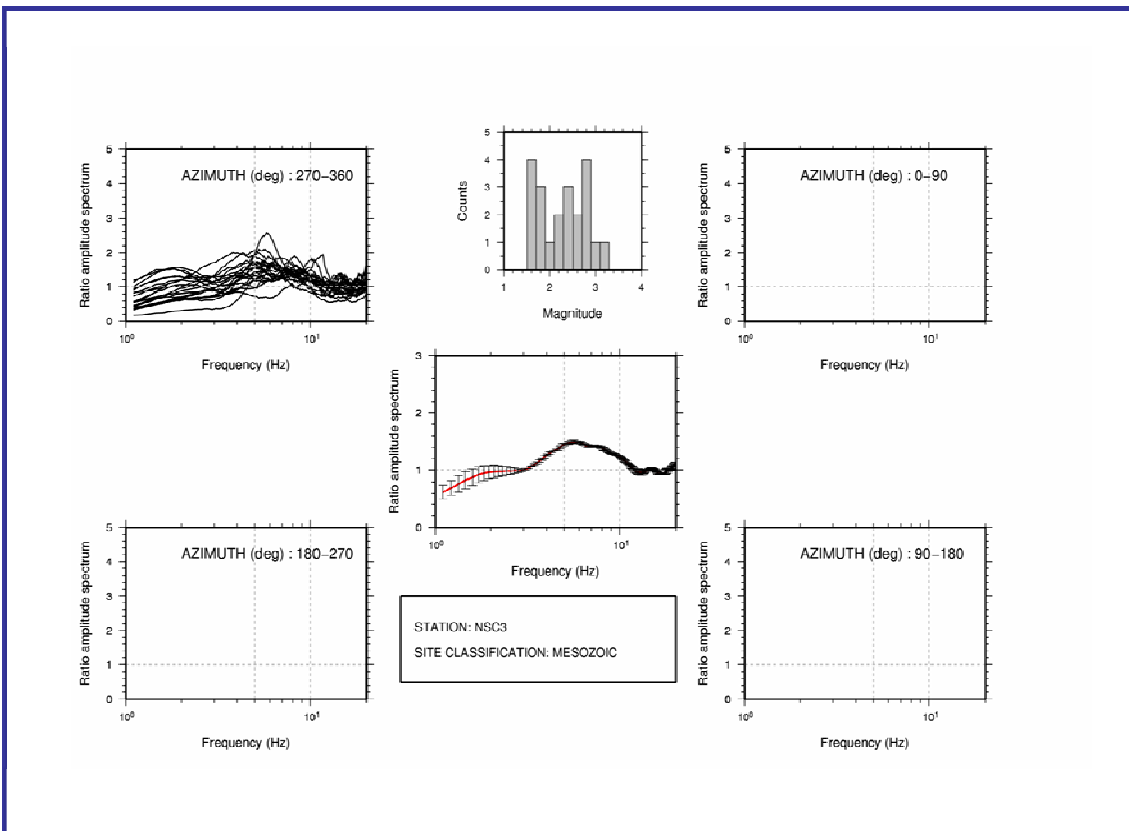


COL3 seismic station - Mesozoic site class.

Figure 5.6 b), and c). Same as figure 5.6a) but for CMP3 and COL3 stations.

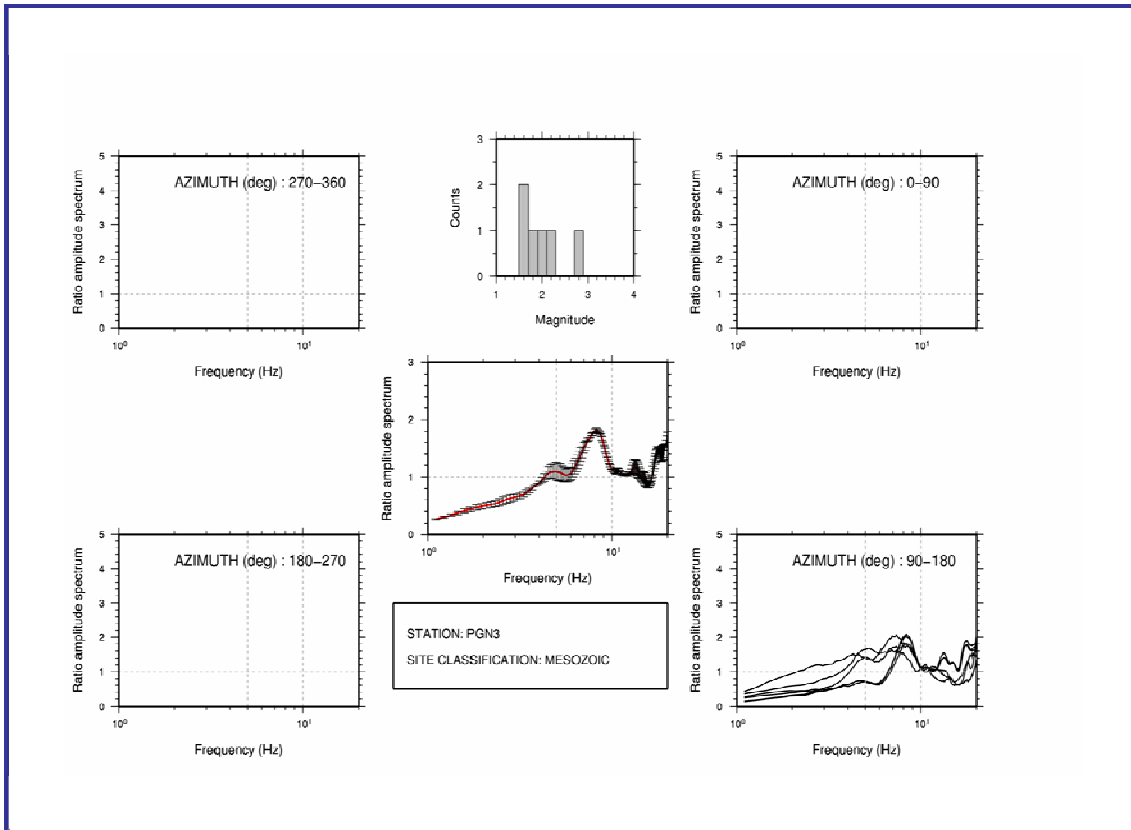


CSG3 seismic station - Mesozoic site class.

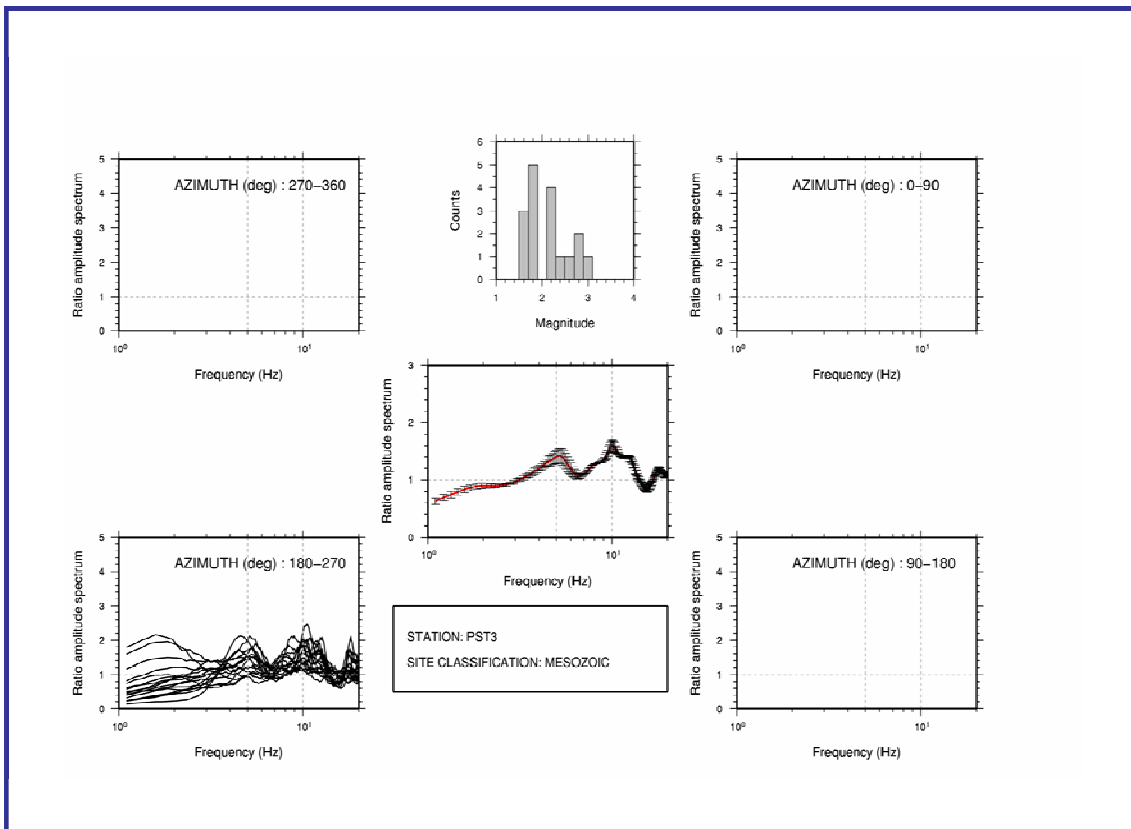


NSC3 seismic station - Mesozoic site class.

Figure 5.6 d), and e). Same as figure 5.6a) but for CSG3 and NSC3 stations.

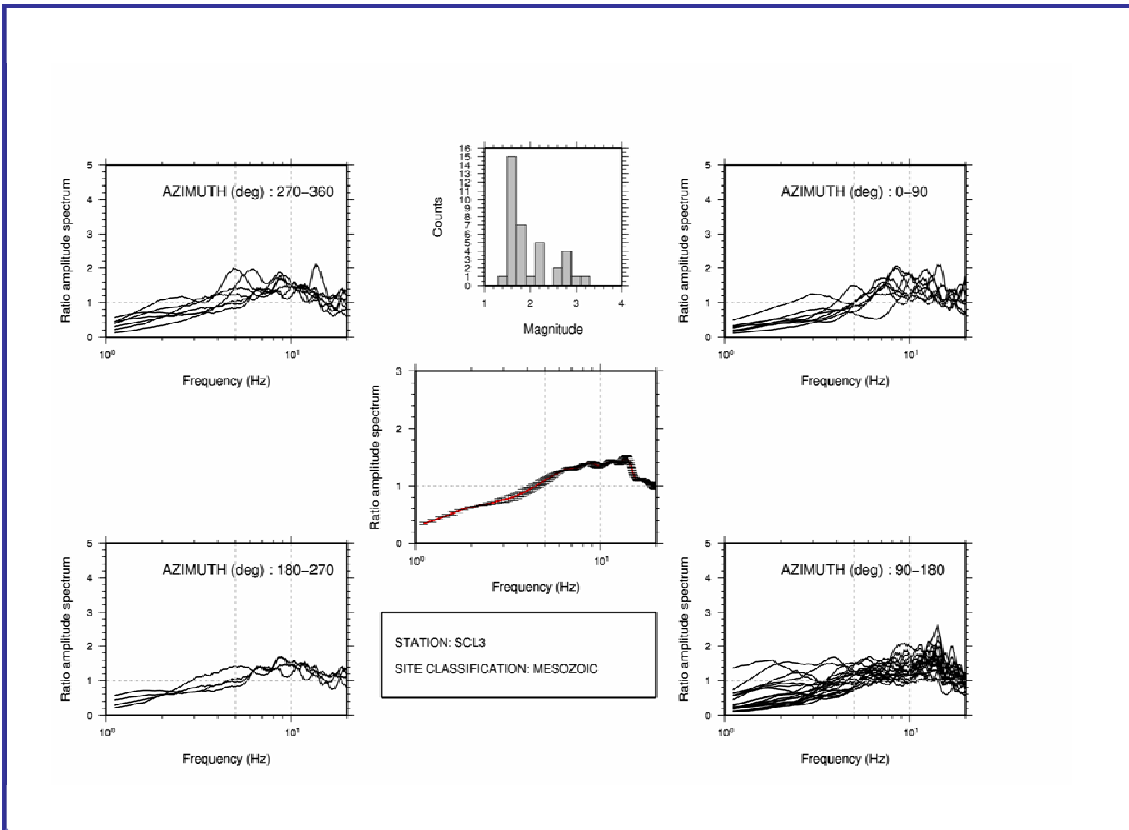


PGN3 seismic station - Mesozoic site class.

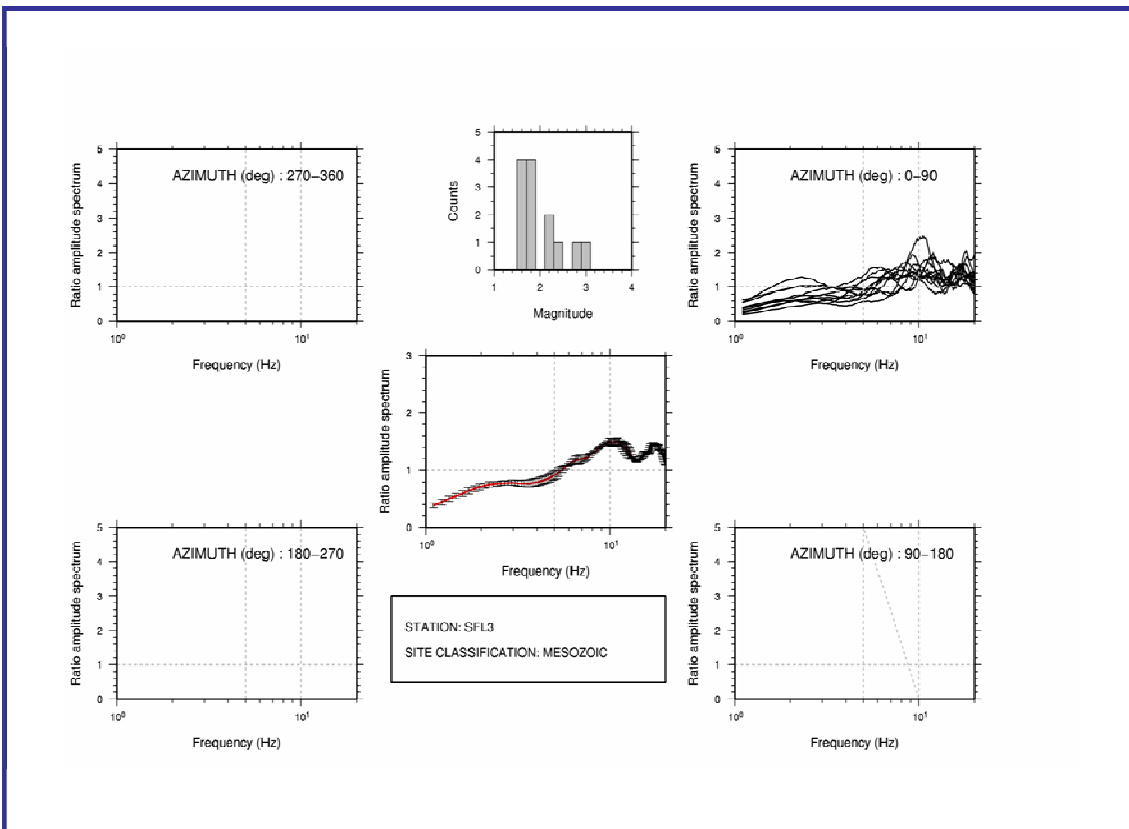


PST3 seismic station - Mesozoic site class.

Figure 5.6 f), and g). Same as figure 5.6a) but for PGN3 and PST3 stations.

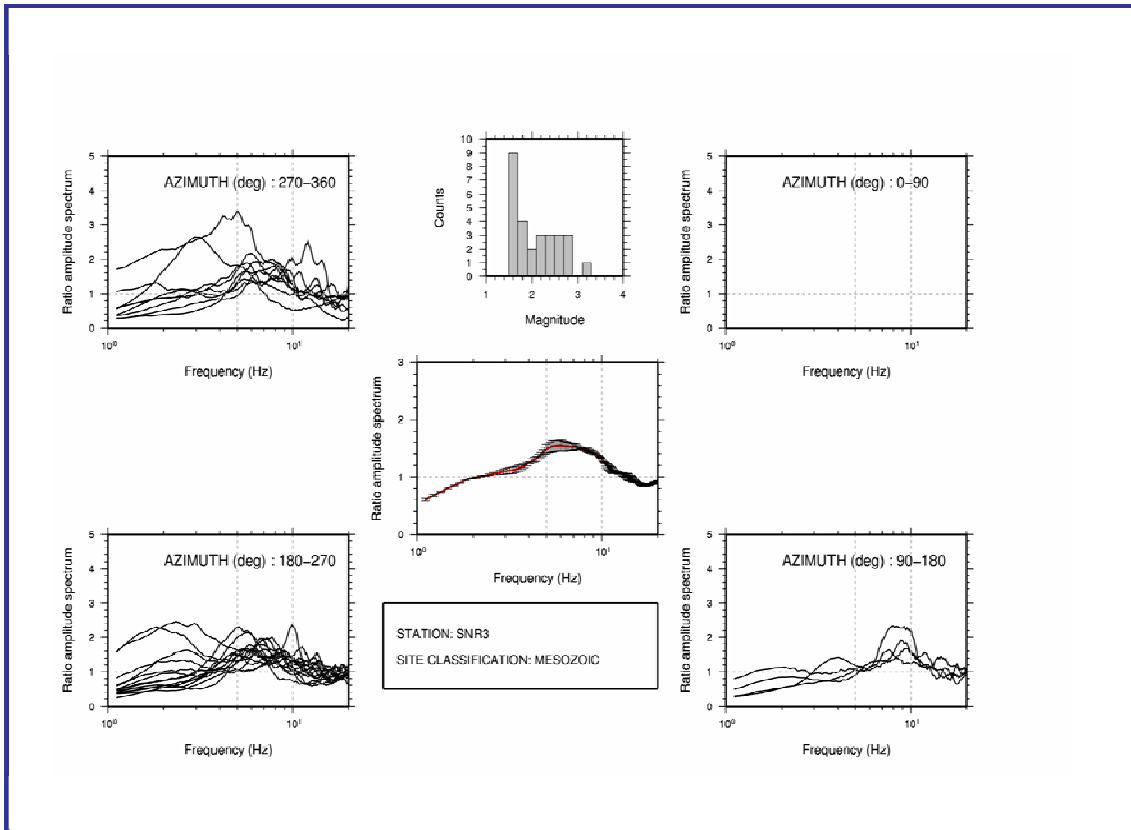


SCL3 seismic station - Mesozoic site class.

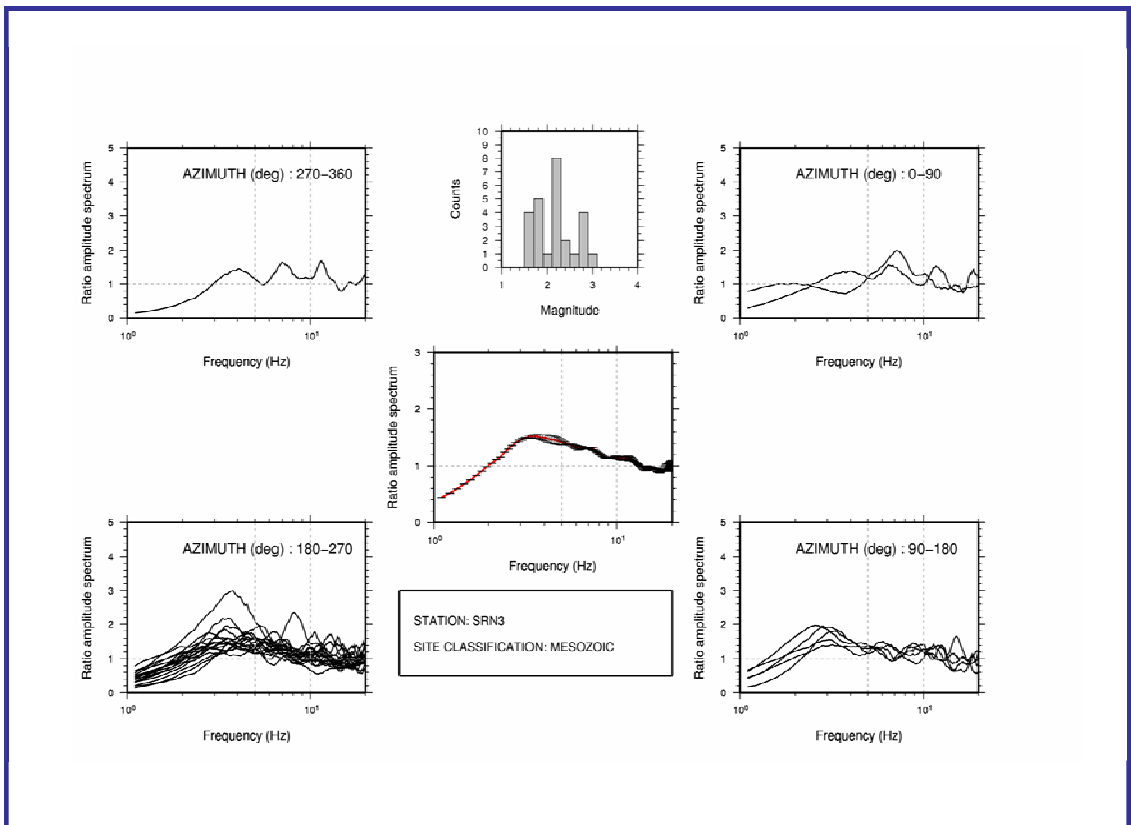


SFL3 seismic station - Mesozoic site class.

Figure 5.6 h), and i). Same as figure 5.6a) but for SCL3 and SFL3 stations.

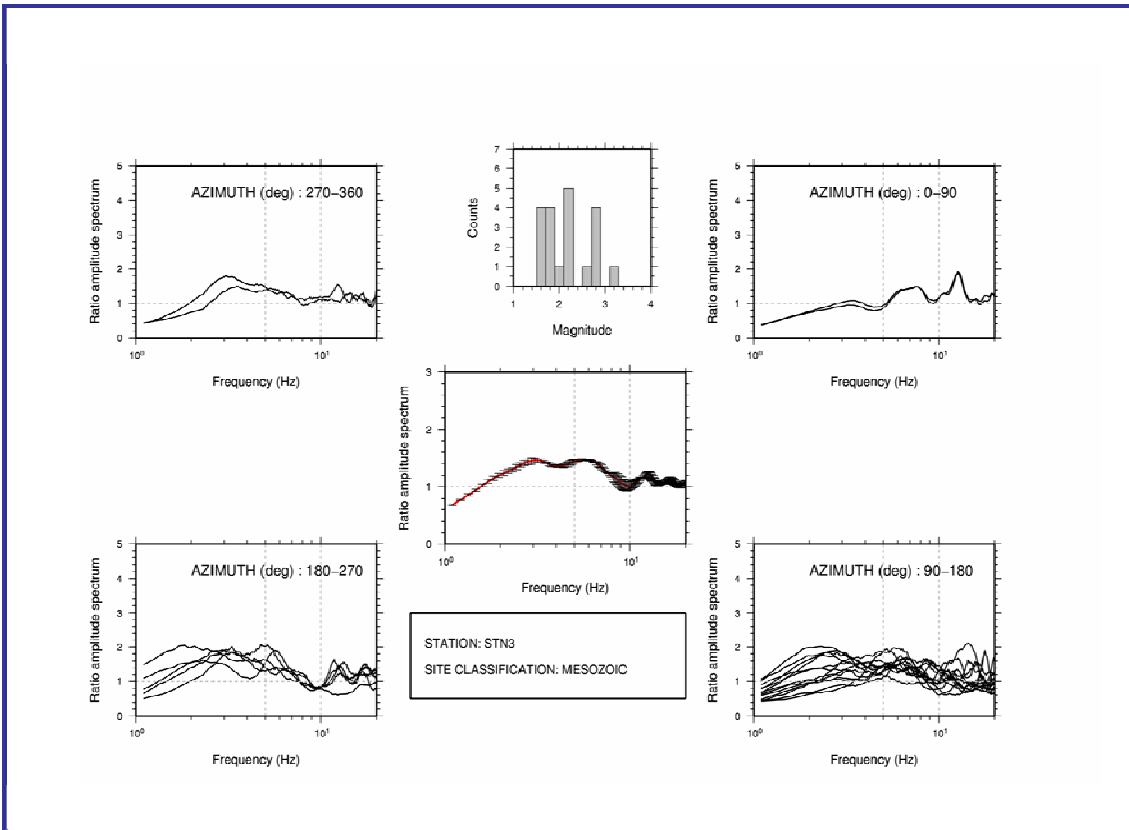


SNR3 seismic station - Mesozoic site class.

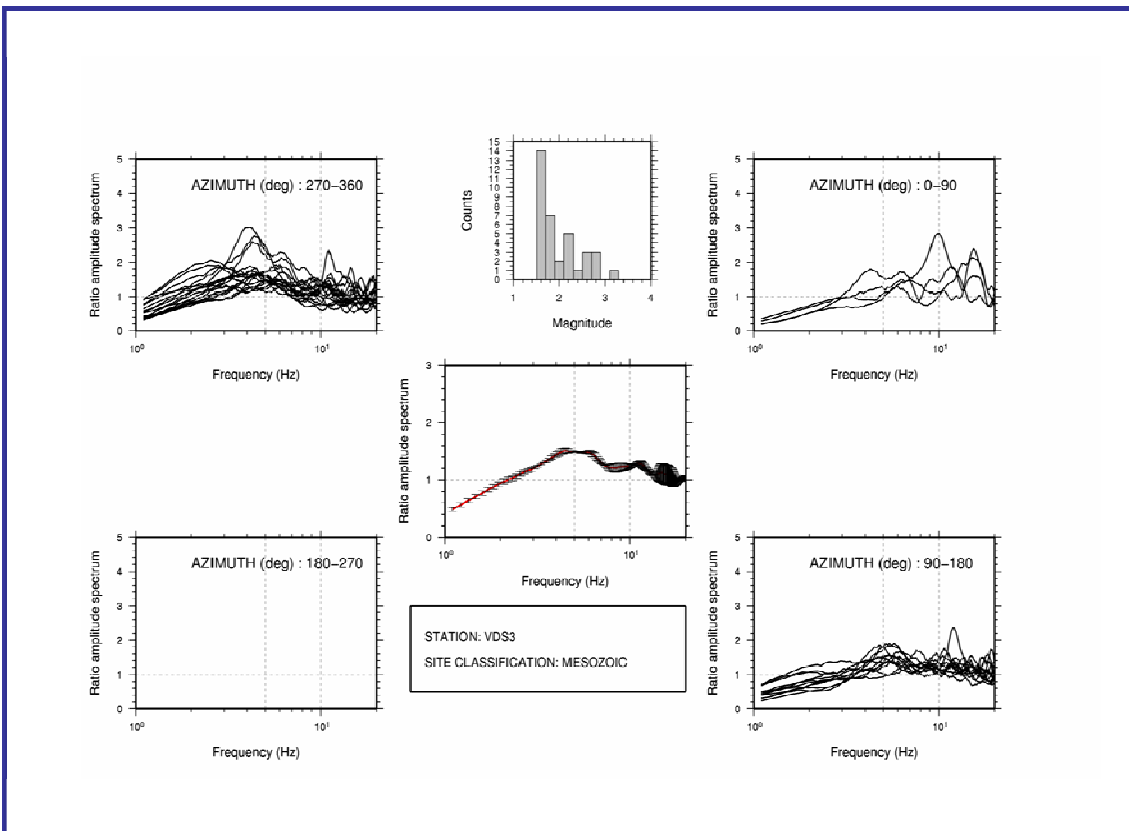


SRN3 seismic station - Mesozoic site class.

Figure 5.6 j), and k). Same as figure 5.6a) but for SNR3 and SRN3 stations.

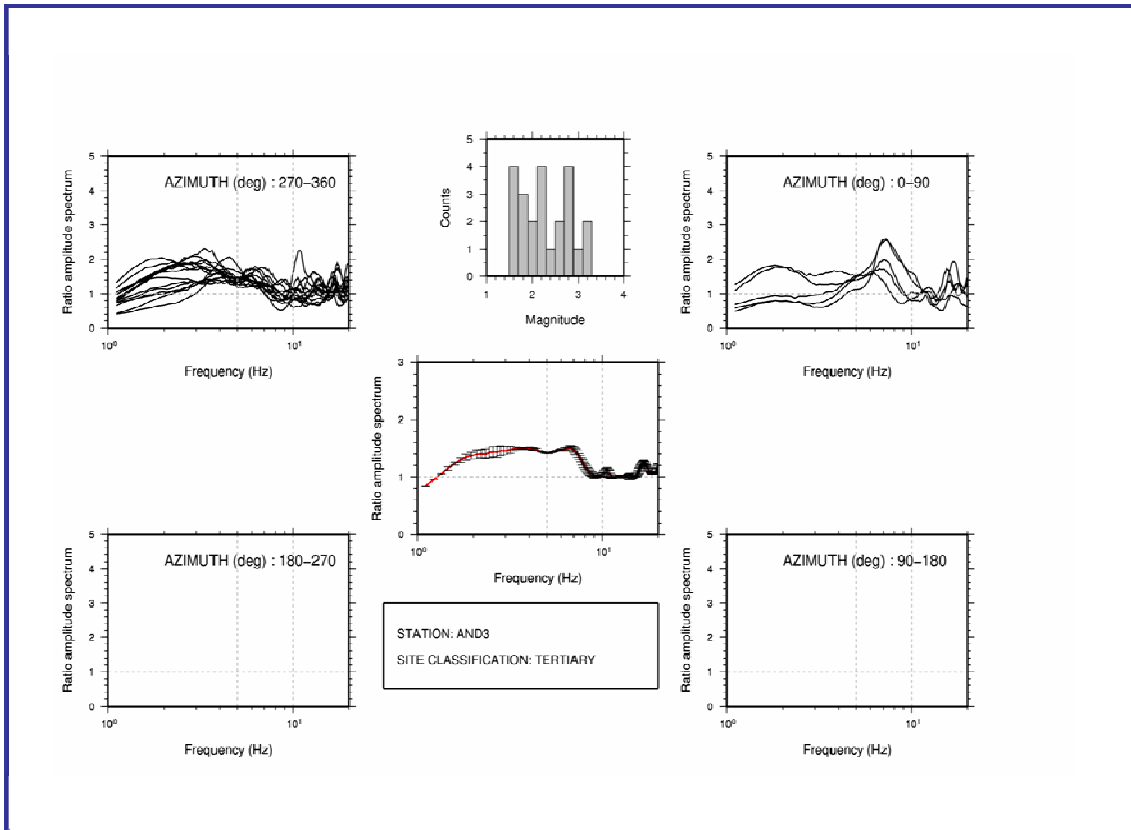


STN3 seismic station - Mesozoic site class.

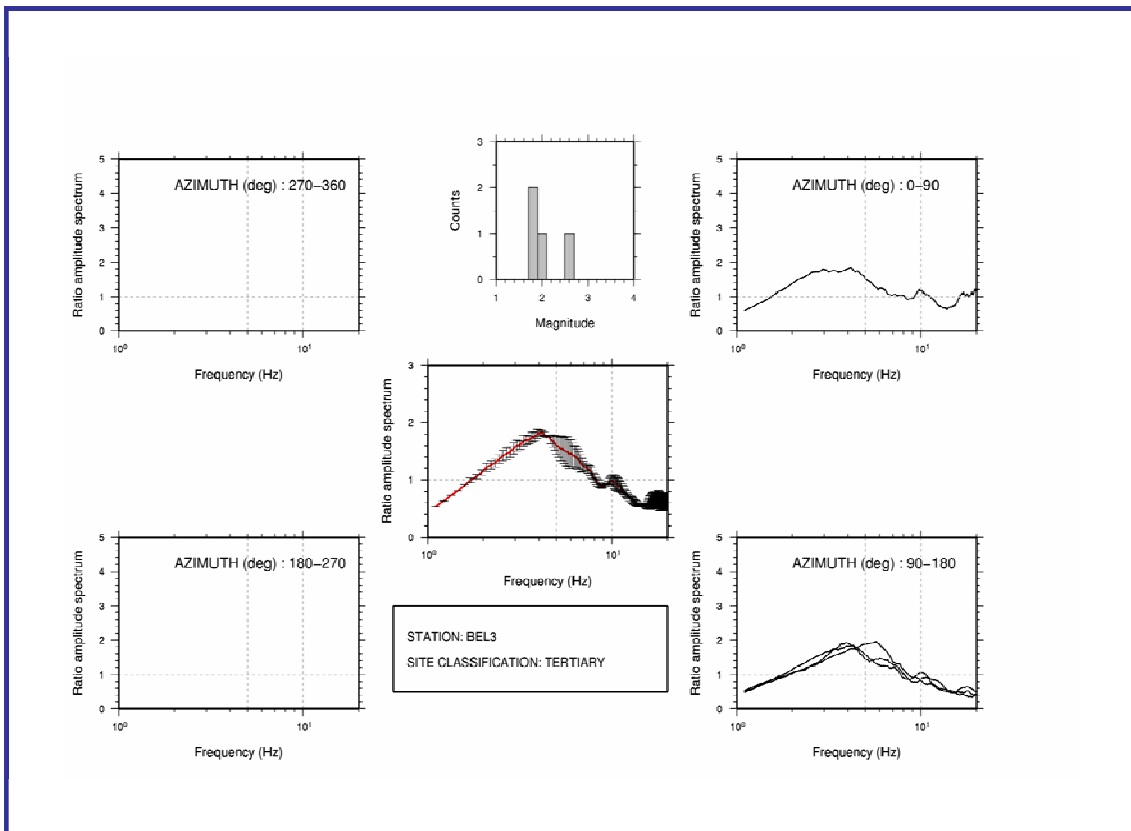


VDS3 seismic station - Mesozoic site class.

Figure 5.6 l), and m). Same as figure 5.6a) but for STN3 and VDS3 stations.

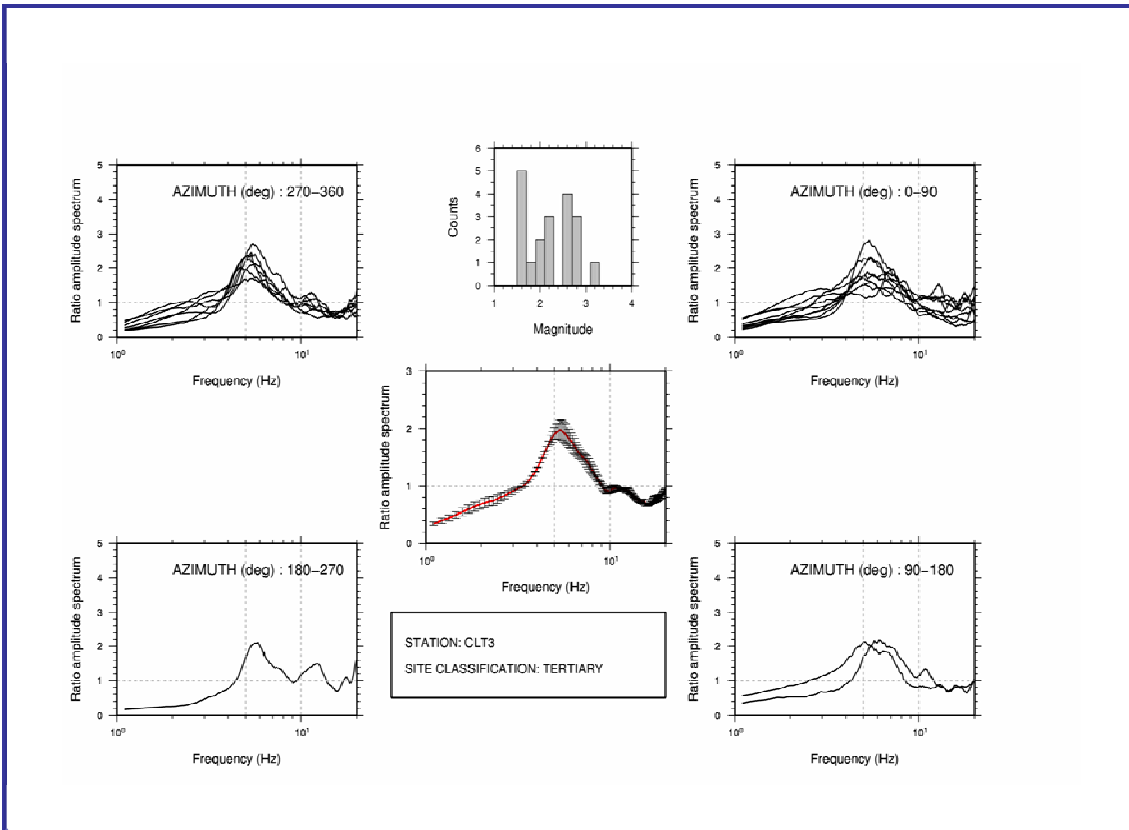


AND3 seismic station - Tertiary site class.

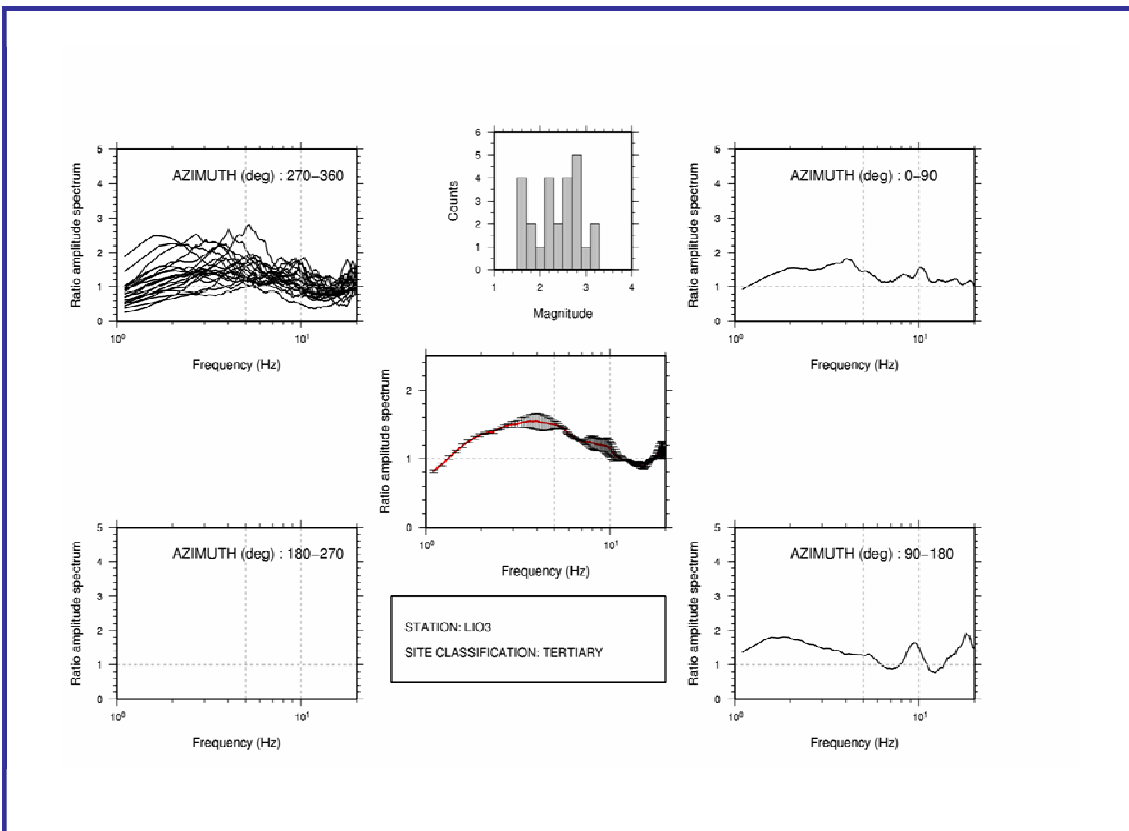


BEL3 seismic station - Tertiary site class.

Figure 5.6 n), and o). Same as figure 5.6a) but for AND3 and BEL3 stations.



CLT3 seismic station - Tertiary site class.



LIO3 seismic station - Tertiary site class.

Figure 5.6 p), and q). Same as figure 5.6a) but for CLT3 and LIO3 stations.

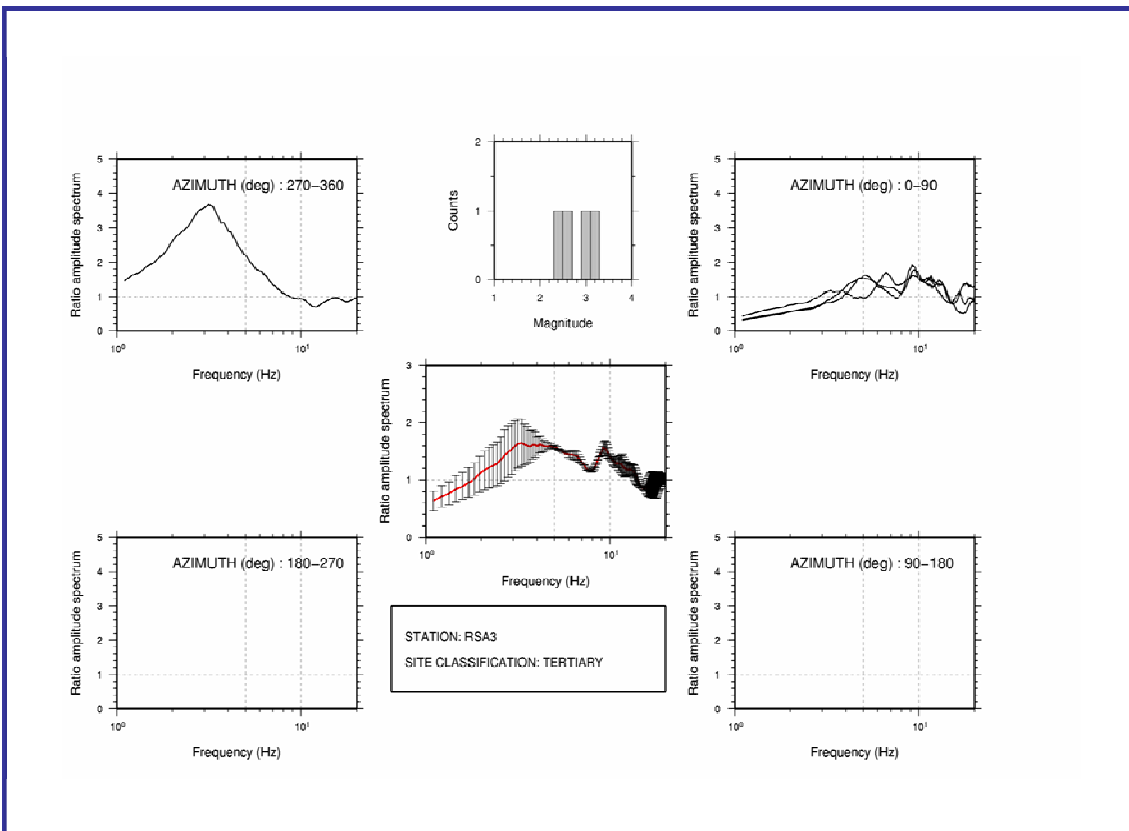
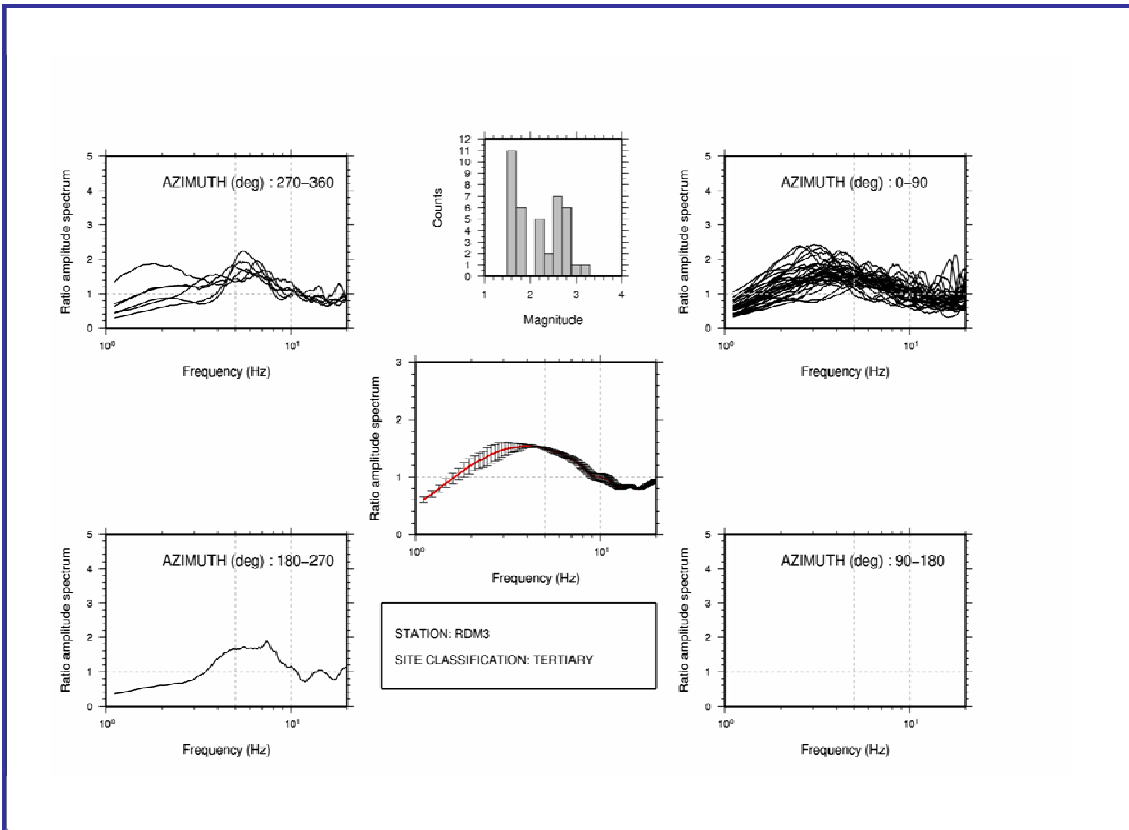


Figure 5.6 r), and s). Same as figure 5.6a) but for RDM3 and RSA3 stations.

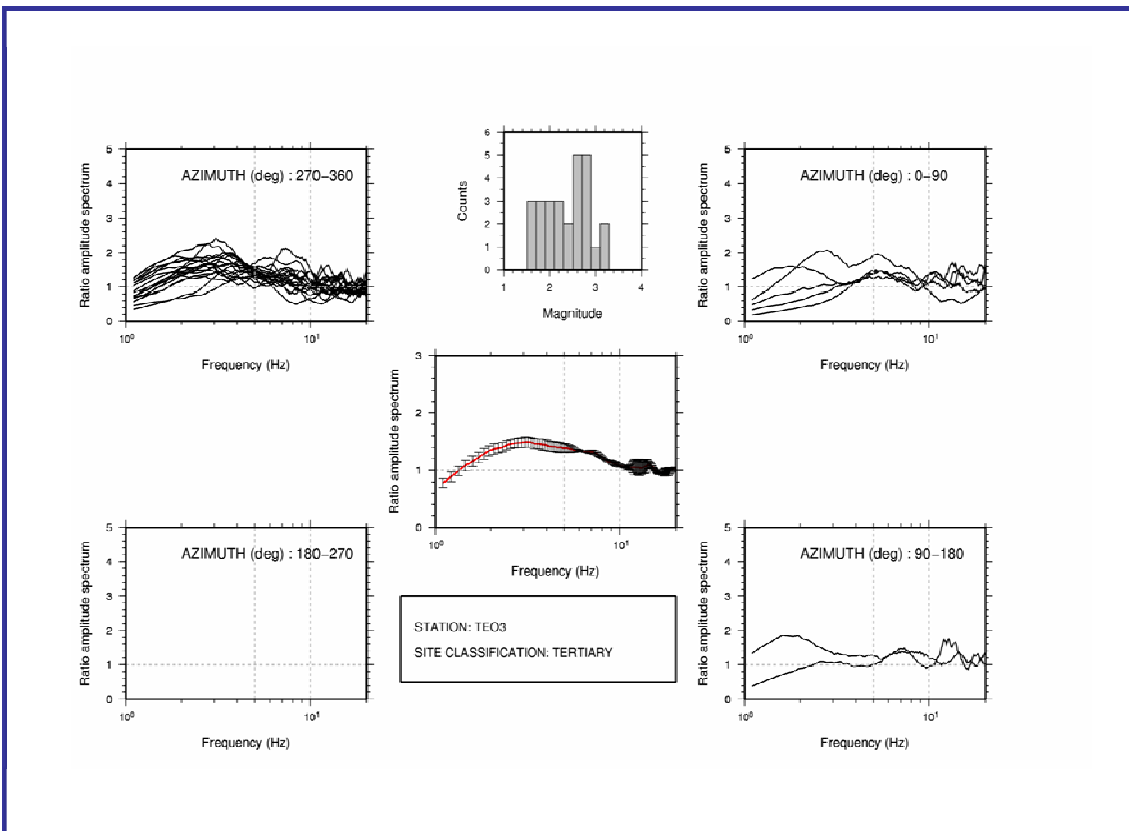
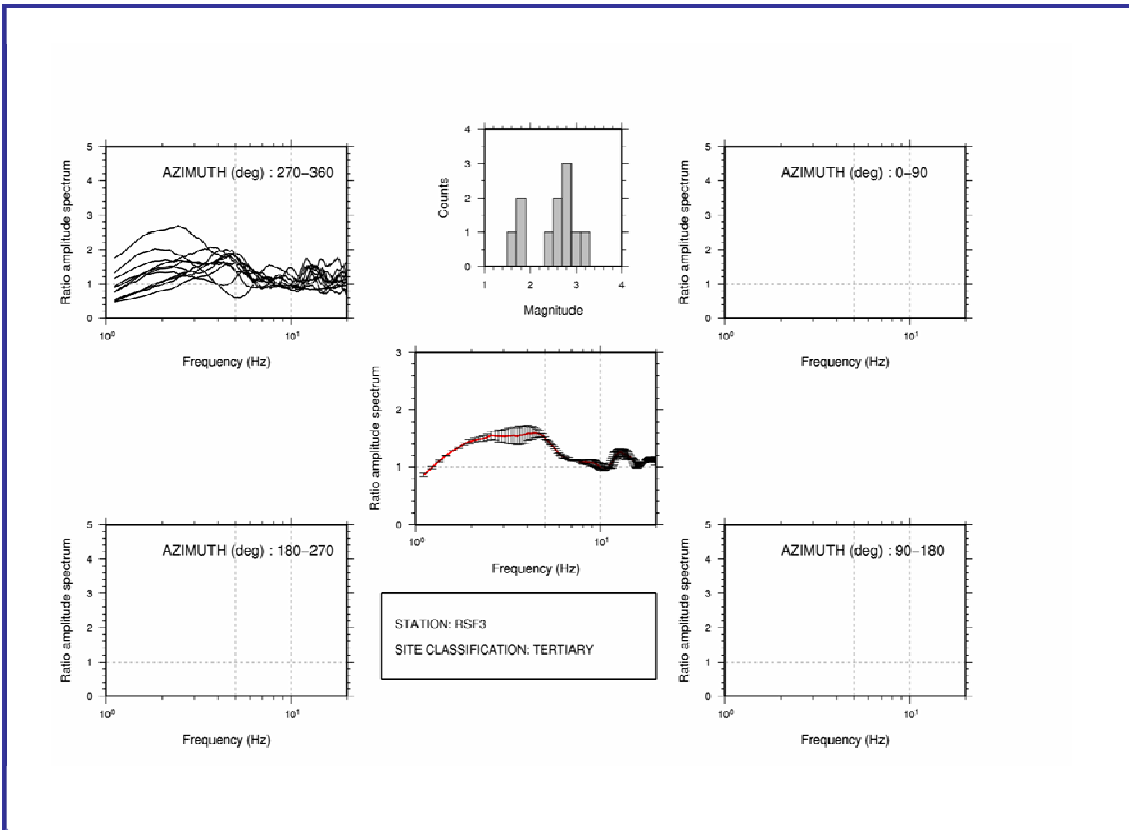
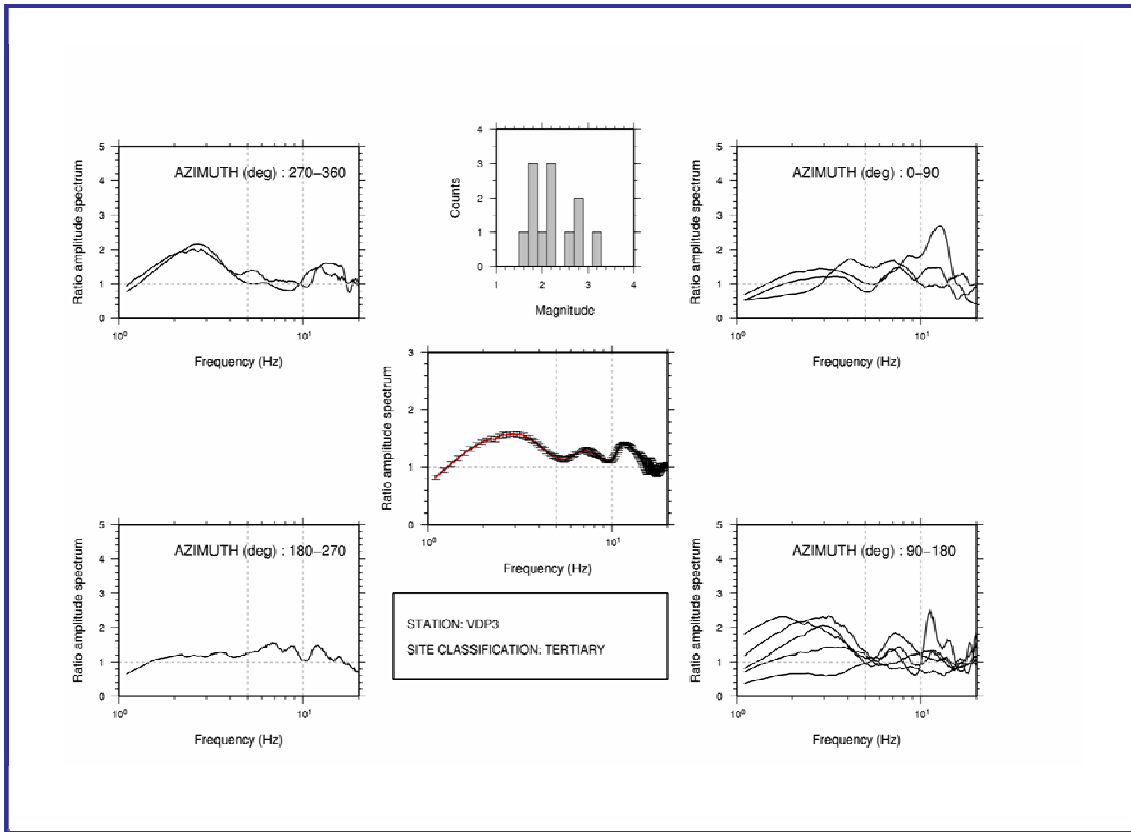
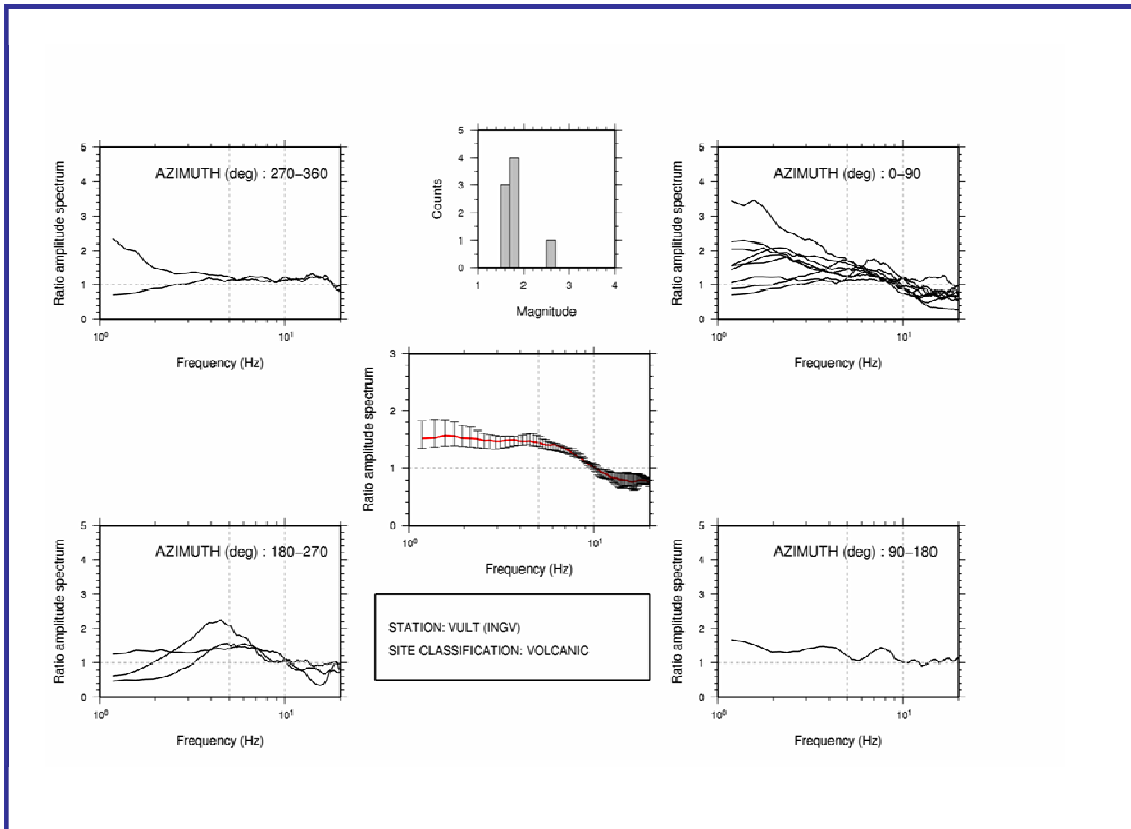


Figure 5.6 t), and u). Same as figure 5.6a) but for RSF3 and TEO3 stations.



VDP3 seismic station - Tertiary site class.



VULT seismic station - Volcanic site class.

Figure 5.6 v), and w). Same as figure 5.6a) but for VDP3 and VULT stations.

5.7. Site amplification maps for the Campania-Lucania region

Site amplification spectra are averaged within three frequency bands: the first-frequency band (Ib) from 1 to 5 Hz, the second-frequency band (IIb) from 5 to 10 Hz, and the third-frequency band from 10 to 20 Hz (IIIb). These bands are chosen based on the size of the analyzed earthquakes, to retrieve the amplification factors for different input ground motion parameters, such as PGA, PGV or Sa(T), that are "moderate-to-high" frequency parameters.

Means and standard deviations of the site responses, estimated using the inversion results, are shown in Table 2, along with the site class descriptors.

Site class:	Mean C-Ib (1-5Hz)	σ Ib	Mean C-IIb (5-10Hz)	σ IIb	Mean C-IIIb (10-20Hz)	σ IIIb	N. Stations
Q							
V	1.500		1.500		0.903		1
T	1.605	0.146	1.550	0.179	1.095	0.544	9
M	1.385	0.233	1.562	0.166	1.217	0.143	13

Table 2. Means and standard deviations of site amplifications grouped by the surface geology category.

In Table 2 it can be noticed that the average Ib amplification at Tertiary sites is higher than the IIb amplification. The lower IIb amplification compared to the Ib one, is in part due to the attenuating nature of stiff and soft soils on high-frequency strong-motion signals. Moreover, the amplification factors vary more strongly with the age at lower frequencies.

The observed relative amplification at rock sites in all the frequency bands, on the one hand may be due to a topographic effect, since many rock sites are located on mountains or hills, and on the other hand it may be caused by the weathered and fractured nature of near-surface materials.

In order to correlate these average horizontal spectral levels with the surface geology, three maps have been constructed, one for each frequency band, displaying the mean frequency bands over the QVTM site conditions map (Figure 5.7). Circles are centred on strong-motion sites, with diameter proportional to the average amplification. Significant correlations with the three frequency bands

have been found, suggesting that the site spectral amplification is also influenced by the nature of near-surface materials. In particular, soil sites showed higher amplification than rock sites for frequencies shorter than about 5 Hz, while the relation is reversed for frequencies higher than about 4-5 Hz.

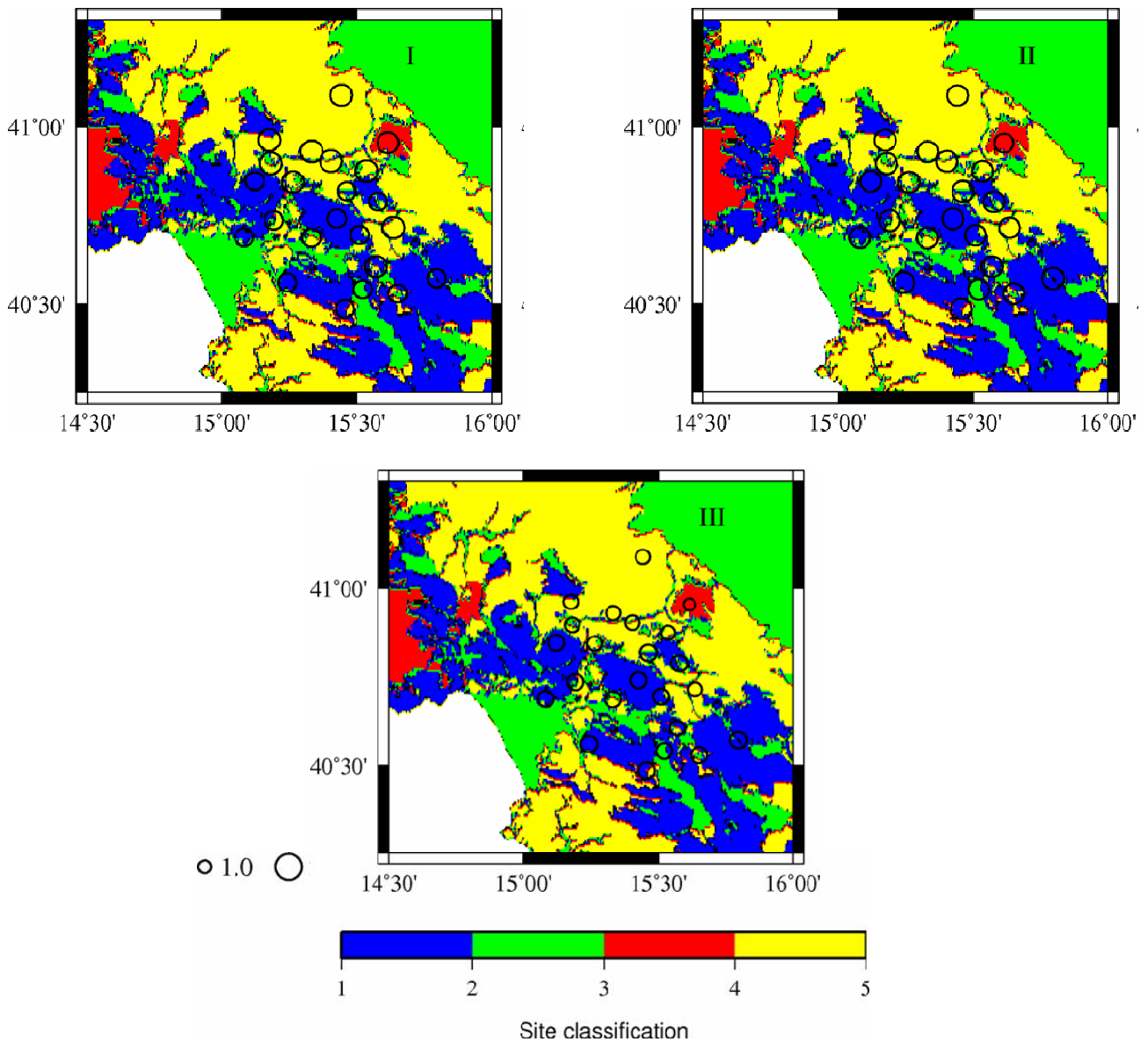


Figure 5.7. Average spectral amplifications computed for three frequency bands, are displayed over the QVTM site conditions map. Circles are centered on strong-motion sites, with diameter proportional to the average amplification.

These maps represent a first attempt to estimate the site amplification, based on the measured ground motions with geologically-based, frequency and amplitude-dependent site corrections.

The accuracy of these maps depends on the density of the stations and the available geologic

information. Clearly the maps are expected to improve when more data become available and more analyses are done. In particular, to further refine the maps, detailed information on alluvial units are needed in order to “split” Quaternary units according to grain size and thickness. In fact, the bigger classification problems are with sites that have a thin layer of alluvium over an higher velocity material at shallow depth.

The site-response factors were also compared with those obtained from past earthquakes in the Los Angeles urban area, and were found to be in reasonably good agreement in the frequency bands for Mesozoic hard rock and Tertiary sediments and soft rock.

Table 3 presents the site amplification factors proposed by Harmsen (1997b) for the Mesozoic (Mz), Tertiary (Ts), and Quaternary (Qoa and Qya) categories.

Table 4 shows those estimated by Borchardt (1994) for the QTM categories at periods of both 0.3 and 1.0 seconds for each of four input ground acceleration levels. Note that at 0.3 sec, amplification for the soil sites (Quaternary) is nearly a factor of 1.5 at low input motions and it decreases to slightly over 1.0 for strong motions; Tertiary and Mesozoic rock units have a less pronounced amplitude dependency (Wald et al., 1999).

Logarithmic means and standard deviations (base 10) of site amplification grouped by surficial geology category.

GEOL Indicator	IFB 0.5- 1.5			HFB 2.0- 6.0		
	Mean	S.D. (10)	N	Mean	S.D. (10)	N
Mz	1.217	0.113	7	1.216	0.156	7
Qoa	2.737	0.097	61	1.838	0.157	61
Qya	2.796	0.173	105	2.185	0.175	105
Ts	2.097	0.182	27	1.967	0.182	27

Mz, Mesozoic rock; Qoa, Pleistocene alluvium; Qya, Holocene alluvium; and Ts, Tertiary sedimentary and volcanic rock. *N* is sample size. Values are relative to 1.0 at PSL.

Table 3. Logarithmic means and standard deviations (base 10) of site amplification grouped by superficial geology category (Harmsen (1997)).

Period (sec)	Input Rock Peak Ground Acceleration (gals)			
	<50 gals	50-100 gals	100-200 gals	>200 gals
Mesozoic:				
0.3	1.00	1.00	1.00	1.00
1.0	1.00	1.00	1.00	1.00
Tertiary:				
0.3	1.14	1.10	1.04	0.98
1.0	1.27	1.25	1.22	1.18
Quaternary:				
0.3	1.39	1.15	1.06	0.97
1.0	1.45	1.41	1.35	1.29

Table 4. Site amplification factors proposed by Borchardt (1994).

The comparison of the average site amplification levels with estimates from the other studies, suggests that these factors can be applied as corrections to attenuation relationships for use in seismic hazard calculations for the Campania-Lucania region at least for the Mesozoic and Tertiary site classes.

6.

H/V spectral ratio of earthquake data

6.1. Introduction

In order to compare site-response estimates obtained from different spectral-ratio techniques that do not rely on a reference site, the horizontal-to-vertical (H/V) method has been applied to earthquake recordings.

The procedure was introduced by Nogoshi and Igarashi in 1970, but Nakamura (1989) made it popular. Originally, it was proposed for analyzing ambient seismic noise recordings. Recently, Lermo and Chavez-Garcia (1993) applied this technique to the S-wave part of earthquake recordings. The method, which is analogous to the so called receiver-function technique used to determine the crustal and upper mantle structures from teleseismic records (Langston, 1979), assumes that the vertical component of ground motion contains more information on the source than the horizontal components.

This thesis presents the estimated site effects for the ISNet stations, obtained applying this technique to the same earthquake recordings employed in the inversion method.

The site responses obtained with those two techniques were found to be similar in shape. Both methods were consistent in estimating the fundamental resonance frequency, even if the levels of amplification were very different. In particular, at frequencies lower than the fundamental one, the H/V ratios showed a higher level of amplification than the inversion results. Nevertheless, both methods have revealed the frequency dependence of site response at the Campania-Lucania region. These results are promising for site-specific-assessments in areas that lack reference sites.

6.2. The technique

The technique used in this study was originally introduced by Nakamura (1989) to interpret microtremor recordings. Recently, Lermo et al., (1993) proposed that the site response can be estimated by dividing the horizontal-to vertical component ratios of the shear-wave spectra at each site, rather than dividing by the reference site spectra. They presented some arguments to explain why the method, conceived to analyze Rayleigh waves in microtremor records, could also work for the S-wave part of seismograms. In this framework, they applied the method to earthquake data obtained at various sediments sites in Mexico City, and found that the frequency and amplitude of

the fundamental resonant peak could be identified. Moreover, several studies have shown that the vertical component of ground motion had the same features and similar amplitudes regardless of the type of soil at the station: clay layer, or hard rock (Campillo et al., 1989). It appears then that the vertical component of shear waves, composed primarily of S- to P-wave conversions (Takahashi et al., 1992), is not influenced by the local structures, whereas the radial component contains P- to S-wave conversions from structural discontinuities below the recording site. Therefore, an estimate of the impulse response function could be obtained by deconvolving, or dividing in the frequency domain, the vertical component from the radial component.

6.3. Comparison of different site response estimation techniques.

The same data and processing used in the inversion approach have been used in the study. From each recording a window of 5 seconds, including the intense part of the S-wave, was selected. The windows of every station were first corrected to zero baseline, then cosine tapered (5%), and Fourier transformed. The spectral amplitudes were smoothed using an arithmetic smoothing algorithm to each data point. The size of the window is defined by specifying its halfwidth of 5 points. The east-west and north-south components were combined in the Fourier domain to obtain a single horizontal component, and used to compute spectral ratios relative to the vertical component. Figures 6.1 (a, b, c, d, e, f, g, h, i, j, k, l, m, n, o, p, q, r, s, t, u, v, w) show the similarities and differences between the site responses estimated by the H/V method (blue line) and those estimated by the inversion technique (red line). The vertical black lines represent standard deviations.

From the figures it can be noted that the estimated spectral ratios are similar in shape. Both methods are consistent in estimating the fundamental resonance frequency for the investigated site, even if a shift in frequency is often observed. The level of amplification from the H/V method is highly variable, and is always higher than that obtained by the inversion technique, especially at frequencies lower than the fundamental one. These differences could be due to the influence of the incidence angle as well as to the amplification of the vertical component (Lermo and Chavez-Garcia, 1993, Parolai et al., 2004). Therefore, small incident angles yield larger amplifications in the H/V curves than in the inversion curves, because of the small amplification of the vertical component that influences both the S- and P-wave part of the seismograms.

A reduction of the H/V amplitude due to the amplification of the vertical component only occurs at high frequencies. This is consistent with the hypothesis that the S- to- P conversion at the bedrock/soil layer contact results in amplification of the vertical component in the S-wave window and deamplification in the resulting H/V ratio. Instead, the P- to- S conversion provides energy to

the horizontal component in the P window, allowing the H/V ratio to give information about S-wave resonance, regardless of the signal window used. However, reliable H/V site responses can be obtained only when earthquakes are distributed around the seismic station at different distances. In fact, at larger epicentral distances, the inhomogeneous phases do affect both the H/V and the inversion site response. Recently, Parolai and Richwalski (2004) showed that the observed differences in the site responses obtained applying different techniques, can be attributed to the contribution of pure and converted waves.

In conclusion, even if discrepancies exist between the site response estimates, the results show a good agreement on the frequency of the fundamental resonant peak.

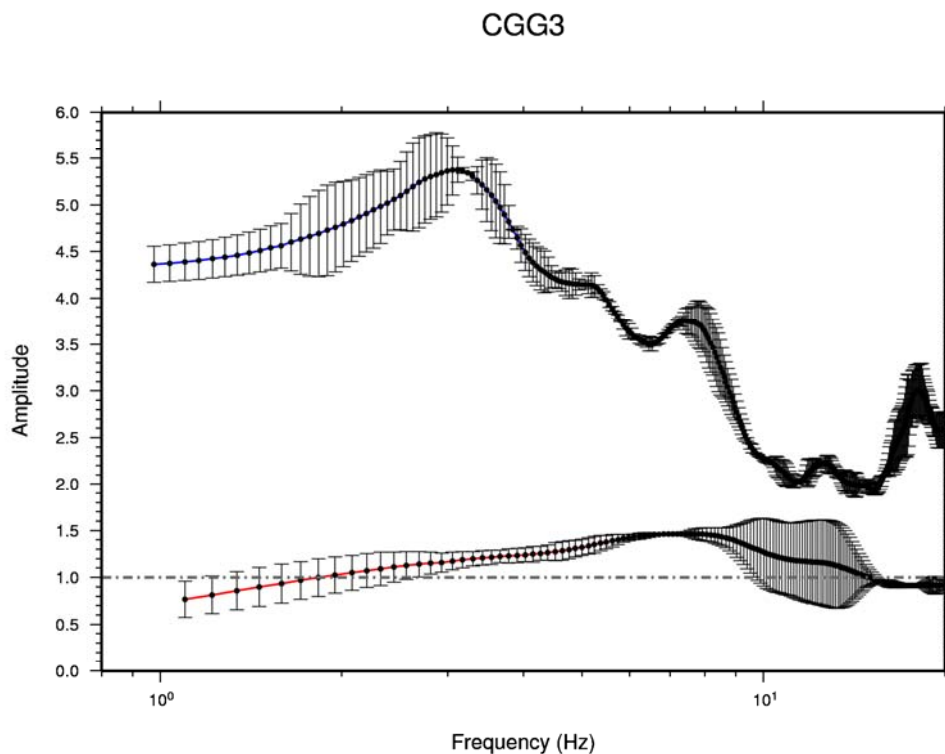


Figure 6.1 a). Similarities and differences between the estimated site responses obtained by the H/V method (blue line) and the inversion technique (red line) on earthquake recordings. The vertical black lines represent standard deviations.

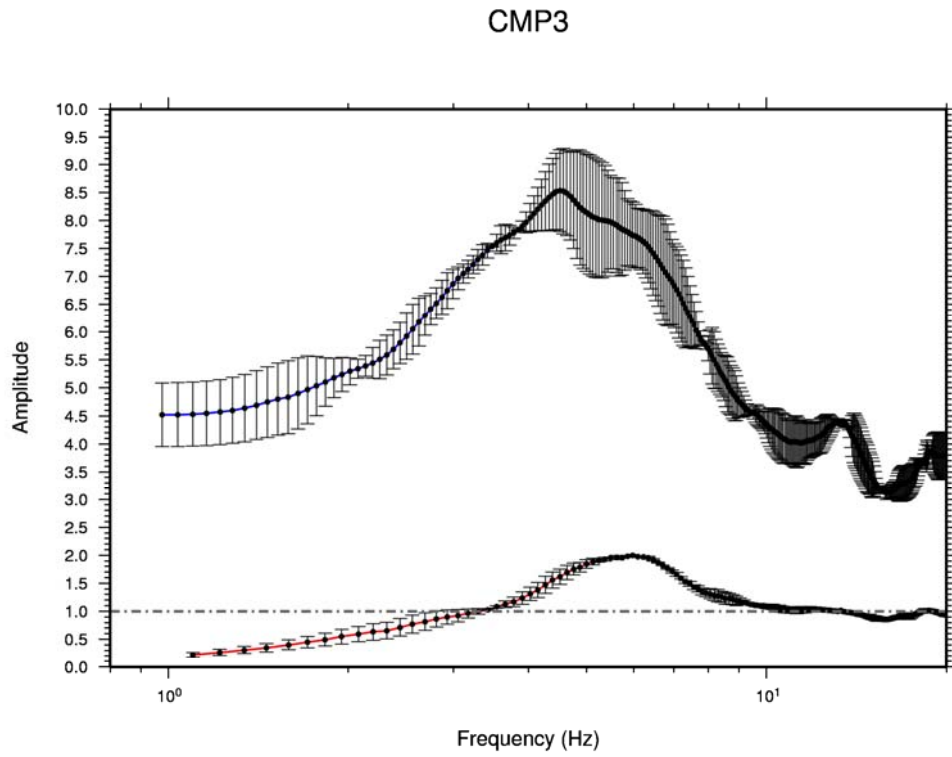


Figure 6.1 b). Same as figure 6.1a), but for station CMP3.

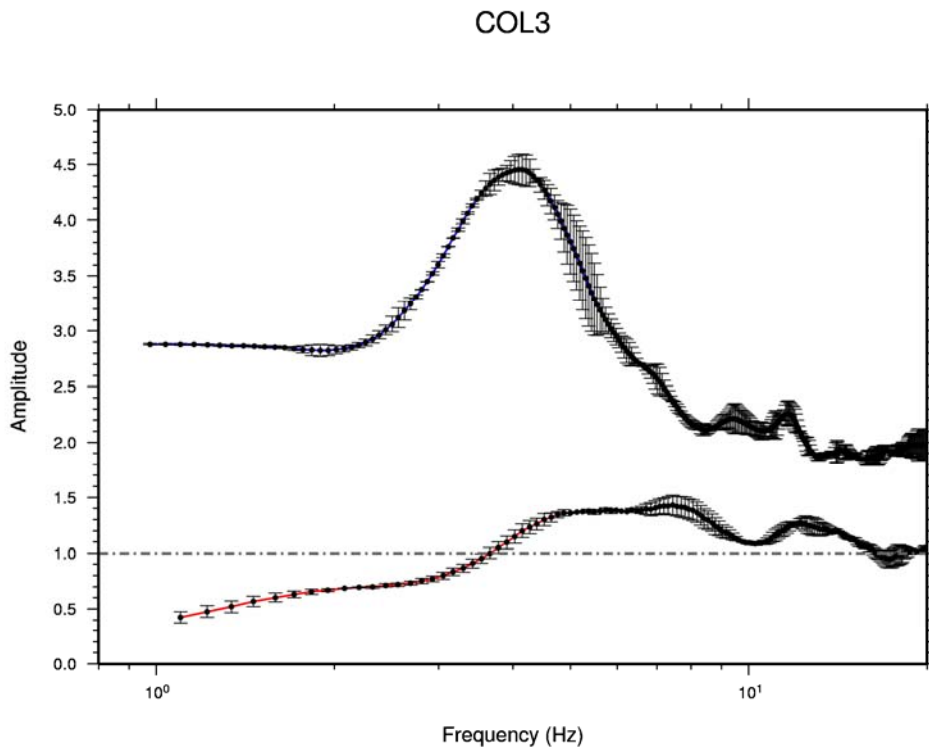


Figure 6.1 c). Same as figure 6.1a), but for station COL3.

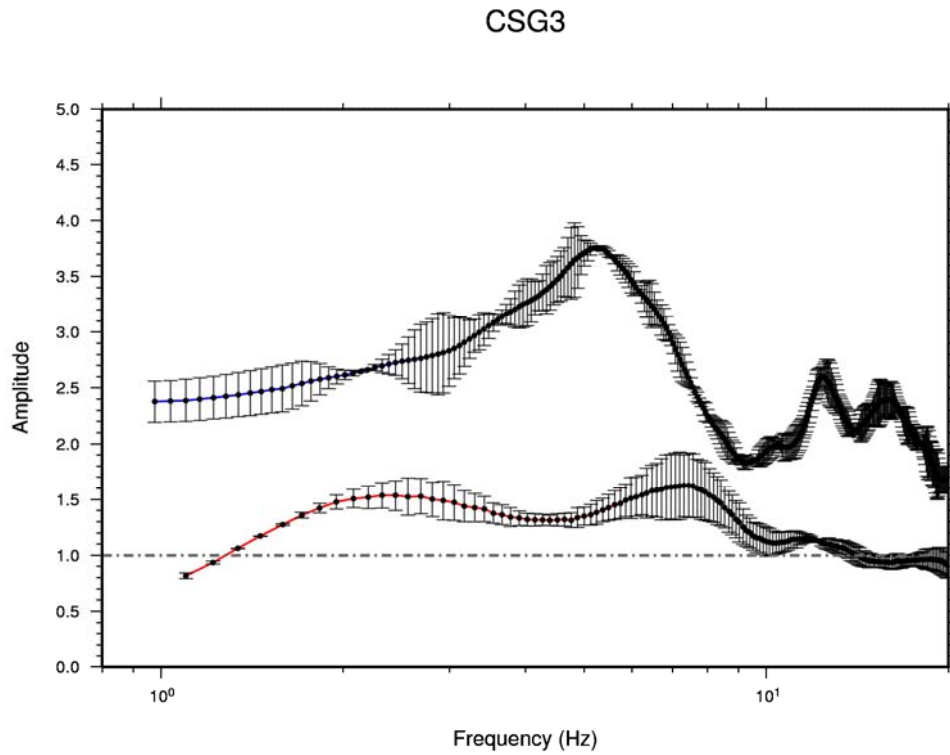


Figure 6.1 d). Same as figure 6.1a), but for station CSG3.

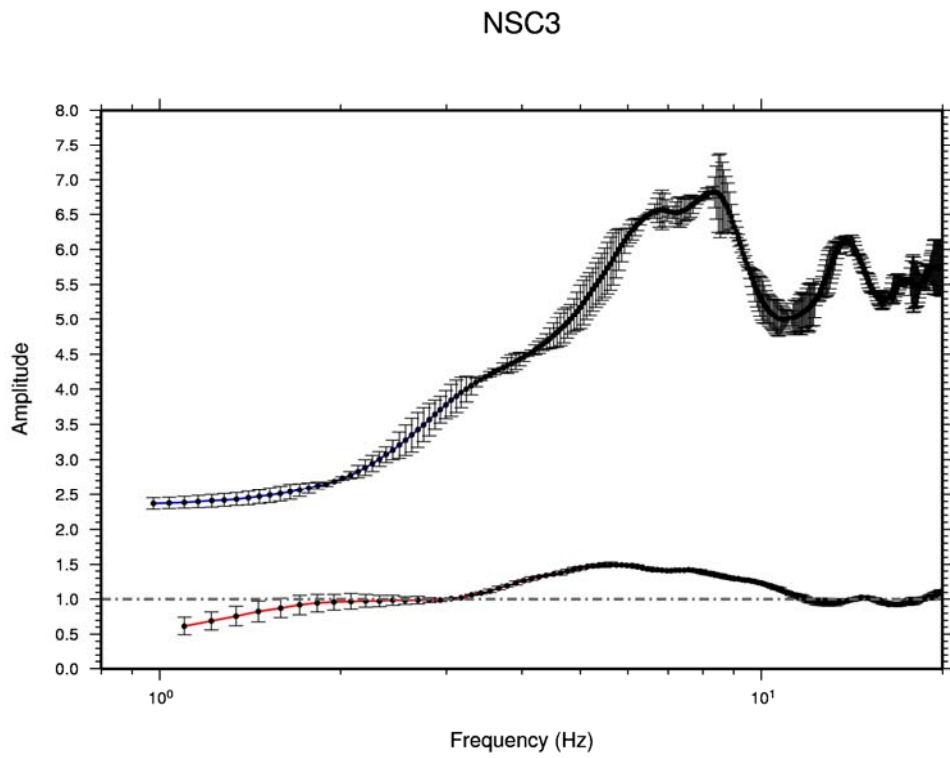


Figure 6.1 e). Same as figure 6.1a), but for station NSC3.

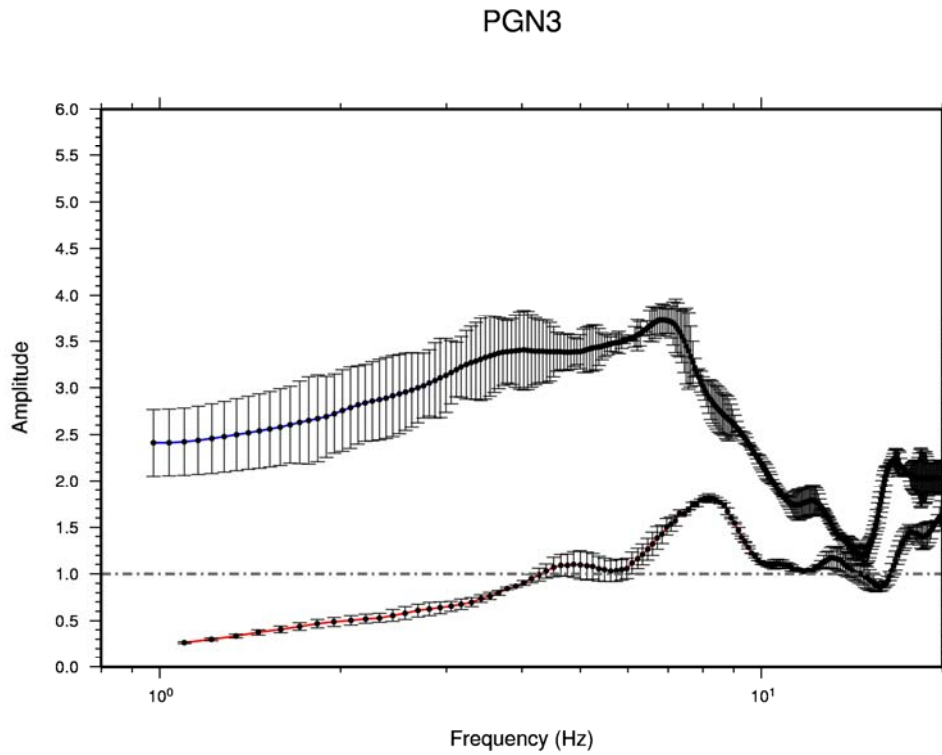


Figure 6.1 f). Same as figure 6.1a), but for station PGN3.

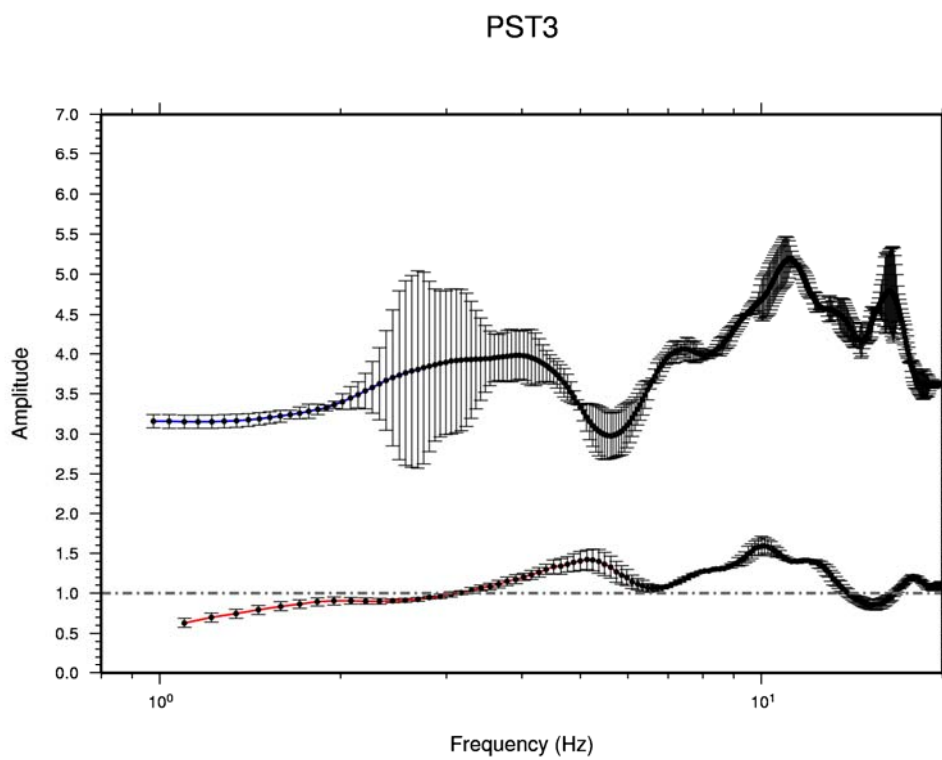


Figure 6.1 g). Same as figure 6.1a), but for station PST3.

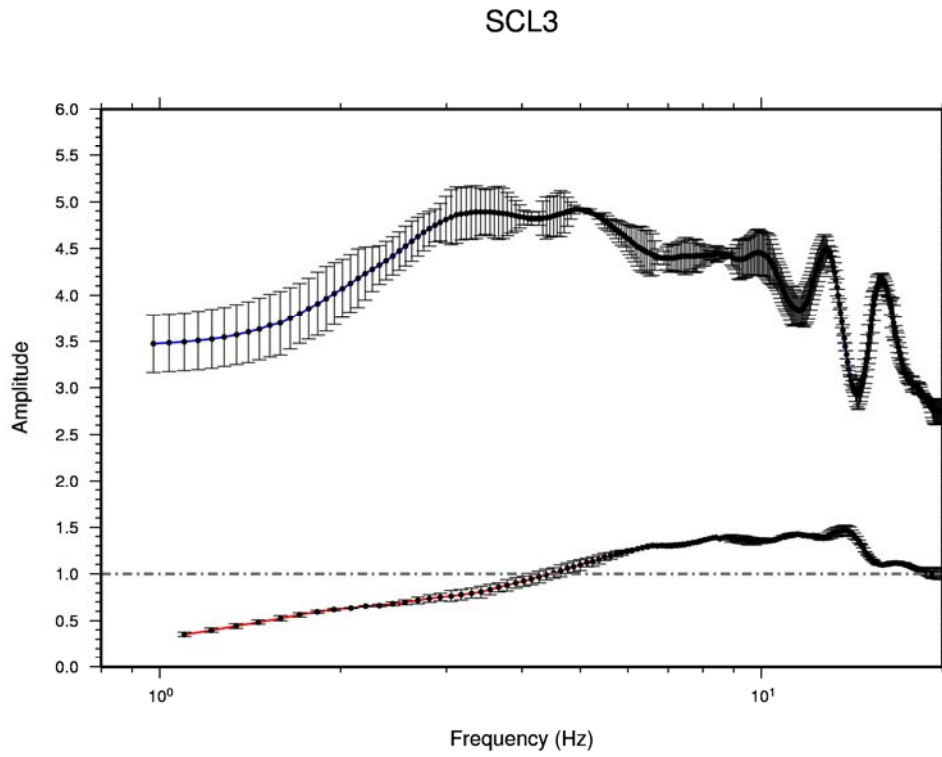


Figure 6.1 h). Same as figure 6.1a), but for station SCL3.

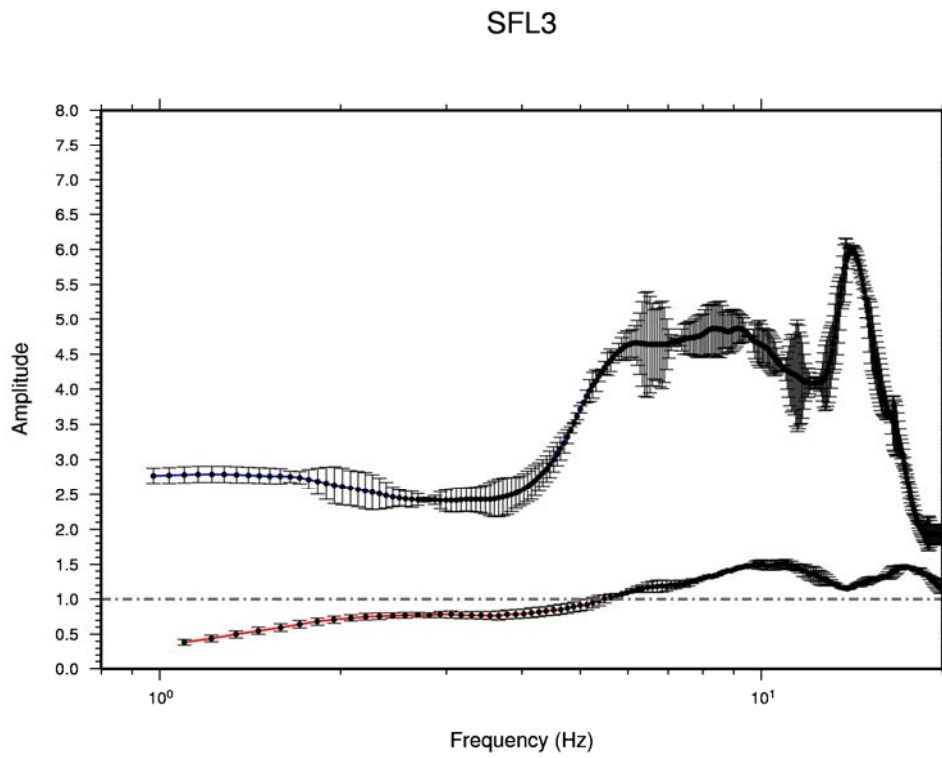


Figure 6.1 i). Same as figure 6.1a), but for station SFL3.

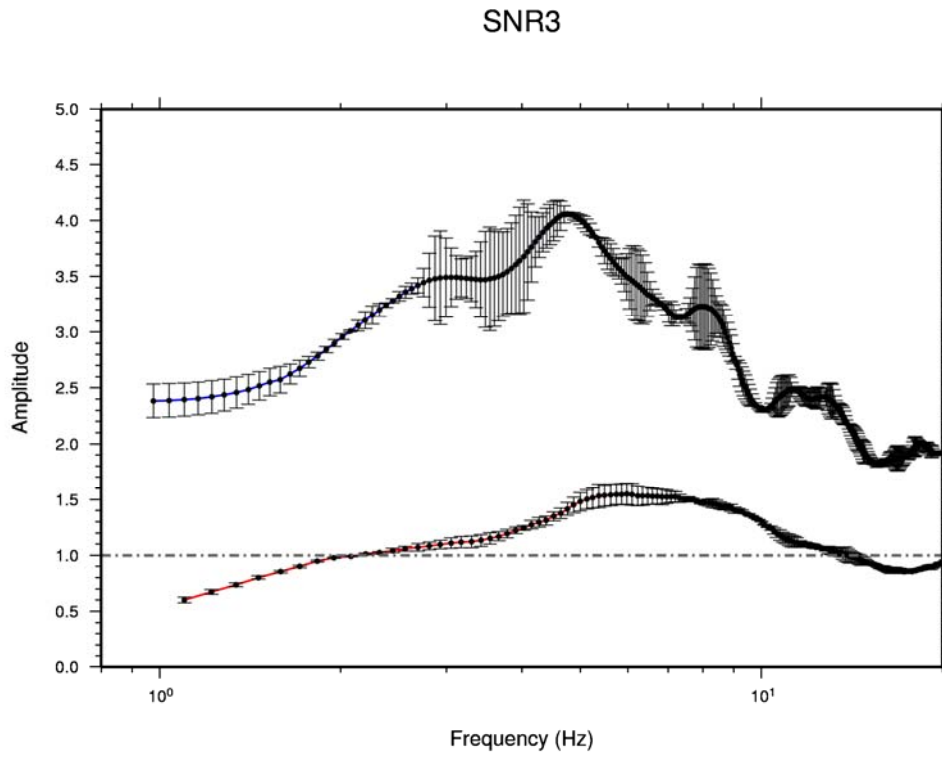


Figure 6.1 j). Same as figure 6.1a), but for station SNR3.

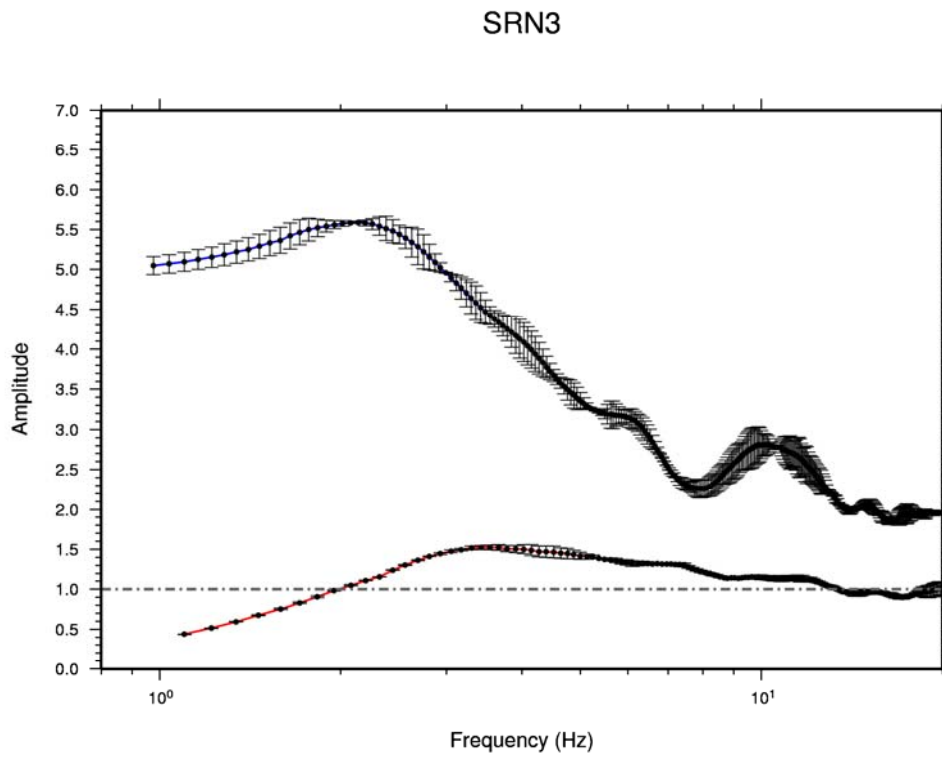


Figure 6.1 k). Same as figure 6.1a), but for station SRN3.

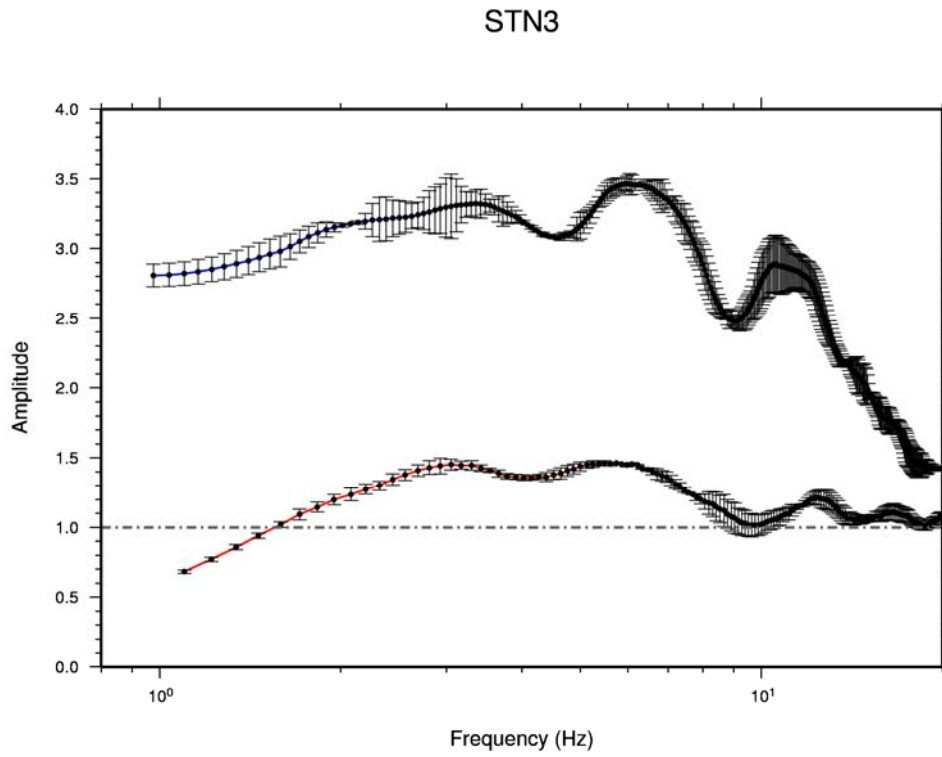


Figure 6.1 l). Same as figure 6.1a), but for station STN3.

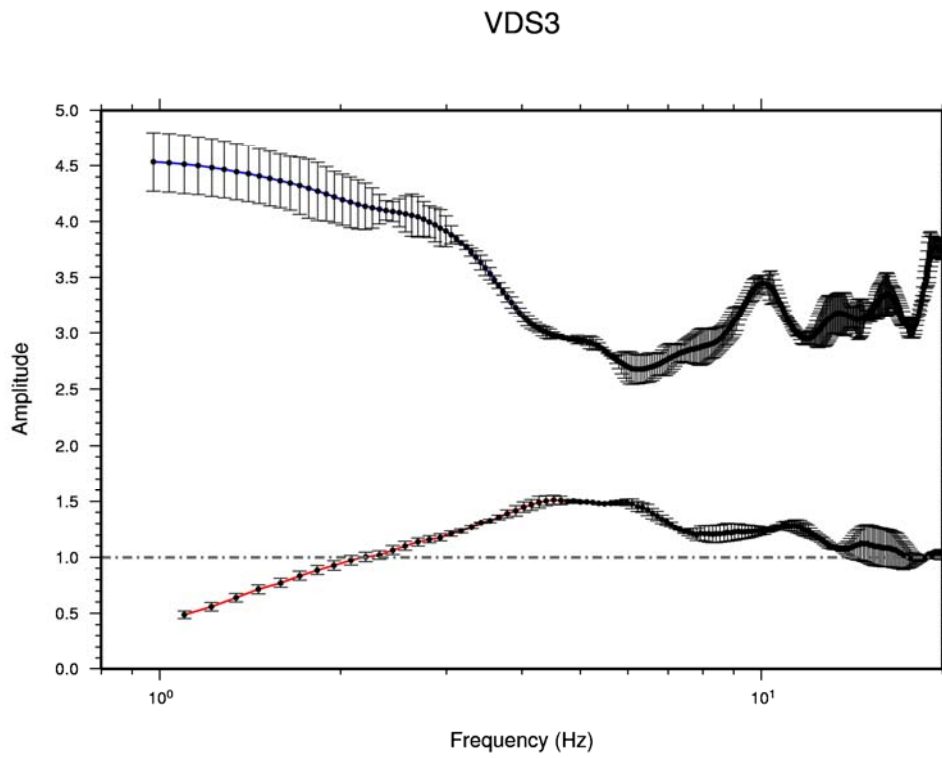


Figure 6.1 m). Same as figure 6.1a), but for station VDS3.

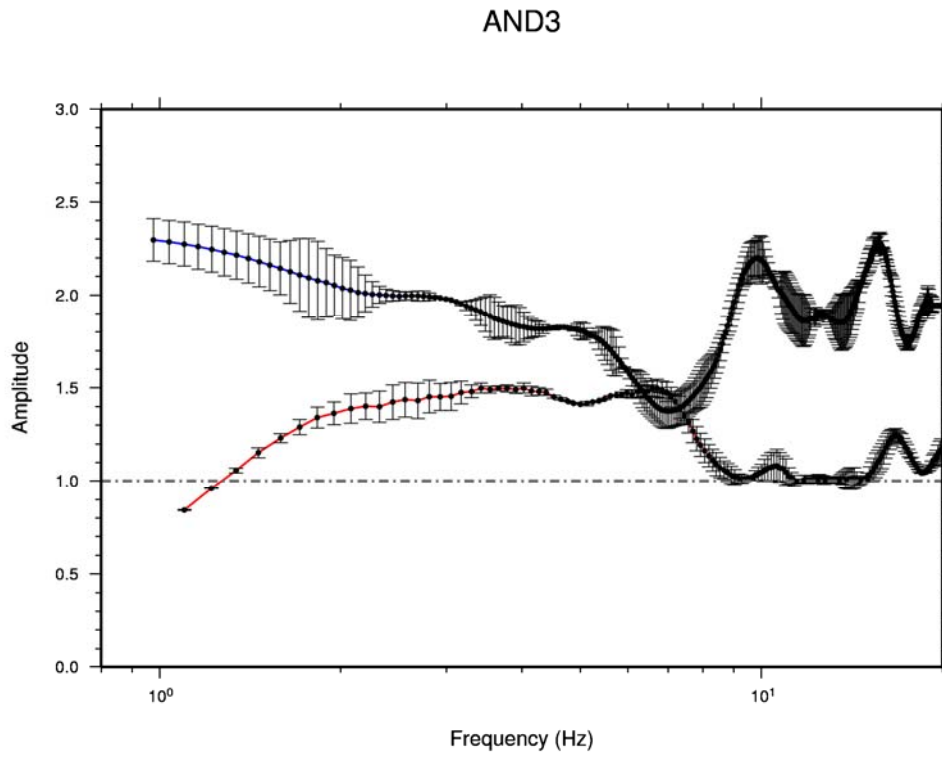


Figure 6.1 n). Same as figure 6.1a), but for station AND3.

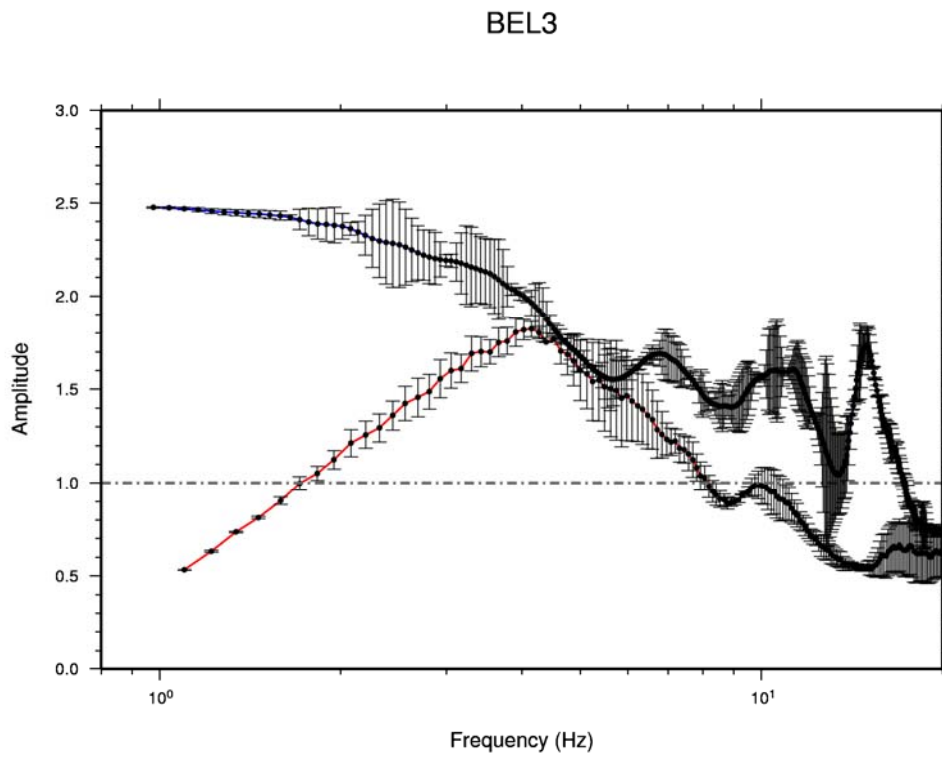


Figure 6.1 o). Same as figure 6.1a), but for station BEL3.

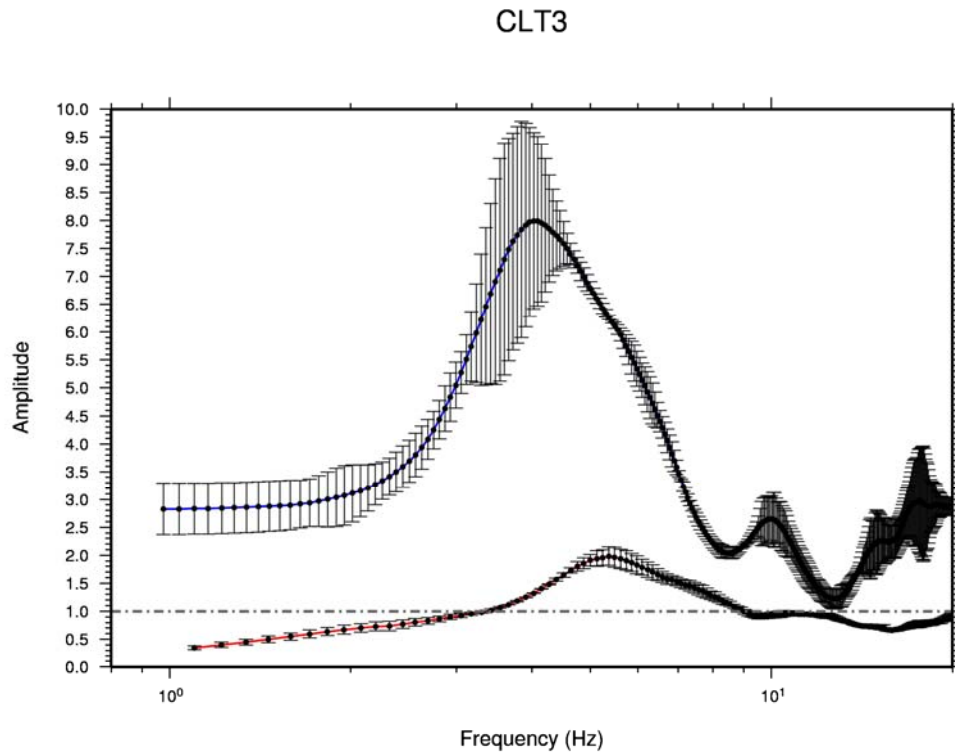


Figure 6.1 p). Same as figure 6.1a), but for station CLT3.

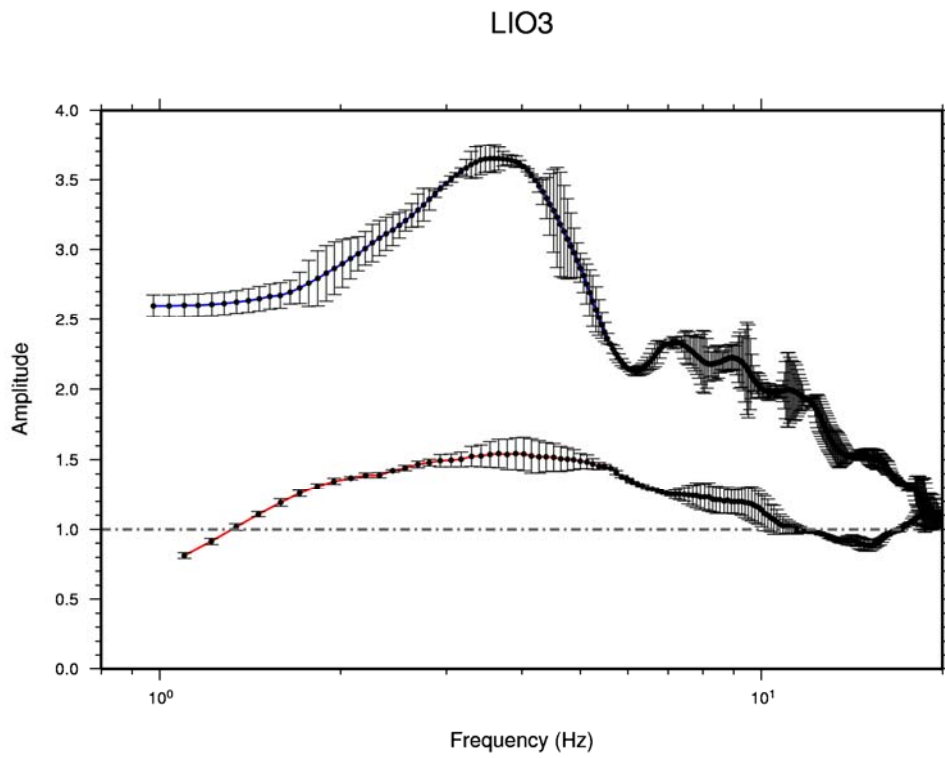


Figure 6.1 q). Same as figure 6.1a), but for station LIO3.

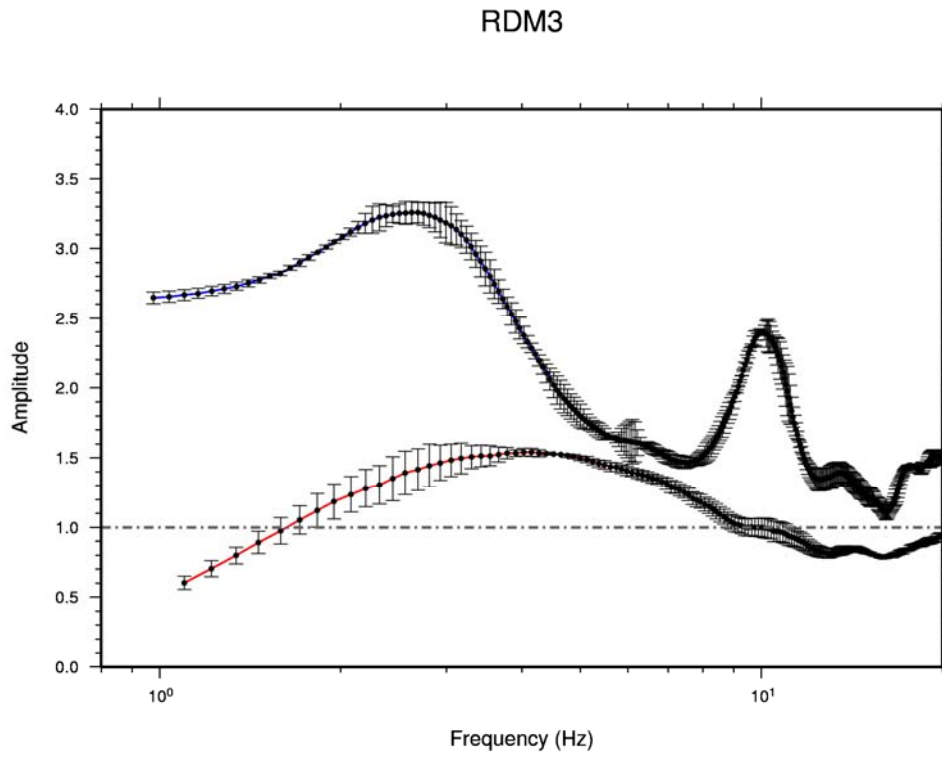


Figure 6.1 r). Same as figure 6.1a), but for station RDM3.

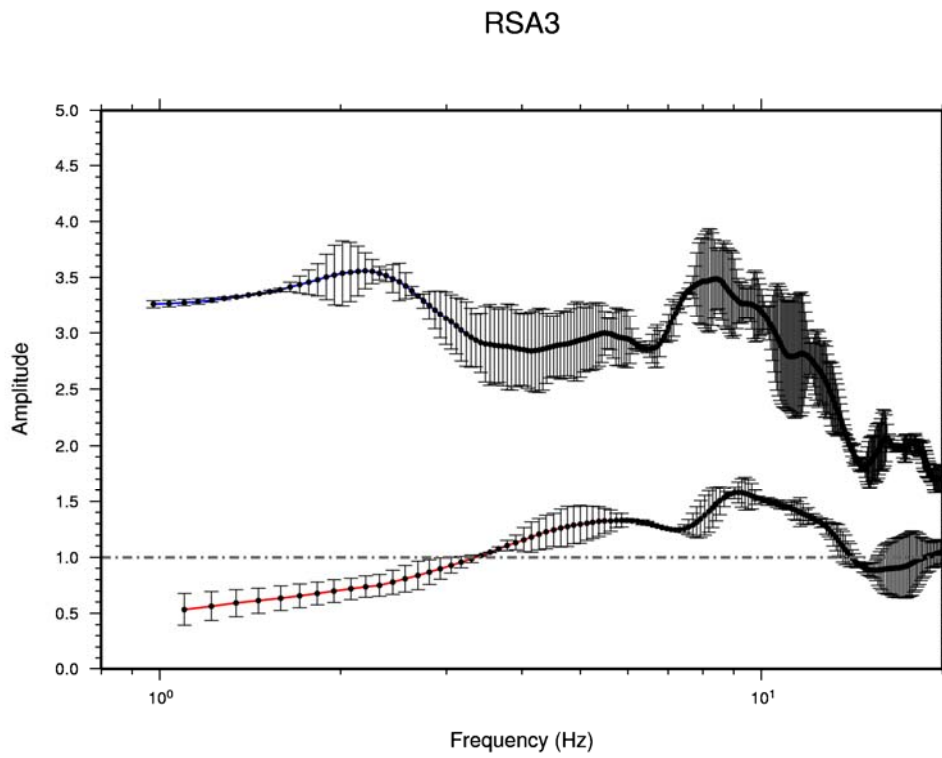


Figure 6.1 s). Same as figure 6.1a), but for station RSA3.

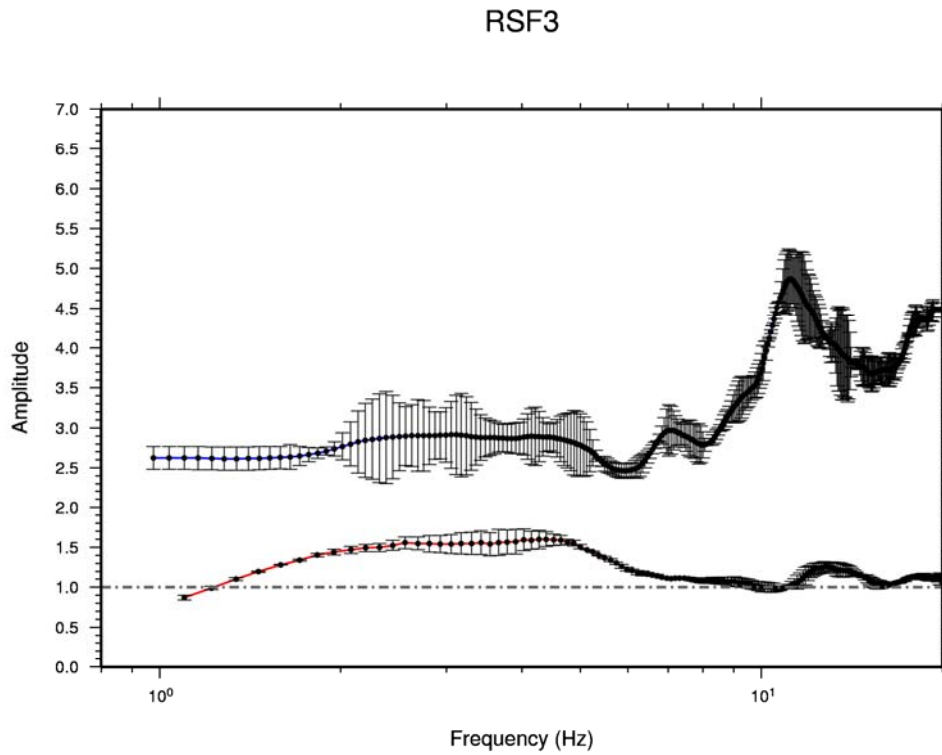


Figure 6.1 t). Same as figure 6.1a), but for station RSF3.

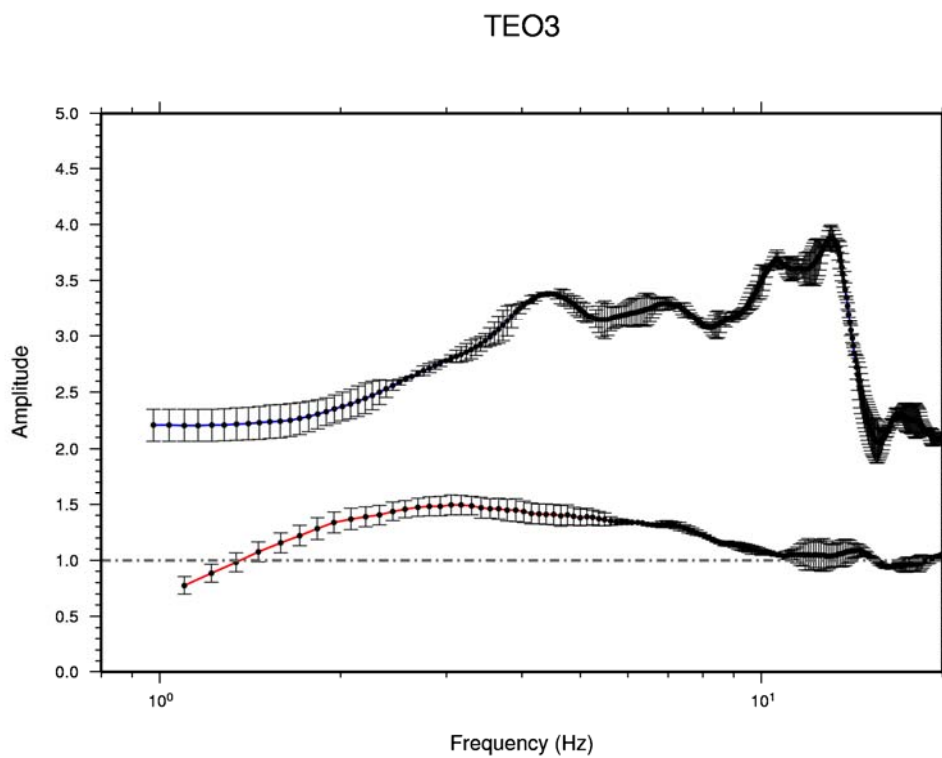


Figure 6.1 u). Same as figure 6.1a), but for station TEO3.

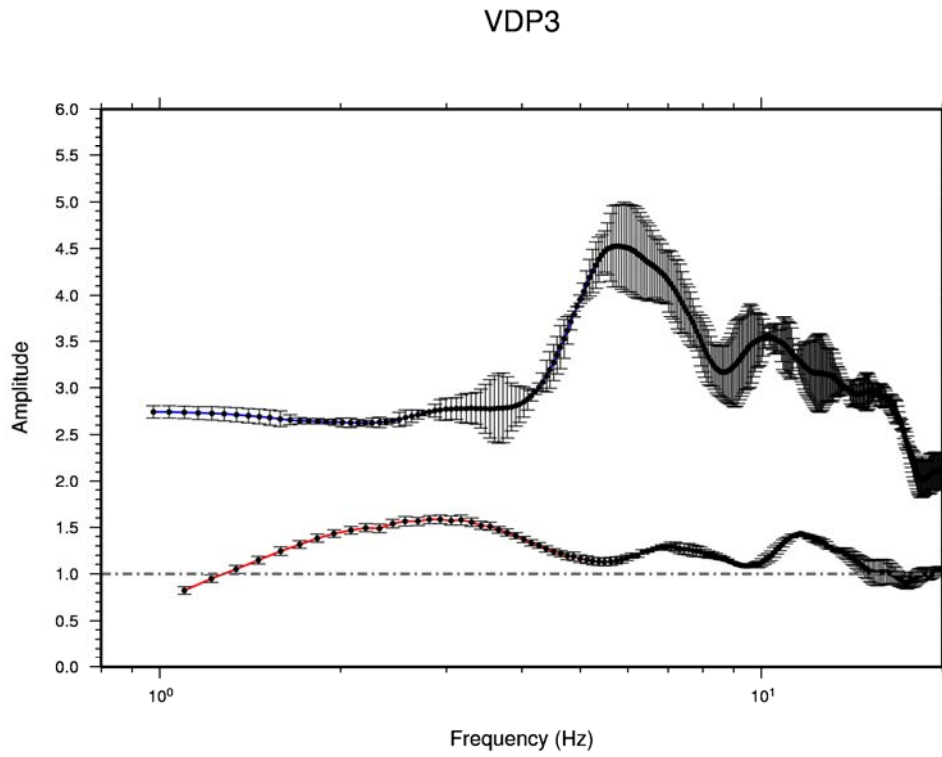


Figure 6.1 v). Same as figure 6.1a), but for station VDP3.

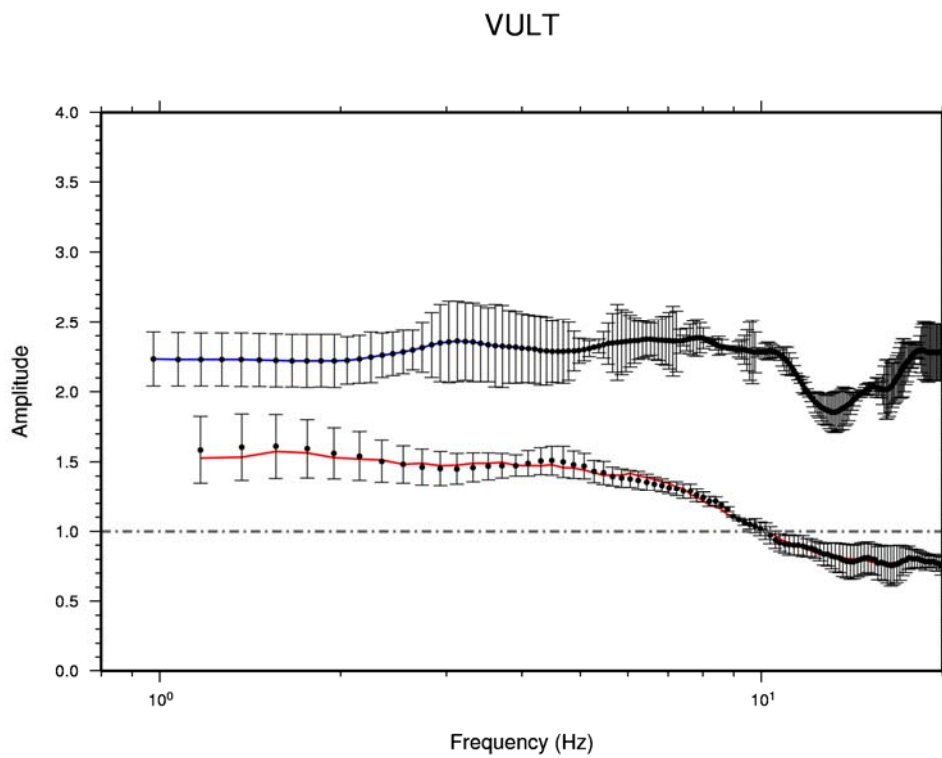


Figure 6.1 w). Same as figure 6.1a), but for station VULT.

For some seismic stations (*CLT3*, *CMP3*, *COL3* and *PST3*) it was possible to calculate the transfer functions using a simple numerical modeling based on Thompson-Haskell propagator matrix method. In this method the ratios of the vertical and horizontal motions at the surface to the total amplitude of the plane wave incident in the bottom layer, were obtained. These ratios are complex functions involving the frequency, the angle of incidence, and the thicknesses, velocities (P and S waves), quality factors, and densities of the layered crustal model.

The velocity models were built by matching position and surface geology with P-, S-velocity and density profiles obtained from the database of the National Strong Motion Network (RAN) (*Working Group ITACA (2008) - Data Base of the Italian strong motion data: <http://itaca.mi.ingv.it>*).

Figure 6.2 shows the transfer functions of the horizontal motion relative to the horizontal amplitude of incident motion for the plane layer model built for a generic site. Excitation is given by plane SH waves with four different incidence angles relative to the vertical. As expected, for small incidence angles, the amplitude is very high (for vertical incidence it would be infinite). For this region, incidence angle of 45° was imposed in the calculate of transfer functions.

The main advantage of this method is that in the cases where there are many layers, each will contribute with multiples or converted waves to the time range of interest.

Figures 6.3 (a,b,c,d, e) show the response functions estimated by using different methods. The blue curve represents the spectral ratio obtained from the H/V method, the red curve represents the spectral ratio obtained from the inversion method and the green curve represents the transfer function computed by the Thompson-Haskell propagator matrix method.

From the figures it can be noted that the obtained spectral ratios from the H/V method and those obtained from the Thompson-Haskell propagator matrix method, are similar in shape. These last ones showed a shift in frequency relative to the frequency peaks present in the inversion curves. However, both methods were consistent in estimating the fundamental resonance frequency, even if the level of amplification was very different. In particular, the level of amplification from the H/V method was always higher than that obtained by the others technique at frequencies lower than the fundamental on.

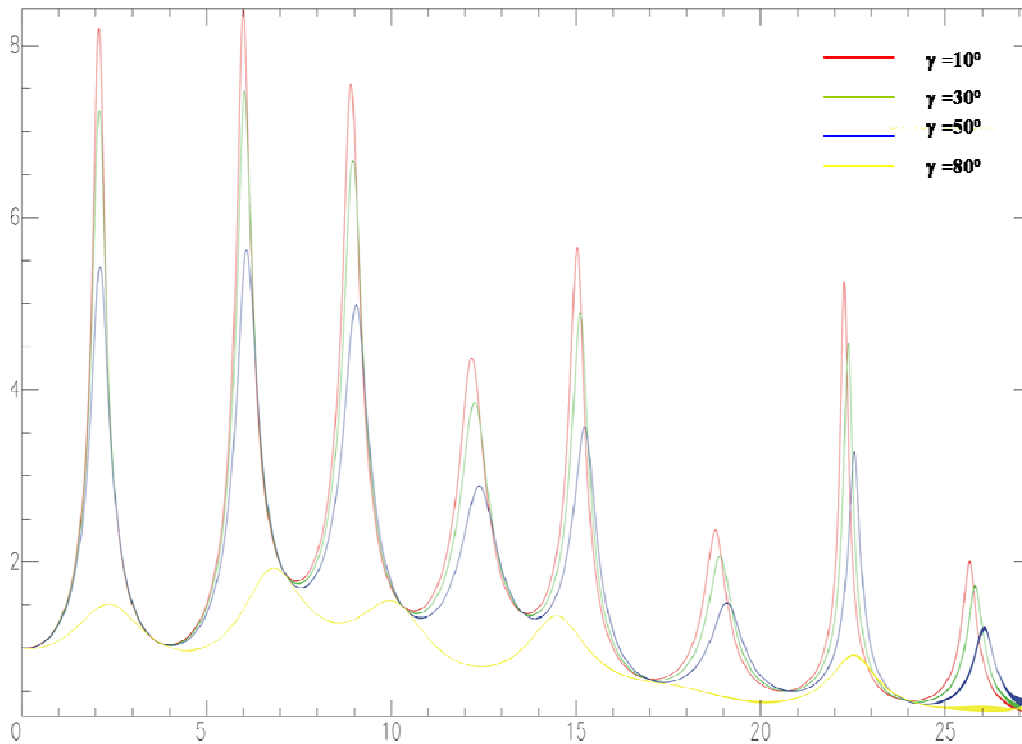


Figure 6.2. Transfer functions of horizontal motion. Excitation is given by plane SV waves with four different incidence angle relative to the vertical.

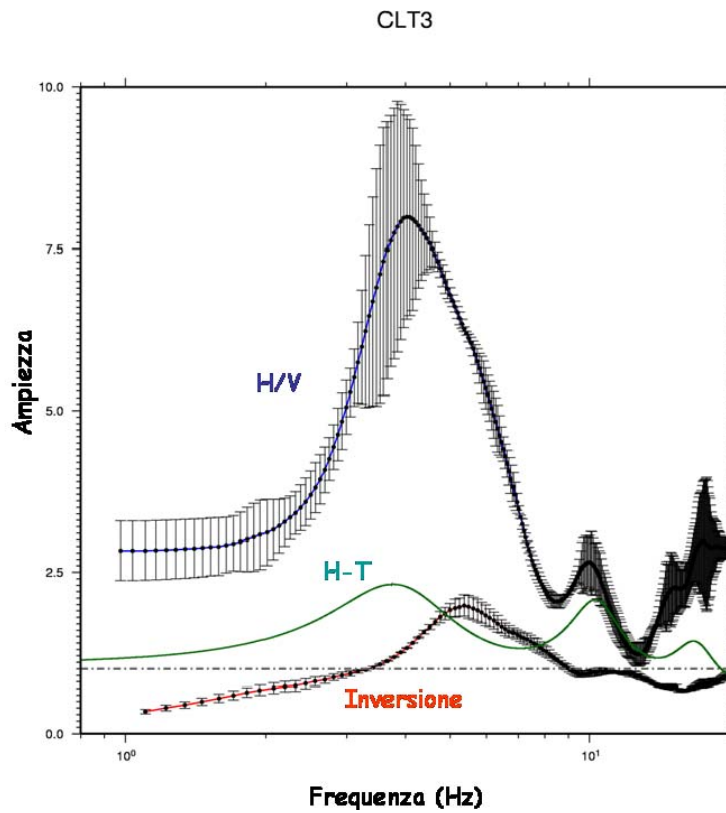


Figure 6.3 a). Response functions estimated by using different methods. The blue curve represents the spectral ratio obtained by the H/V method, the red curve represents the spectral ratio obtained by the inversion method and the green curve represents the transfer function computed by Thompson-Haskell propagator matrix method.

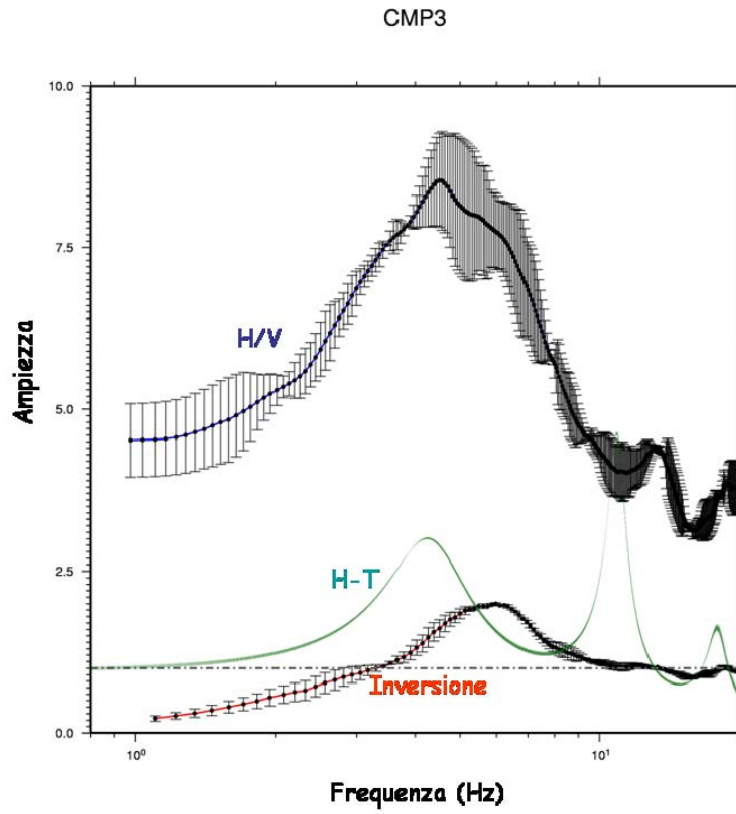


Figure 6.3 b). Same as figure 6.3 a), but for station CMP3.

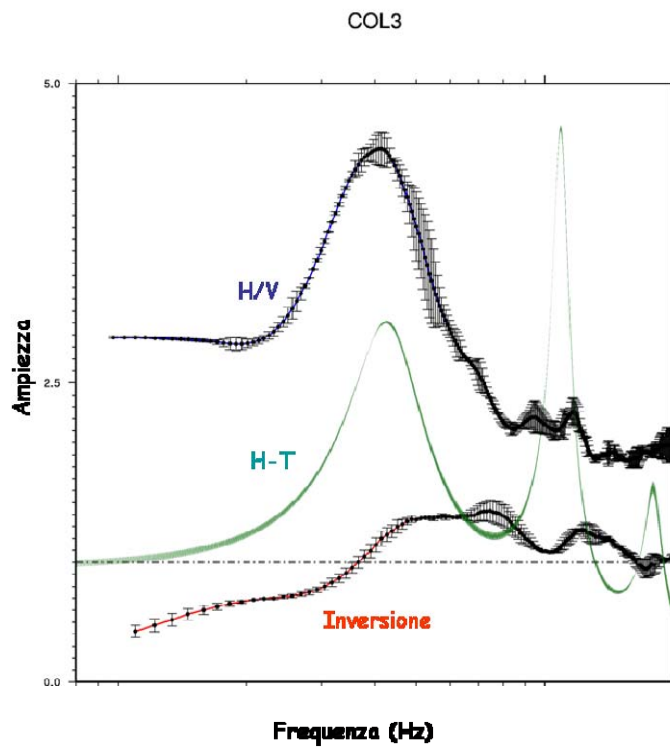


Figure 6.3 c). Same as figure 6.3 a), but for station COL3.

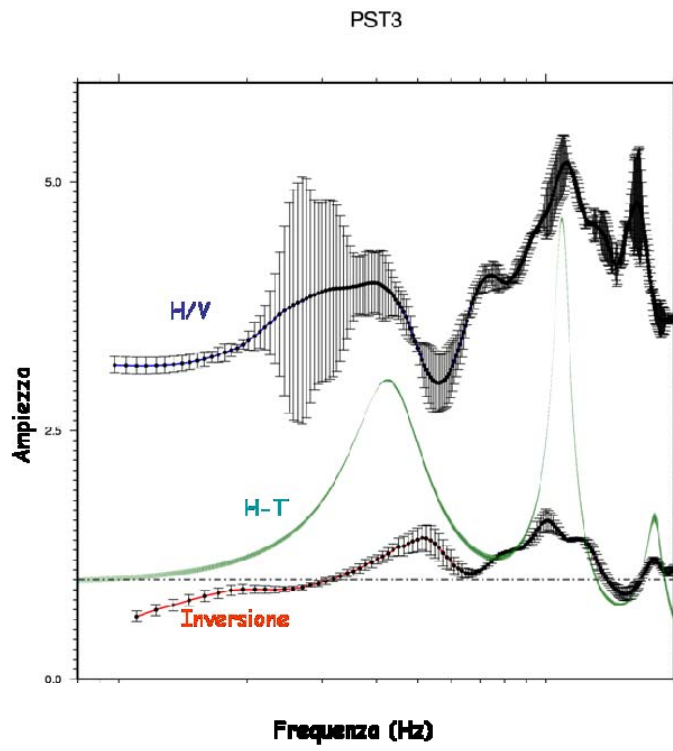


Figure 6.3 d). Same as figure 6.3 a), but for station PST3.

Conclusions

Site responses at stations of the ISNet network were estimated using different techniques. First, the available information of the local geology have been used to create some generalized sites classes, according to the European norm, Eurocode8 (EC8). The approach and geologic categories described in this thesis, result in a map, the QVTM site conditions map, that yields site conditions information for some units of the Campania-Lucania region.

Obviously the accuracy of this site conditions map is limited by the amount available data. Clearly the map is expected to improve when more shear-wave velocity measurements and more analyses will be done. In particular, to further refine the map, detailed information on Quaternary and Volcanic units are needed in order to highlight significant variations in site response for mapped young sediments. However, the statewide the site classification map may provide a basis as is or in conjunction with other factors, for more precise characterisations of the site conditions in probabilistic seismic hazard calculations.

In the present thesis, time-domain simulations were used to identify possible site effects at the seismic stations of the ISNet network, by comparing the observed and simulated peak ground motion parameters at a generic rock or a generic soil site. The predicted data were obtained both by using a attenuation relationship and without a attenuation relationship. The residual values measured at each station have provided a first-order measure of the site effect. The data have showed that the material properties near the surface in the Campania-Lucania region, can produce large modifications of the selected peak ground-motion parameters. In particular, the common assumption that the surface-rock site record represents the input motion at the base of the soil layers does not seem to hold in the case of the Mesozoic seismic stations. The observed relative amplification at rock sites in all the frequency bands, on the one hand may be due to a topographic effect, since many rock sites are located on mountains or hills, and on the other hand it may be caused by the weathered and fractured nature of near-surface materials.

These results have suggested that techniques not requiring a reference site could provide more reliable estimates of the site effects at the ISNet stations. Therefore, the site responses were computed using two non-reference site methods: the non-linear inverse procedure based on the Simplex algorithm and the horizontal-to-vertical (H/V) method.

In most of cases, the two techniques have provided site responses with similar shapes. Both methods were consistent in estimating the fundamental resonance frequency, even if the levels of amplification were very different. Several studies explain these significant differences as due to the contribution of pure and converted waves to the site response.

The site response factors, determined by averaging the site-amplification spectra obtained through the inversion method, were correlated with the local geology. Significantly different site-response factors were found for Tertiary and Mesozoic units. In general, the Tertiary units showed higher amplification than rock sites for frequency lower than about 4-5 Hz. Moreover, a good correlation between larger site response factors and lower average shear-wave velocity in the upper 30 m, has been found. The general similarity in these results with other studies suggest that the site amplification factors provide a useful correction for local amplification and can be incorporated into a rapid generation of peak ground motion maps to estimate the ground shaking over the region analyzed.

These conclusions are based on three important assumption. First, the limitation to the observation data, assuming that 106 seismic events used are representative of what we can expect from future earthquakes in the Campania-Lucania region. Second, the accuracy of the site-response maps presented in this thesis depend on the large map scale, on the available geologic information, and on the available ground-motion data. Third, the limitation to observations from the Campania-Lucania region, affects the results for the Quaternary and Volcanic class due to lack of data for these sites.

In conclusion, the study presented in the thesis should be seen as guide for future investigations. Analyses using larger data sets of strong-motion observations and of shear-wave velocity measurements, are expected. Studies based on other significant factors, such as topography effects and other effects of shallow structures, are recommended. Moreover, numerical modelling to explain the differences in the results obtained using different techniques, should also be considered.

References

- Aki, K. (1988). Local site effects on strong ground motion. *Proc. Earthquake Eng. Soil Dyn. II*, 103-155.
- Aki, K., and P. G. Richards (2002). *Quantitative Seismology. Second Ed., University Science Books, Sausalito, California, 700 pp.*
- Akinci, A., L. Malagnini, R. B. Herrmann, N. A. Pino, L. Scognamiglio, and H. Eyidogan, (2001). High-frequency ground motion in the Erzincan region, Turkey: Inferences from small earthquakes. *Bull. Seism. Soc. Am.*, **91**, 1446–1455.
- Anderson, J. G. and S. E. Hough, (1984). A Model for the Shape of the Fourier Amplitude Spectrum of Acceleration at High Frequencies. *Bull. Seism. Soc. Am.*, **74**, 1969–1993.
- Anderson, H. J., J. Jackson (1987). Active tectonics of the Adriatic region. *J. R. Astron. Soc.*, **91**, 937-987.
- Anderson, J. G. and Y. Lei (1994). Nonparametric description of peak acceleration as a function of magnitude, distance, and site in Guerrero, Mexico. *Bull. Seism. Soc. Am.*, **84**, 1003–1017.
- Andrews, D. J. (1986). Objective determination of source parameters and similarity of earthquakes of different size. *Geophysical Monographs* 37, **6**, 259-267.
- Archuleta, R. J., and J. H. Steidl (1998). ESG studies in the United States: results from borehole arrays in *The Effects of Surface Geology on Seismic Motion*, K. Irikura, K. Kudo, H. Okada, and T. Sasatani (editors) Vol. **1**, BAKLEMA, Rotterdam, 3-14.
- Bard, P.-Y., and M. Bouchon (1985). The two-dimensional resonance of sediment-filled valleys. *Bull. Seism. Soc. Am.*, **75**, 519-541.
- Bard, P.-Y., and J. C. Gariel (1986). The seismic response of two-dimensional sedimentary deposits with large vertical velocity gradients. *Bull. Seism. Soc. Am.*, **76**, 343-356.

- Bard, P.-Y., M. Campillo, F. J. Chavez-Garcia and F. J. Sanchez-Sesma (1988). A theoretical investigation of large- and small-scale amplification effect in the Mexico City valley. *Earthquake Spectra*, 4-3, 609-633.
- Bard, P.-Y., A. –M. Duval, B. Lebrun, C. Lachet, J. Riepl and D. Hatzfeld (1997). Reliability of the H/V technique for site effects measurements: an experimental assessment. In: *Seventh International Conference on Soil Dynamics and Earthquake Engineering*, July 19-24, Istanbul, Turkey.
- Bernard, P., and A. Zollo (1989). The Irpinia (Italy) 1980 earthquake: Detailed analysis of a complex normal fault. *J. Geophys. Res.*, **94**, 1631-1648.
- Boatwright, J., L. C. Seekins, and C. S. Mueller (1991a). Ground motion amplification in the Marina. *Bull. Seism. Soc. Am.*, **81**, 1117-1131.
- Bonardi G., B. D'Argenio, and V. Perrone. Geological map of Southern Apennines– 74° Congress of the Geological Society of Italy.
- Boore, D. M. (1983). Stochastic simulation of high-frequency ground motions based on seismological models of the radiated spectra. *Bull. Seism. Soc. Am.*, **73**, 1865-1894.
- Boore D. M., and J. Boatwright (1984). Average body-wave radiation coefficients. *Bull. Seism. Soc. Am.*, **74**, 1615-1621.
- Boore, D. M., W. B. Joyner, and T. E. Fumal (1993). Estimation of response spectra and peak accelerations from Western North American earthquakes, an interim report, *U.S. Geol. Surv. Open-File Rept. 93-509*, 72.
- Boore, D. M., W. B. Joyner, and T. E. Fumal (1994). Estimation of response spectra and peak accelerations from Western North American earthquakes, an interim report, Part 2, *U.S. Geol. Surv. Open-File Rept. 94-127*, 40 pp.

- Boore, D. M., W. B. Joyner, and T. E. Fumal (1997). Equation for estimating horizontal response spectra and peak acceleration from Western North American earthquakes: a summary of recent work, *Seism. Res. Lett.*, **68**, 128-153.
- Boore D. M., and L. T. Brown (1998). Comparing shear-wave velocity in profiles from inversion of surface-wave phase velocities with downhole measurements: systematic differences between the CXW method and downhole measurements at six USC strong-motion sites. *Seism. Res. Lett.*, **69**, 222-229.
- Boore, D. M (2003). Simulation of ground motion using the stochastic method. *Pure and Appl. Geophys.*, **160**, 635-676.
- Borcherdt, R. D., M. EERI (1970). Effects of local geology on ground motion near San Francisco Bay. *Bull. Seism. Soc. Am.*, **60**, 29-61.
- Borcherdt, R. D., C. M. Wentworth, A. Janssen, T. Fumal, and J. Gibbs (1991). Methodology for predictive GIS mapping of special study zones for strong ground motion in the San Francisco Bay region, CA. *Proc. Fourth Int. Cont. on Seismic Zonation*, Earthquake Engineering Research Institute, Oakland, California, 545–552.
- Borcherdt, R. D. (1994). Estimates of site-dependent response spectra for design (Methodology and Justification). *Earthquake Spectra* **10**, 617-654.
- Boschi, E., E. Guidoboni, G. Ferrari, G. Valensise e P. Gasperini (eds) (1997). Catalogo dei Forti Terremoti in Italia dal 461 A.C. al 1990 (*ING, Roma – SGA, Bologna*), pp. 644, con database su CD-ROM.
- Brambati, A., E. Faccioli, E. B. Carulli, F. Culchi, R. Onofri, S. Stefanini, and F. Ulcigrai, (1980). Studio di microzonizzazione sismica dell'area di Tarcento (Friuli). *Edito da Regione Autonoma Friuli-Venezia-Giulia*.
- Brune , J. N. (1970). Tectonic stress and the spectra of seismic shear waves from earthquakes. *J. Geophys. Res.*, **75**, 4997-5009.

- Campillo, M., J. C. Gariel, K. Aki, and F. J. Sanchez-Sesma (1989). Destructive strong ground motion in Mexico City: source, path and site effects during great 1985 Michoacan earthquake. *Bull. Seism. Soc. Am.*, **79**, 1718-1735.
- Celebi, M. (1987). Topographical and geological amplifications determined from strong-motion and aftershock records of the 3 March 1985 Chile earthquake. *Bull. Seism. Soc. Am.*, **77**, 1147-1157.
- Cinti, F. R., L. Faenza, W. Marzocchi, and P. Montone (2004). Probability map of the next $M \geq 5.5$ earthquakes in Italy. *Geochemistry, Geophysics, Geosystem*, **5**, Q 11003, doi: 10.1029/2004GC000724.
- Doglioni, C., P. Harabaglia, G. Martinelli, F. Mongelli, G. Zito, (1996). A geodynamic model of the Southern Apennines accretionary prism. *Terra Nova*, **8**, 540-547.
- Eurocode 8: Design of structures for earthquake resistance. Part 1: General rules, seismic actions and rules for buildings. Draft January 2003.
- Field, E. H., and K. H. Jacob (1995). A comparison and test of various site-response estimation techniques, including three that are not reference-site dependent. *Bull. Seism. Soc. Am.*, **4**, 1127-1143.
- Fumal, T. E. and J. C. Tinsley (1985). Mapping shear wave velocities of near surface geologic materials. *Evaluating Earthquake Hazard in the Los Angeles Region--An Earth-Science Perspective*, J. E. Ziony (editor), *U.S. Geol. Surv. Profess. Pap.* **1360**, 101-126.
- Gutenberg, B. (1927). *Grundlagen der Erdlebenskunde*, Berlin.
- Hanks, T. C., and H. Kanamori (1979). A Moment Magnitude Scale. *J. Geophys. Res.*, **84**, 2348-2350.
- Hanks, T. C., and R. K. McGuire (1981). The character of High-frequency Strong Ground Motion. *Bull. Seism. Soc. Am.*, **71**, 2071-2095.

- Hanks, T. C. (1982). Fmax. *Bull. Seism. Soc. Am.*, **72**, 1867–1879.
- Harmsen, S. C. (1997b). Determination of site amplification in the Los Angeles urban area from inversion of strong-motion records. *Bull. Seism. Soc. Am.*, **87**, 866-887.
- Hartzell, S., A. Leeds, A. Frankel, and J. Michael (1996a). Site response for urban Los Angeles using aftershocks of the Northridge earthquake. *Bull. Seism. Soc. Am.*, **86**, S168-S192.
- Hartzell, S., S. Harmsen, A. Frankel, D. Carver, E. Cranswick, M. Meremonte and J. Michael (1996b). Site response maps for the Los Angeles region based on earthquake ground motions. *U.S. Geol. Surv. Open-file Rept.* 96-723, 14 pp.
- Iwata, T., and K. Irikura (1988). Source parameters of the 1983 Japan earthquake sequence. *J. Phys. Earth*, **36**, 155-184.
- Joyner, W. B. and D. M. Boore (1981). Peak horizontal accelerations and velocity from strong-motion records including records from the 1979 Imperial Valley, California, earthquake. *Bull. Seism. Soc. Am.*, **71**, 2011-2038.
- Joyner, W. B. and T. E. Fumal (1985). Predictive mapping of earthquake ground motion, in *Evaluating Earthquake Hazard in the Los Angeles Region-An Earth-Science Perspective*, J.E. Ziony (Editor), *U.S. Geol. Surv. Profess. Pap.* **1360**, 203-220.
- Kawase, H., and K. Aki (1990). Topography effect at the critical SV wave incidence: possible explanation of damage pattern by Whittier-Narrows, California, earthquake of 1 October 1987. *Bull. Seism. Soc. Am.*, **80**, 1-22.
- Langston, C. A. (1979). Structure under Mount Rainier, Washington, inferred from teleseismic body waves. *J. Geophys. Res.*, **84**, 4749-4762.
- Lermo, J., and F. J. Chavez-Garcia (1993). Site effect evaluation using spectral ratios with only one station. *Bull. Seism. Soc. Am.*, **83**, 1574-1594.

- Lermo, J., and F. J. Chavez-Garcia (1994). Are microtremors useful in site response evaluations? *Bull. Seism. Soc. Am.*, **84**, 1350-1364.
- Malagnini L., R. B. Herrmann, and M. Di Bona (2000). Ground-Motion Scaling in the Apennines. (Italy). *Bull. Seism. Soc. Am.*, **90**, 1062–1081.
- Mallet, R.(1862). Great Neapolitan Earthquake of 1857. London, **2** vols.
- McGuire, R. K., and T. C. Hanks (1980). RMS Accelerations and Spectral Amplitudes of Strong Ground Motion during the San Fernando, California, Earthquake. *Bull. Seism. Soc. Am.*, **70**, 1907-1919.
- Menke, W. (1989). Geophysical data analysis: discrete inverse theory. *International geophysics series*, Vol. **45**.
- Moya A., J. Aguirre, and K. Irikura (2000). Inversion of source parameters and site effects from strong ground motion records using genetic algorithms. *Bull. Seism. Soc. Am.*, **90**, 977-992.
- Montone, P., M. T. Mariucci, S. Pondrelli, and A. Amato, (2004). An improved stress map for Italy surrounding regions (central Mediterranean). *J. Geophys. Res.*, **109**, B10410, doi: 10.1029/2003JB002703.
- Nakamura, Y. (1989). A method for dynamic characteristics estimations of subsurface using microtremors on the ground surface. *Q. Rep. Railway Tech. Res. Inst. Japan*, **30**, 25-33.
- Nogoshi, M., and T. Igarashi (1970). On the propagation characteristics of microtremors. *J. Seism. Soc. Japan*, **23**, 264-280.
- Nunziata, C., M. Natale, and G. F. Panza (2004). Seismic characterization of Neapolitan soils. *Pure and Appl. Geophys.*, **161**, 1285-1300.
- Nunziata, C., M. Natale, G. Luongo, G. F. Panza (2006). Magna reservoir at Mt. Vesuvius: Size of the hot, partially molten, crust material detected deeper than 8 km. *Earth and Planetary Science Letters*, **242**, 51-57.

- Pantosti, D., and G. Valensise (1990). Faulting mechanism and complexity of the 23 November 1980, Campania-Lucania earthquake inferred from surface observations. *J. Geophys. Res.*, **134**, 15,319-15,341.
- Papageorgiou, A. S., and K. Aki (1983b). A specific barrier model for the quantitative description of inhomogeneous faulting and the prediction of strong ground motion. Part II. Applications of the model. *Bull. Seism. Soc. Am.*, **73**, 953–978.
- Park, S. and S. Elrick, (1998). Prediction of shear wave velocities in Southern California using surface geology. *Bull. Seism. Soc. Am.*, **88**, 677-685.
- Parolai S., and Sandra M. Richwalski (2004). The Importance of Converted Waves in Comparing H/V and RSM Site Response Estimates. *Bull. Seism. Soc. Am.*, **94**, 304-313.
- Patacca, E., and P. Scandone, (1989). Post-Tortonian mountain building in the Apennines. The role of the passive sinking of a relic lithospheric slab. In: The lithosphere in Italy, Boriani, A., M Bonafede, G.B. Picardo, G.B. Vai, (Eds). *Accad. Naz. Lincei*, **80**, 157-176.
- Patacca, E., R. Sartori, P. Scandone, (1990). Tyrrhenian Basin and Apenninic arc: kinematic relations since Late Tortonian times. *Mem. Soc. Geol.*, **45**, 425-451.
- Pedersen, H., B. LeBrun, D. Hatzfeld, M. Campillo, and P.-Y. Bard (1994). Ground motion amplitude across ridges. *Bull. Seism. Soc. Am.*, **84**, 1786-1800.
- Pescatore, T., P. Renda, M. Schiattarella, M. Tramutoli (1999). Stratigraphic and structural relationships between Meso-Cenozoic Lagonegro Basin and coeval carbonate platform in Southern Apennines, Italy. *Tectonophysics*, **315**, 269–286.
- Press W. H., B. P. Flannery, S. A. Teukolsky, and W. T. Vetterling (1987). Numerical Recipes. The Art of Scientific Computing. *Cambridge University Press*.
- Roure, F., P. Casero, R. Vially (1991). Growth processes and melange formation in the Southern Apennines accretionary wedge. *Earth Planet. Sci. Lett.*, **102**, 395-412.

- Sanchez-Sesma, F. J. (1990). Elementary solutions for the response of a wedge-shaped medium to incident SH and SV waves. *Bull. Seism. Soc. Am.*, **80**, 737-742.
- Singh, S. K., Ordaz, M., Dattatrayam, R. S., And Gupta, H. K. (1999). A Spectral Analysis of the 21 May 1997, Jabalpur, India, Earthquake (Mw= 5.8) and Estimation of Ground Motion from Future Earthquakes in the Indian shield region. *Bull. Seism. Soc. Am.*, **89**, 1620–1630.
- Singh, S. K., W. K. Mohanty, B. K. Bansal, and G. S. Roonwal, (2002). Ground motion in Delhi from future large/great earthquakes in the central seismic gap of the Himalayan arc. *Bull. Seism. Soc. Am.*, **92**, 555–569.
- Siro, L. (1982). Southern Italy November 23, 1980 earthquake. In: *Proceedings of the Seventh European Conference on Earthquake Engineering*, September 20-25, Athens, Greece, Technical Chamber of Greece (Editor), **7**, 419-429.
- Steidl, J., A. G. Tumarkin, and R. J. Archuleta (1996). What is a reference site? *Bull. Seism. Soc. Am.*, **86**, 1733-1748.
- Takahashi, K., S. Ohno, M. Takemura, T. Ohta, Y. Sugawara, T. Hatori, and S. Omote (1992). Observation of earthquake strong motion with deep borehole: generation of vertical motion propagating in surface layers after S-wave arrival. *Proceedings of the 10th World Conference on Earthquake Engineering*, **3**, 1245-1250.
- Tarantola A., (2005). Inverse Problem Theory and Methods for Model Parameter Estimation. *Siam*, editor.
- Tinsley, J. C. and T.E. Fumal (1985). Mapping Quaternary sedimentary deposit for areal variations in shaking response, in Evaluating earthquake hazard in the Los Angeles region-an earth-science perspective. *U.S. Geol. Surv. Profess. Pap.*, **1360**, 101-125.
- Trifunac, M. D., and Hudson, D. E. (1971). Analysis of the Pacoima Dam accelerograms – San Fernando earthquake of 1971. *Bull. Seism. Soc. Am.*, **61**, No. 5, 1393-1411.

- Tsurugi, M., M. Tai, K. Irikura, and A. Kowada (1997). Estimation of empirical site amplification effects using observed records. *Zisin J. Seism. Soc. Japan*, **50**, 215–227 (in Japanese).
- Valensise, G., A. Amato, P. Montone, and D. Pantosti (2003). Earthquakes in Italy: Past, present and future. *Episodes*, **26** (3), 245-249.
- Wald, D. J., V. Quitoriano, T. H. Heaton, H. Kanamori, C. W. Scrivner, and C. B. Worden (1999). TriNet "ShakeMaps": Rapid Generation of Peak Ground Motion and Intensity Maps for Earthquakes in Southern California. *Earthquake Spectra*, Vol. 15, No. **3**, 537-556.
- Weber, E., G. Iannaccone, A. Zollo, A. Bobbio, L. Cantore, M. Corciulo, V. Convertito, M. Di Crosta, L. Elia, A. Emolo, C. Martino, A. Romeo, C. Satriano, (2006). Development and testing of an advanced monitoring infrastructure (ISNet) for seismic early-warning applications in the Campania region of Southern Italy in P. Gasparini et al. editors, *Seismic Early Warning*, Springer-Verlag.
- Weber E., V. Convertito., G. Iannaccone, A. Zollo, A. Bobbio, L. Cantore, M. Corciulo, M. Di Crosta, L. Elia, C. Martino, A. Romeo and C. Satriano (2007). An Advanced Seismic Network in the Southern Apennines (Italy) for Seismicity Investigations and Experimentation with earthquake Early-Warning. *Seism. Res. Letters*, **78**, n°6 (in press).
- Westaway, R., and J. Jackson (1987). The earthquake of 1980 November 23 in Campania-Basilicata (Southern Italy). *Geophys. J. R. Astr. Soc.*, **90**, 375–443.
- Zollo A., G. Iannaccone, A. Emolo, M. Lancieri, and E. Weber (2004). The irpinia fault system as a natural laboratory for earthquake fracture related studies in *The many facets of seismic risk*, edited by M. Pecce, G. Manfredi, and A. Zollo.